DOE Award Number: DE-FC26-05NT42455

Report Type: Final Technical Report

Project Reporting Period: January 1, 2006 -- June 4, 2010

Novel Sorption Enhanced Reaction Process for Simultaneous Production of CO_2 and H_2 from Synthesis Gas Produced by Coal Gasification

Principal Investigator: Prof. Shivaji Sircar (shs3@lehigh.edu)
Principal Investigator: Prof. Hugo S. Caram
(hsc0@lehigh.edu)
Dr. Kwangkook Jeong,
Dr. Michael G. Beaver,
Mr. Fan Ni,
Mr. Agbor Tabi Makebe

Department of Chemical Engineering
Lehigh University
111 Research Drive, Iacocca Hall
Bethlehem, PA 18015
June 2010

Submitted by: Dr. Michael G. Beaver

DISCLAIMER

Abstract

The goal of this project is to evaluate the extensive feasibility of a novel concept called Thermal Swing Sorption Enhanced Reaction (TSSER) process to simultaneously produce H_2 and CO_2 as a single unit operation in a sorber-reactor. The successful demonstration of the potential feasibility of the TSSER concept implies that it is worth pursuing further development of the idea. This can be done by more extensive evaluation of the basic sorptive properties of the CO_2 chemisorbents at realistic high pressures and by continuing the experimental and theoretical study of the TSSER process. This will allow us to substantiate the assumptions made during the preliminary design and evaluation of the process and firm up the initial conclusions.

The task performed under this project consists of (i) retrofitting an existing single column sorption apparatus for measurement of high pressure CO_2 sorption characteristics, (ii) measurement of high pressure CO_2 chemisorption equilibria, kinetics and sorption-desorption column dynamic characteristics under the conditions of thermal swing operation of the TSSER process, (iii) experimental evaluation of the individual steps of the TSSER process (iv) development of extended mathematical model for simulating cyclic continuous operation of TSSER to aid in process scale-up and for guiding future work, (v) simulate and test SER concept using realistic syngas composition, (vi) extensive demonstration of the thermal stability of sorbents using a TGA apparatus, (vii) investigation of the surfaces of the adsorbents and adsorbed CO_2 ,and (viii) test the effects of sulfur compounds found in syngas on the CO_2 sorbents.

Table of Contents

1. Executive Summary

One vision of clean energy for the future is to produce hydrogen from coal by partial oxidation with oxygen and steam in an ultra-clean plant. The conventional route to achieve this is to (1) treat the coal gasification product in a water gas shift (WGS) reactor to convert CO to CO_2 and H_2 by reacting with H_2O and (b) separate the reaction products in a pressure swing adsorption (PSA) system to produce a pure hydrogen product gas at the feed gas pressure. A waste fuel gas containing CO_2, CO and H_2 is also produced by the PSA process. There is a need for developing a compact (small foot print) and more efficient H_2 production method which reduces the capital cost. Simultaneous production of a CO_2 by-product at the feed gas or a higher pressure will also be very attractive for its sequestration or sale.

A novel concept called Thermal Swing Sorption Enhanced Reaction (TSSER) process which was designed to achieve these goals by simultaneously carrying out the WGS reaction and the separation of CO_2 from the reaction zone by selective chemisorptions on a sorbent in a single unit operation. The chemisorbent was periodically regenerated by steam purge using the principles of thermal swing adsorption (TSA) for cyclic operation of the process. The concept permitted circumvention of the thermodynamic limitations of the WGS reaction and enhanced the forward rate of reaction. The research objectives included (i) construction of a single column sorption apparatus for characterizing the equilibrium and dynamic adsorptive properties of potential CO_2 chemisorbents as well as the individual steps of the proposed TSSER process, and (ii) developing a mathematical process design model for scale up, optimization, and guiding future work. Two novel chemisorbents (Na_2O promoted alumina and K_2CO_3 promoted hydrotalcite) were identified as potential CO_2 chemisorbents for this application. They exhibited

(a) high selectivity for CO_2 chemisorption over CO, N_2, and H_2 in presence of steam at a temperature of 200-500 ^oC (alumina) and 400-550 ^oC hydrotalcite), (b) decent CO_2 working capacities by the cyclic TSSER process, (c) moderate heats of chemisorptions, (d) relatively fast kinetics of CO_2 sorption, (e) ease of CO_2 desorption by an inert gas (e.g. steam) purge, and (f) thermal stability. These properties were experimentally and theoretically evaluated in our laboratory during this project. Extensive mathematical model simulations of the performance of the TSSER concept showed that both materials can be used to fulfill the goals of this project: simultaneous production of a fuel cell grade H_2 product gas (dry basis) at reaction pressure and an essentially pure and compressed (much above reaction pressure) CO_2 by-product gas (dry basis) from an ideal synthesis gas ($CO+H_2+H_2O$) by sorption enhanced WGS reaction.

In the second period of project, we have done more extensive evaluation of the basic sorptive properties of the CO_2 chemisorbents at realistic high pressures (up to 20 atm) and continued the experimental and computational study of the TSSER process. The various experiments including sulfur sorption, high pressure retrofitting of the sorption apparatus and high pressure sorption measurement, DRIFTS (Diffuse Reflectance Infrared Fourier Transform Spectroscopy), Raman Spectroscopy, SEM (Scanning Electron Microscopy), TPSR (Temperature Programmed Surface Reaction), and TPD (Temperature Programmed Desorption) were made during the period. The computational research was extended to heat recovery analysis from high temperature desorption streams produced by the process and TSSER heat integration analysis. A modeling for heat and mass transfer processes and phase change in a high pressure, high temperature condenser was carried out to explore the performance of the condenser and the fraction of heat recovery. A finite difference method was used to solve the boundary value problem. Additional insight into the problem was obtained by describing the operating lines and

equilibrium condition in an enthalpy diagram. An experimental study to evaluate the tolerance of these chemisorbents to trace amounts of SO_2 and H_2S was completed by measuring the CO_2 capacity of the materials before and after exposure to the sulfur compounds. The tests were conducted using a small adsorber containing about a gram of the sorbent, passing a stream of 15 % CO_2 in N_2 at near ambient pressure and a temperature of 250 ~ 400 ^oC over the sorbent and monitoring the effluent gas CO_2 concentration with time, and cyclically repeating the experiment after exposing to either SO_2 (~1,000 ppm in N_2) or H_2S (~190 ppm in N_2) until breakthrough. A scheme for heat integration of the TSSER process was developed to help aid in a first pass economic evaluation of the TSSER process. The first pass evaluation looks promising. A series of surface analysis techniques were employed to explore the surfaces of the chemisorbents under CO_2 sorption conditions.

2. Experimental study on high pressure CO_2 sorption

In the first phase of this project CO_2 sorption properties were measured up to CO_2 partial pressures of ~2 atm due to pressure limitations of the sorption apparatus hardware such as mass flow controllers. A retrofit of the column apparatus was needed in order to measure high pressure CO_2 sorption data. New mass flow controllers tolerant of high pressure were ordered and installed. New solenoid valves were ordered and installed to replace the faulty old solenoids valves. A new back pressure regulator was also installed. A new adsorption column was also constructed from Inconel Alloy 600, chosen due to its stability at high temperatures and pressures (the alloy can easily withstand temperatures of >600°C and pressures of >40 atm. The old column has been exposed to extensive thermal cycling over the past 5 years, and a back up column was needed in the event of failure as the old column has seen much usage in this time.

The new column is 43” in length and is fitted with three thermocouples located 10” apart. The column also features a 6” line of tubing that has a pressure gauge fitted on the end that will allow for the measurement of pressure rise inside the column due to thermal desorption of CO_2 from the chemisorbents during the cyclic process step testing. The automated control valves will allow for quick shut-off of gas flow into and out of the reactor. Figure 1 shows a picture of the newly assembled sorption column.

Ensuring a leak proof system is essential for high pressure sorption measurement, and helium was used to leak test the sorption apparatus. In order to identify system gas leaks on the modified sorption apparatus, a Laco Technologies LHHLD-1000 Minitracer Helium leak detector was ordered. The system was filled with Helium under high pressure (~10 atm), and the detector was passed over all fittings and pipelines until all detectable leaks were identified, as indicated by the handheld leak detector. The leaks were sealed, and the system was found to hold pressure.

The experimental study on CO_2 adsorption characteristics at high pressure has been started after final leak testing of all equipment. The sorber reactor was filled with Na_2O promoted alumina as sorbent (~100 g) and was pressurized to 5.1 atm pressure and heated to 250°C in flowing N_2. Once flow readings, temperatures, and pressures were stabilized, the gas feed was changed to 80% CO_2 in N_2 to yield a gas phase CO_2 partial pressure of ~4.1 atm. As with the low pressure experiments, the column was completely saturated with CO_2 at the conditions stated above for ~2-3 hours. The column was desorbed by switching gas flow to pure N_2 in a countercurrent flow path and also by raising column temperature to 450°C. The desorption cycle was continued for ~6-8 hours.

The adsorption and desorption of CO_2 and gas concentrations were measured by Gow Mac and Mass Spectrometer. The CO_2 sorption capacities for three experimental runs was 1.242, 1.246, and 1.160 moles of CO_2 / kg of adsorbent at a CO_2 partial pressure of 4.1 atm. An updated plot of the CO_2 sorption isotherm at 250°C appears (experimental and model) in Figure 2. The analysis of test results have been carried out and the new high pressure data point (4.1 atm) was found to have a good close of the mass balance, and it is observable that the higher pressure sorption data collected at this temperature deviates from that predicted by the sorption model.

The sorption data at 250°C was refitted to the sorption model by changing the sorption parameters until an adequate fit was achieved for the 250°C data. Once a good fit was obtained, the new parameters were used to fit the isotherm data at 150, 250, 350, and 450°C where sorption data was previously measured. Care was taken to adjust the model parameters so that the model described the sorption data at all four temperatures of interest. Table 1 gives the values of the new sorption parameters at these four temperatures, and Figure 3 shows a plot of the experimental data with the isotherm fits using the parameters of Table 1. We have currently used the mixture gas made by balancing between two cylinders of CO_2 and N_2 gases at high pressure, which needs sensitive and sophisticated adjustment to mix at high pressure. Flow problems have been encountered, so a cylinder of pre-mixed 80% CO_2 in N_2 was ordered to facilitate high pressure CO_2 sorption measurements.

3. Extended mathematical model for simulating cyclic continuous operation of TSSER

A high pressure condenser is considered to be used to remove water vapor as well as recover heat from the desorbed steam – CO_2 gas mixture in a novel sorption enhanced reaction process. This piece of equipment is essential to the heat recovery of the process as steam is needed to regenerate the adsorbent; this high pressure condensing heat exchanger allows for the recovery of heat from the desorbing gas stream and also for the production of essentially pure CO_2 from the desorbing gas stream. Successful recovery of heat will reduce the operating energy costs of the TSSER process as less energy will be needed to generate steam if the heat can be recovered. It is possible to have water condensation at the gas side as well as water evaporation at the coolant water side due to large temperature difference between the hot and cold side. In this study, a model of heat and mass transfer processes and phase change in the system was developed to understand the complex phenomena associated with the simultaneous condensation and evaporation taking place in the unit. A finite difference method was used to solve the boundary value problem describing the problem. Additional insight into the problem was obtained by describing the operating lines and equilibrium condition in enthalpy diagram. The model was used to explore the performance of the condenser and the fraction of the heat recovery as the desorption progressed. The heat recovery was best at the beginning of the process when the superheated steam was generated.

3.1 Background

Conventional production of hydrogen from coal gasification is a commercial technology. As shown in Figure 4, it involves high pressure partial oxidation of coal with oxygen and steam

to produce a synthesis gas containing H_2, CO, CO_2, H_2O and traceable amounts of H_2S and COS. The synthesis gas is cooled down and the impurities are removed. Then the gas is subjected to catalytic water gas shift (WGS) reaction ($CO + H_2O \leftrightarrow CO_2 + H_2$) for converting most of the CO to H_2 and CO_2. The effluent gas from WGS reactor is sent to a gas purification system for production of pure H_2 through a condensation separation process and a pressure swing adsorption process.[1]

In this study, a novel TSSER (Thermal Swing Sorption Enhanced Reaction) process has been developed to combine the water gas shift reaction and the subsequent CO_2 separation from the reaction product in a single unit operation for simultaneous production of essentially pure CO_2 and H_2 products, both at feed gas pressures (Figure 5). A H_2 enriched product (~ 99.99+ %) is produced at feed pressure by condensing out the water from the reactor effluent by cooling. Then the sorber-reactor is counter-currently purged with superheated steam at pressure P_H (design variable, up to ~40 bar) and temperature T_H (design variable, up to 550 °) until most of the CO_2 is desorbed out of the column.

A high pressure condenser is used to condense the steam from the desorbed gas mixture and produce a nearly pure carbon dioxide stream at elevated pressure. In this work, a heat exchanger model is used to determine the best heat recovery through case studies of the process.[2]

It is necessary for condensation modeling to consider the effect of non-condensable CO_2 gas exhausted with the purge steam from the TSSER condensation process. The condenser is operated at high pressure up to 40 bar on both sides with large temperature differences (up to 170 ^oC in terms of Log Mean Temperature Difference (LMTD)) between the hot and cold side. Accordingly, it is important to predict properties at high pressure and post dryout heat transfer in boiling modeling.

Previous work on condensation heat transfer

The goals of modeling the high pressure condenser are 1) to condense steam out of the effluent gas (CO_2 + steam) from the desorption step of the TSSER process and produce a high purity (95+%), high pressure (40 bar) stream of CO_2, and 2) to recover as much heat as possible to minimize energy needs of the TSSER process. The 95+% CO_2 stream meets CO_2 pipeline specifications and the high pressure (40 bar) will greatly reduce the necessary compression required to be of CO_2 pipeline specifications (140 bar). Heat recovery is essential to the TSSER process as steam is used as the purge gas and this recovered heat can be used to minimize the energy needed by the process. The high pressure condenser will have two-phase flow in both the shell and tube sides, and the ability to recover heat from the CO_2 + H_2O stream by the model depends on the ability to accurately predict where the phase changes occur in the unit.

In 1980, Webb et al.[3] developed a one dimensional numerical model to predict condensation with the effect of non-condensable gases in a 10-row by 10-column finned tube heat exchanger by solving the Colburn-Hougen equation for refrigerant R-11 and air mixture. An iterative solution procedure was applied to solve the equation.

From 1999 to 2003, Osakabe et al.[4-7] carried out one-dimensional heat and mass balance calculations for the condensation of flue gas in bare and finned tube heat exchangers. Experimental studies using actual flue gas from propane, natural gas and oil combustion were conducted to investigate the effect of parameters and then compared with the computational results.

In 2005, Oh et al.[8-10] performed steam condensation experiments inside vertical tube submerged in pool water for complete condensation, cyclic venting and through-flow modes. With pressure ranging from 0.1 to 0.4 MPa, their results showed that as the system pressure

increased, the condensation heat transfer rate was enhanced but the condensation heat transfer coefficient decreased.

In 2008, Lee et al.[11] developed a theoretical model using a heat and mass transfer analogy and a simple model using Lee and Kim's correlation were developed to investigate the effects of noncondensable gas on steam condensation heat transfer inside a vertical tube submerged in a pool of water and applied the model to the design of a PRHRS (Passive Residual Heat Removal System) condensation heat exchanger in a SMART-P (System-integrated Modular Advanced ReacTor Power) plant. They investigated the effects of the system pressure on the PRHRS condensation heat exchanger. The phase-change region to complete condensation of steam at the given system became shorter as the system pressure increased from 1.3 to 8.6 MPa due to enhanced heat transfer.

In 2010, Jeong et al.[12, 13] derived energy balance equations governing heat and mass transfer in a condensing heat exchanger designed for separating water vapor and sulfuric acid from flue gas of power plant. A computer program was developed to solve the split boundary problem with the equations by using a one dimensional finite difference method. The modeling results were verified with test results made at a power plant and showed good agreement.

Previous work on boiling heat transfer at high pressure

In 1962, Schrock et al.[14] developed an empirical correlation to predict local heat transfer coefficients for forced flow boiling of water in vertical tubes at pressures ranging from 2.9 to 34.8 bar, which was recommended for the range of quality from 0 to 50 %.

In 2000, Mori et al. classified their dryout results into three characteristic regimes based on the experimental trends they observed and presented prediction methods for their values of dryout inception x_{di} and completion x_{de}.

In 2005, experimental data taken by Wojtan et al.[15,16] agreed with dryout regime of Mori et al.[17] The approach of Mori et al. has been extended by including the heat flux effect using the non-dimensional ratio and new empirical factors based on all experimental points and using the least squares method.

3.2 Analytical Modeling

In this study, the governing equations based on mass and energy balances for water boiling and condensation were derived to predict variables; gas exit temperature, water condensation rate, and mole fraction at gas side and cooling water exit temperature, steam generation rate and quality at coolant side.

Further insight into the model is obtained using a graphical method that illustrates the operating conditions and bounds in the process. As a result of study, several cases were analyzed for evaluation of the system. A counter-flow shell and tube heat exchanger with an inside diameter of 0.6 m, length of 6 m, and 2 vanes per meter of shell length and 281 to 895 12.7 mm OD tubes of 3 mm thickness was used in the study. The tube pitch was 1.5 (s_L/d_o, longitudinal) X 1.5 (s_T/d_o, transverse), and total heat transfer area varied between 102 to 272 m^2.

3.2.1 Mass and energy balances

If there is no condensation in the gas side or evaporation in the coolant side, the energy equations for both streams are familiar:

$$\dot{m}_g \cdot c_{p.g} \cdot \frac{dT_g}{dA} = h_g \cdot (T_g - T_w) \quad (1)$$

$$\dot{m}_c \cdot c_{p.c} \cdot \frac{dT_c}{dA} = h_c \cdot (T_w - T_c) \quad (2)$$

where T_w (K), the tube wall temperature, is set by the selection between h_g and h_c (W/m^2 K^{-1}), the respective heat transfer coefficients, and $\dot{m}_g$ and $\dot{m}_c$ (kg/s), the respective gas and mass flow rates, remain constant. T_g and T_c are the respective gas and coolant temperatures, $c_{p,g}$ and $c_{p,c}$ are the respective gas and coolant specific heats (kJ/kg K^{-1}), and A is the differential heat exchange area (m^2).

If there is condensation in the gas side, the wall temperature is now given by the well known Colburn-Hougen relation and the steam saturation temperature at its partial pressure at the wall:

$$h_g(T_g - T_i) + k_m \cdot l_{LC} \cdot (y_{H_2O} - y_i) = h_c(T_i - T_c) \quad (3)$$

The interfacial temperature, T_i, is found by relating the mole fraction at the wall, y_i, to the vapor-liquid equilibrium temperature. y_{H2O} is the gas phase water mole fraction, k_m is the mass transfer rate of the condensation (kg/m^2 s^{-1}), and l_{LC} is the latent heat of condensation of water (kJ/kg). Due to condensation, mass flow in the gas side is no longer constant and it varies according to the relation:

$$\frac{d\dot{m}_g}{dA} = k_m \cdot (y_{H_2O} - y_i) \quad (4)$$

If there is evaporation in the coolant side, the temperature will remain constant at the boiling point of the coolant and the mass of vapor will vary as

$$\frac{d\dot{m}_{bo}}{dA} = \frac{h_g(T_g - T_w)}{l_{LV}} \quad (5)$$

where m_{bo} is the mass flow rate of boiling water (kg/s) and l_{LV} is the latent heat of vaporization of H_2O (kJ/kg).

Heat and Mass Transfer Coefficients

The Colburn j factors for heat and mass transfer with their applicable ranges are defined as:[19,20]

$$j_H = St \cdot \mathrm{Pr}^{2/3} = \frac{h}{\rho \cdot c_p \cdot V} \cdot \mathrm{Pr}^{2/3} \qquad (6)$$
$$0.6 < \mathrm{Pr} < 60$$

$$j_m = St_m \cdot Sc^{2/3} = \frac{k_D}{V}(Sc)^{2/3} \qquad (7)$$
$$0.6 < Sc < 3000$$

where h is convective heat transfer coefficient [W/m^2 K^{-1}], ρ is the fluid density (kg/m^3), c_p is the fluid specific heat (kJ/kg K^{-1}), V is the fluid velocity (m/s), and k_D is convective mass transfer coefficient [m/s]. In Equation (6), the term Pr is the fluid Prandtl number and is calculated by $Pr = (c_p * \mu)/k$ and gives the rate of viscous diffusion to thermal diffusion. μ is the fluid dynamic viscosity (kg/m s^{-1}) and k is the fluid thermal conductivity (W/m K^{-1}). In Equation (7), the term Sc is the mass transfer-equivalent of Pr and is calculated from $Sc = \mu/(\rho * D)$. D is the effective mass diffusivity of the fluid (m^2/s). The Chilton-Colburn analogy requires equating Equation (6) and (7), that is, $j_H = j_m$. Then an expression for the mass transfer coefficient, k_m, is derived as :

$$k_m = \frac{h_g \cdot M_{H_2O}}{c_{p,g} \cdot M_g \cdot y_{lm} \cdot Le_{H_2O-gas}^{2/3}} \qquad (8)$$

where M_{H2O} is the molecular weight of H_2O (kg/mol), M_g is the molecular weight of the gas mixture(kg/mol), and $Le_{H2O\text{-}gas}$ is the dimensionless Lewis number of the gas mixture. All properties are calculated based on composition of mixture, and y_{lm}, the logarithmic mole fraction of the non-condensable gas across the film is:[21,22]

$$y_{lm} = \frac{y_{ni} - y_{nb}}{\ln(y_{ni} / y_{nb})} \tag{9}$$

where y_{ni} and y_{nb} are the mole fractions of non-condensable gases at the gas/film interface and in the bulk flow, respectively.

The variable Le_{H_2O-gas} at Equation (8) is the Lewis number of water vapor in desorption gas, in which D_{H_2O-gas} is the mass diffusion coefficient of water vapor in the desorption gas.[22]

$$Le_{H_2O-gas} = \frac{Sc}{\mathrm{Pr}} = \frac{\alpha_g}{D_{H_2O-gas}} \tag{10}$$

and α_g is the gas thermal diffusivity (m^2/s)

<u>Convective Heat Transfer Coefficient for Gas Side</u>

To predict the convective heat transfer coefficient on the gas side of a bare tube bank, an empirical correlation proposed by Zukauskas,[23] Equation (11), is used.

$$\overline{Nu_D} = 0.021 \cdot \mathrm{Re}_{D,\max}^{0.84} \cdot \mathrm{Pr}^{0.36} \cdot \left(\frac{\mathrm{Pr}}{\mathrm{Pr}_s} \right)^{1/4} \tag{11}$$

Here $\overline{Nu_D}$ is the average dimensionless Nusselt number given by $\overline{Nu_D} = \frac{hL}{k}$ where h is the convective heat transfer coefficient ($W/m^2\ K^{-1}$), L is a characteristic length (m), and k is the thermal conductivity of the fluid ($W/m\ K^{-1}$). $Re_{D,max}$ is the dimensionless Reynolds number

given by $\mathrm{Re}_{D,\max} = \frac{\rho V L}{\mu}$ where ρ is the fluid density (kg/m^3), V is the fluid velocity (m/s), and μ is the fluid dynamic viscosity (kg/m s^{-1}).

Convective Heat Transfer Coefficient inside Coolant Tubes

The single phase flow heat transfer coefficient of the cooling water side inside the tube is predicted by using the Gnielinski's correlation,[24] Equation (12) is valid for either pure liquid or pure vapor.

$$Nu_D = \frac{(f/8)(\mathrm{Re}_D - 1000)\,\mathrm{Pr}}{1 + 12.7(f/8)^{1/2}(\mathrm{Pr}^{2/3} - 1)} \tag{12}$$

f is a friction factor found from tabulated data.

Boiling Heat Transfer Coefficient inside Coolant Tubes

As tube wall temperature exceeds the saturation temperature of the liquid, boiling starts at the wall. With the start of flow boiling, the coolant water side changes to two phase flow of vapors and liquid phases. Equation (12) is not applicable anymore for two phase flow and a boiling heat transfer coefficient (h_{bo}) should be used to predict the boiling heat transfer inside the tube. The boiling heat transfer coefficient is calculated by using Schrock-Grossman correlation,[14,25] Equation (13), which can be applicable for the high pressure range.

$$h_{bo} = 0.739 \cdot [B_o \times 10^4 + 1.5(1/\chi_{tt})^{2/3}] \cdot h_l \tag{13}$$

where h_l is single phase pure liquid heat transfer coefficient evaluated from Equation (12). Variables of B_o and χ_{tt} are boiling number used by Mumm and the Lochart-Martinelli parameter, respectively, defined as

$$B_o = \frac{Q_c''}{G \cdot l_c} \tag{14}$$

$$1/\chi_{tt} = \{x/(1-x)\}^{0.9}(\rho_l/\rho_v)^{0.5}(\mu_v/\mu_l)^{0.1} \quad (15)$$

where G and x are mass flow per unit area (kg/m^2 s^{-1}) and steam quality, respectively. $Q_C^{"}$ is the heat transfer rate per unit area (W/m^2), and l_C is the latent heat of the coolant (J/kg). ρ and μ are density (kg/m^3) and viscosity (kg/m s^{-1}), respectively. Subscripts of l and v denote liquid and vapor phase, respectively.

Post Dryout Heat Transfer

The operational conditions for the system at high pressure (40 bar) and large temperature difference (LMTD ≈ 170 ^{o}C). Large temperature difference between hot and cold side entails a large temperature gap (wall superheat ≈ 70 ^{o}C) between tube wall and water to be boiled, which can cause a serious instability of two phase flow and unpredictable transition to dry out. The prediction for dryout point and post-dryout heat transfer is critical for the modeling of boiling because the dryout point can occur earlier due to the large temperature difference. The inception and completion of dryout can be calculated from the following equations:[15,16]

$$x_{di} = 0.58\, e^{[0.52-0.235\cdot We_v^{0.17} Fr_v^{0.37}\left(\frac{\rho_v}{\rho_L}\right)^{0.25}]} \quad (16)$$

$$x_{do} = 0.61\, e^{[0.57-5.8\cdot 10^{-3}\cdot We_v^{0.38} Fr_v^{0.15}\left(\frac{\rho_v}{\rho_L}\right)^{-0.09}]} \quad (17)$$

We_v is the Weber number and is calculated by $We_v = \frac{\rho V^2 L}{o}$ where ρ is the fluid density (kg/m^3), V is the velocity (m/s), L is a characteristic length (m), and σ is the interfacial surface tension at the liquid vapor interface (dyne/cm).

Assumptions and Simplifications

The following assumptions were made to complete the development of modeling in this study. It is assumed that boiling heat transfer coefficient is linear from the inception to the completion point of dryout. Only film condensation is assumed on the tube wall surface. Thermal resistance between liquid film and tube wall is neglected. There is no heat loss from system to environment. The chemical composition is assumed with H_2O(g), H_2O(l) and CO_2(g) in desorption gas and H_2O(g) and H_2O(l) in coolant side.

3.2.2 Numerical scheme

The governing equations corresponding to a split boundary value problem are solved using an iterative numerical scheme and a one dimensional finite difference method (FDM) with forward differencing. The known variables were: inlet gas temperature, flow rate and mole fraction of steam, inlet cooling water temperature, and flow rate. The main variables to be solved by modeling were: exit gas temperature and steam mole fraction, and temperature of coolant and condensation rate of steam at gas side etc. All properties at high pressure were predicted by using the database from NIST (National Institute of Standards and Technology).[26]

It operates with the desorption gas (CO_2 + Steam) in the shell side and the cooling water in the tubes. Figure 6 (a) illustrates a simplified schematic of the control volume in the heat exchanger. Flow appears cross flow to the tubes, but the overall flow pattern in the equipment is counter flow. Heat and mass transfer for water condensation in the shell side and phase change for flow boiling in the tube side are considered within this control volume.

Figure 6 (b) shows main variables to be considered for the modeling. The desorption gas temperatures at the inlet and outlet of the shell side are expressed as $T_{g,in}$ and $T_{g,out}$, respectively. The saturation temperatures corresponding to steam partial pressures at the inlet ($y_{H_2O,in}$) and

outlet ($y_{H_2O,out}$) of gas side are $T_{sat,g,in}$ and $T_{sat,g,out}$, respectively. The variables $T_{c,in}$ and $T_{c,out}$ express cooling water temperatures at the inlet and outlet of the tube side, respectively. Saturation temperature corresponding to the operating pressure at tube side is $T_{sat,c}$ at the cooling water side. Tube wall temperature is expressed by T_w. The variable T_i is the interfacial temperature at shell side which is the saturation temperature corresponding to the interfacial mole fraction of steam at the liquid-vapor interface film. The heat transfer coefficients for gas and cooling water side are expressed as h_g and h_c, respectively. The mass transfer coefficient for the case of condensation is k_m.

In order to apply the FDM method, total surface area of the entire system was discretized into a large number of cells. Governing equations are solved at each cell to solve unknown variables from the inlet of gas side to the exit of gas side. The inlet and exit of gas side match to the exit and inlet of coolant water side since the system is assumed as the counter-cross flow heat exchanger. We will study the 'Performance Problem' for different flows of steam, CO_2 and coolant. The exchanger area and configuration will now be fixed.

As shown in Figure 7, there are three possibilities for the coolant condition at the exit: liquid, saturated liquid and vapor, and superheated vapor. The actual condition is obtained by iteration by assuming an exit condition for the coolant, integrating backwards to match the feed condition of the coolant at the entrance of the condenser. Three loops are used to iterate on those possible exit conditions.

The first loop (ITN-1) assumes liquid water (one phase) at the coolant exit and iterates on the exit coolant temperature until the calculated inlet cooling water temperature approaches to the correct target value. The ITN-1 can compute the condensation rate on the gas side without evaporation on the tube side. The program converges only if the calculated inlet cooling water

temperature reaches to the target temperature with convergence of the condensation rate and the exit cooling water tube wall temperature is lower than the saturation temperature. During the loop, tube wall temperature stays below the saturation temperature at both sides everywhere in the heat exchanger. With the first iteration loop, the assumed variable is only the cooling water exit temperature.

If the coolant leaves the condenser as a liquid-vapor mixture, the iteration (ITN-2) is carried out on the mass fraction of steam at the coolant exit. The program calculates phase changes for the cases that the tube wall temperature is either 1) higher or 2) lower than saturation temperature. So it allows both condensation at the gas side and boiling at the coolant side. For example, it tends to have boiling near the exit of coolant side and condensation near the exit of gas side. The program converges if the calculated cooling water inlet temperature reaches to the target temperature with the assumed steam quality for the range of $0 < x \leq 1.0$. The assumed variable is only the steam quality at the coolant exit since the exit coolant temperature is assumed as the saturation temperature.

If the coolant leaves as superheated steam, the third loop (ITN-3) begins with an assumption of exit superheated steam temperature. The ITN-3 computes the phase change from the saturated liquid phase to the superheated steam on the coolant tube side with a possibility of condensation on the gas side. The program can be completed if the calculated cooling water inlet temperature reaches to the target temperature with the assumed exit superheated steam temperature. With the ITN-3, the assumed variable is only the exit temperature of superheated steam on the coolant side.

3.2.3 Process conditions

The composition of the stripping gas changes during the desorption process as the mass flow of CO_2 decreases as it is removed from the bed. As the desorption progresses, the concentration of CO_2 at the gas inlet of heat exchanger varies from 1.0 to zero. As shown in Table 2, the CO_2 concentration varies from 99.0 to 1.35 % while the molar flow rate of CO_2 decreases from 3.57 to 0.05 kmol/s during the desorption cycle. The coolant side is assumed to be a sub-cooled liquid phase at the inlet with a variable flow rate ranging from 1.34 to 7.57 kmol/s, during the process. Figure 8 shows the variations of CO_2 mole fractions and total flow rates in the gas side during the desorption process.

3.2.4 Graphical method using bounded constraint diagram

Since there are multiple phases possible, further insight into the process can be obtained by using a graphical method to study the operational limits of the condenser unit described above. The simplified control volume defined in Figure 9 which consists of the upper hot desorption gas side and lower coolant water side is used to carry out an enthalpy balance. Mixture gas of $\dot{m}_g$ (CO_2 and H_2O) enters into the gas side and exits with condensed liquid water and CO_2, while cooling water at flow rate $\dot{m}_c$ at liquid phase into the coolant side and may exit as either liquid or vapor or a mixture of both. Variables of enthalpies for gas and coolant side passing the dashed volume are expressed by H_g and H_c, respectively.

The enthalpies entering and exiting the volume are shown at the left and right side of Equation (18), respectively. The enthalpy balance yields a linear operating line connecting the enthalpies of the gas phase and the coolant, when the enthalpy of the gas phase is given per unit of mass (mole) of non-condensable CO_2.

$$\dot{m}_g \cdot H_g + \dot{m}_c \cdot H_{ci} = \dot{m}_g \cdot H_{go} + \dot{m}_c \cdot H_c \quad (18)$$

$$H_g = \frac{\dot{m}_c}{\dot{m}_g} \cdot (H_c - H_{ci}) + H_{go} \quad (19)$$

As shown in Figure 10, the operating line for the condenser in the (H_g, H_c) plane is constrained in the region bounded by the following lines: 1) a vertical line corresponding to the enthalpy of the inlet cooling water, 2) a horizontal line corresponding to the enthalpy of the inlet gas, and 3) an equilibrium line corresponding to equal temperature of the gas and cooling water side. The enthalpy lines taken from the inlet cooling water and inlet gas temperature can be drawn by the given boundary conditions at each inlet. The isotherm enthalpy line is drawn by the assumption that the cooling water temperature is the same as the gas at any arbitrary points. With those three enthalpy lines, a bounded constraint diagram can be established in the (H_g, H_c) plane mapped from the temperature domain. Then the straight line made by the result of modeling, which is called 'operating line', is verified by checking if the line is placed inside the bounded graph without crossing or passing the bounded lines.

The actual position of the line depends on the heat transfer area available (A) and it shifts from a single point for A = 0 to a line tangential to the equilibrium point. The slope of the operating line depends on the flow rate ratio of the coolant to gas, $\frac{\dot{m}_c}{\dot{m}_g}$, as shown in Equation (19). Figure 10 contains distinct sections named *L* (liquid), *L+V* (liquid & vapor), and *V* (vapor) to clearly explain the phase matching to each section of the line.

Figure 11 shows all four cases given in Table 2. As shown in Figure 11 (a), the enthalpies of coolant and vapor phase (H_c and H_g) are contained, again, in an area bound by three lines: a horizontal line for the inlet gas enthalpy, a vertical line of the inlet cooling water enthalpy and an "equilibrium" line corresponding to equal gas and coolant temperature. With Figure 11 (a) for Case I, which is saturated water being fed into the system, it is seen that the far right end of the

operating line is located above the vapor phase of cooling water side of the isotherm enthalpy line, which agrees with the modeling result that has mostly superheated vapor at the exit of cooling water side. Moving from Figure 11 (a) of Case I to Figure 11 (d) of Case IV, the slope ($\frac{\dot{m}_c}{\dot{m}_g}$) of the operating line increases as the mass flows of gas decrease and coolant side increase. Figure 11 (d) shows that the operating line has a very steep slope due to very large ratio of $\frac{\dot{m}_c}{\dot{m}_g}$ at the end of process. It means that all vapor involved at gas side is removed by condensation due to much higher heat transfer to coolant side with higher flow rate ratio of cooling water to gas side. Notice that the operating lines do not intersect the equilibrium lines.

3.3 Results and discussion

The simulation of a high pressure condenser has been carried out for a pilot scale shell and tube heat exchanger but can be extended to any scale. The cross-counter flow heat exchanger has desorption gas flowing into the shell side and coolant water flowing into the tube side. The heat exchanger operated at high pressure of 40 bar has been targeted 1) to remove steam from the desorption gas in the shell side and 2) to produce steam in the tube side to recover heat from the hot gas side.

Figure 12 shows the profiles of gas temperature, tube wall temperature and cooling water temperature as results of all cases shown at Table 2. As shown in Figure 12 (a), it is seen that the cooling water leaves the condenser as mostly superheated steam. It is seen that the tube wall temperature abruptly increases at halfway of the heat transfer area due to onset of post-dryout heat transfer. At the post-dryout region, the liquid film may dry out or become entrained in the high velocity vapor-phase, which results in poor heat transfer. In the other extreme case, Figure 12 (d) shows that water condensation occurs over most of the heat transfer surface area as the gas

side gets cooled enough because of relatively high ratio of $\frac{\dot{m}_c}{\dot{m}_g}$. Each result of modeling in Figure 12 (a) to (d) matches well with the results of bounded constraint diagram in Figure 11 (a) to (d).

Figure 13 shows the exit quality of coolant tube side during the time of the desorption cycle. Quality is defined as the mass percentage of water vapor to total coolant flow rate in the tube side. The quality at the coolant exit produces 100% steam in the initial stage of the process since the coolant side of relatively small flow rate gets high enough heat transfer to be converted to superheat. 100% of quality means that all saturated liquid phase coolant water is evaporated into fully saturated vapor phase. However, at the end of the cycle, the quality decreases to zero based on increased coolant flow rate so that it can condense the desorbed gas.

Figure 14 shows condensation efficiency at the gas side. Condensation efficiency is defined as the mass ratio of condensation rate to incoming vapor steam. For example, 100% of condensation efficiency means all incoming vapor at gas side is condensed to liquid phase at the exit. The higher condensation efficiency means the higher removal efficiency of steam from the desorption gas mixture. The condensation efficiency increases from 0 to 98.7% to capture water vapor in the desorption gas by increasing the coolant flow rate and lowering its coolant temperature.

Figure 15 shows the heat recovery rate during the desorption cycle. The heat recovery rate is defined as the ratio of enthalpy change at gas side to enthalpy of incoming gas. It varies from 11.3 to 32.0 % during the cycle and shows a peak at 0.3 min as is also seen at the pattern of desorption gas flow rate in Figure 8. To achieve 100% of steam quality, the coolant water should be decreased but this will reduce the condensation in the gas side. For a 100% steam removal, a high flow rate of coolant relative to gas side is needed but it will be disadvantageous for coolant tube side's steam generation, which is trade-off with the case of steam generation. The heat

recovery profile showed higher rate when the cooling water side experienced vaporization due to boiling.

3.4 Conclusion

The design of a high pressure condenser has been studied for heat recovery from a gas-steam mixture. A possible application is Temperature Swing Sorption Enhanced Reaction (TSSER) process where steam is removed from CO_2 stream generated during the coal gasification process.

Governing equations corresponding to a split boundary value problem are defined for a control volume in a pilot scale shell and tube heat exchanger with appropriate assumptions. A computer program to solve unknown variables in the equations and to predict heat and mass transfer was developed by using MATLAB R2009a. Numerical scheme was made by using an iterative numerical scheme and a one dimensional finite difference method (FDM) with forward differencing.

Process conditions for modeling of case studies were taken with variable flow rates of CO_2 and steam during desorption cycle. A graphical method was also presented by using bounded constraint diagram which was made by three lines: lines of inlet coolant enthalpy, inlet gas enthalpy and equilibrium temperature. The results of modeling were verified with the graphical method of bounded constraint diagram.

Predicted heat recovery rates from the desorption gas side to the cooling water side ranged from 11.3 to 32 %. The heat recovery profile showed higher rate when the cooling water side had phase change to the steam due to boiling. The heat recovered was best at the beginning of the process when superheated steam was generated.

4. First Pass Economic Evaluation and Heat Integration of TSSER Process for production of 30 MMSCFD H_2

The TSSER process uses a thermal swing step to a) facilitate regeneration of the chemisorbent and b) obtain a high-pressure, pure CO_2 stream to facilitate its subsequent compression for sequestration or storage. To calculate the parasitic power consumption of the heating and desorption steps, we have used the following equation, which was developed by NETL[27] for the analysis of thermal swing adsorption systems:

$$\frac{Q}{m_{CO2}} = \frac{m_e}{m_{CO2}} Cp_e \Delta T + \frac{Cp_{solid} \Delta T}{m_{CO2}} + Cp_{gas} T_2 - Cp_{solid} T_1 + \frac{H_r}{m_{CO2}} \quad (20)$$

where m_{CO2} is the mass of CO_2 recovered from the sorber, Q is the heat duty, Cp_e is the heat capacity of the equipment, Cp_{solid} is the heat capacity of the solid, ΔT is the temperature swing employed, Cp_{gas} is the gas phase heat capacity inside the sorber at the end of the SER period, T_2 is the final desorption temperature, T_1 is the temperature of the SER step, and H_r is the heat of CO_2 sorption. The first term $\frac{m_e}{m_{CO2}} Cp_e \Delta T$ accounts for raising the temperature of the sorber-reactor vessel while the second term $\frac{Cp_{solid} \Delta T}{m_{CO2}}$ accounts for the heating the solid inside the vessel. The third term $Cp_{gas} T_2 - Cp_{solid} T$ is the delta enthalpy between gaseous CO_2 at the end of regeneration and the base sorbent at the end of the adsorption step. This third term was found to be relatively small compared to the other terms. The final term of equation (20) accounts for the heat of adsorption to be supplied. This equation has been used to determine the thermal power

needed to perform the thermal swing operation. It should be noted that one advantage of our TSSER process is the ability to produce a compressed CO_2 by product gas stream. This CO_2 will have to be compressed to very high pressures (140 atm) for its subsequent transfer in pipelines to sequestration sites. The amount of compression will decrease as higher desorption temperatures are used, and this will help to nullify some of the additional power needs for the batch heating step.

A preliminary cost analysis of the TSSER process for production of 30MM scfd H_2 appears again in Table 3. The costs show the calculated cost per kg of high purity H_2 produced. Capital cost and power consumption costs were calculated from correlations obtained from a Process design book.[28] The system was designed in the following manner. The H_2 productivity ($H2_{productivity}$) from the simulated TSSER process was used to calculated the mass of sorbent/catalyst mixture needed to meet the target production rate ($H2_{rate}$ = 30 MM scfd) in the desired cycle time (t_{SER} = 5 min). It was decided that at any given time, four vessels would be receiving syngas and producing fuel cell grade H_2. The mass of sorbent/catalyst mixture was calculated by

$$W_{sorbent} = \frac{t_{SER} H2_{rate}}{4 H2_{productivity}} \tag{21}$$

Next the volume of each vessel was calculated by dividing the mass of sorbent/catalyst mixture by the bulk density, ρ_b, of the mixture according to

$$V_{vessel} = \frac{W_{sorbent}}{\rho_b} \tag{22}$$

This system consists of 16 sorber reactor vessels that were chosen to be 16.4 ft in length (=L_c). The vessel cross sectional area (A_{cs}) and diameter (*DIA*) were calculated, assuming that the tubes occupied 80% of the space inside the vessel (void of $\varepsilon = 0.8$), by

$$A_{cs} = \frac{V_{vessel}}{\varepsilon L_c} \tag{23}$$

$$DIA = \sqrt{\frac{4}{\pi} A_{cs}} \tag{24}$$

and the vessel diameter was calculated to be 13.1 ft. 4 vessels undergo the same step of the TSSER process at any given time, and the length of each cycle step is shown in Figure 16. Each vessel contains many 1.73 cm (d_{tube}) diameter tubes packed with the chemisorbent-catalyst admixture. The amount of sorbent per tube (m_{tube}) was calculated by

$$m_{tube} = \rho_b \left(\pi \frac{d_{tube}^2}{4} L_c \right) \tag{25}$$

and the total number of tubes per vessel (N_{tube}) was calculated by

$$N_{tube} = \frac{W_{sorbent}}{m_{tube}} \tag{26}$$

A capital cost for these vessels has been calculated by using an empirical correlation for the capital cost of a fixed head shell and tube style heat exchanger. The calculation is based on the total heat transfer area of the vessel based on the surface area of the tubes (HTA_{tube}). HTA_{tube} is calculated by $HTA_{tube} = \pi d_{tube} L_c$, and the correlation for capital cost of the exchanger is given as

$$C_{pHX} = F_p F_M F_L C_b \tag{27}$$

in US $ where F_p is a factor based on design pressure, F_M is a materials of construction factor (F_M = 1) , and F_L is a tube length factor (F_L = 1.25). *HTA* is the total amount of heat transfer area of the tubes. F_p is given as

$$F_p = 0.9803 + 0.0017\left(\frac{P_d}{100}\right)^2 + 0.018\left(\frac{P_d}{100}\right) \tag{28}$$

where the design pressure, P_d, is calculated from the operating pressure P_o (psig) by

$$P_d = \exp\left(0.60608 + 0.91615\ln(P_o) + 0.0015655\ln^2(P_o)\right) \tag{29}$$

The base cost, C_b, is given as

$$C_b = \exp\left(11.0545 - 0.9288\ln(HTA) + 0.009861\ln^2(HTA)\right) \tag{30}$$

Each vessel requires 8 valves that are assumed to cost $10,000 each, so this is added to C_{pHX} for each vessel, and this number is multiplied by an installation multiplier of 5. The cost of the sorbent/catalyst mixture was assumed to be $7.71 per kg of mixture, and the total cost of sorbent was calculated from the total mass of sorbent needed for the process.

The CO_2 is produced at 40.5 atm by the thermal swing process, and a capital cost for two CO_2 compressors to compress the CO_2 to pipeline pressure (140 atm) is included in Table 3. The compression ratio in the two compressors were 2.0 and 1.73 to raise the pressure to 140 atm and the power consumption of each compressor was calculated from

$$W_{comp} = \frac{mC_pT_{in}}{\eta}\left(R^{\frac{\gamma-1}{\gamma}} - 1\right) \tag{31}$$

where m is the CO_2 flow rate (kg/s), C_p is the gas phase specific heat (C_p = 0.85 kJ/kg K^{-1}), T_{in} is the gas inlet temperature (T_{in} = 310.9 K), R is the compression ratio, γ is the specific heat ratio

(γ_{CO2} =1.287), and η is the compressor efficiency (η = 0.75). The cost of electricity is \$0.10 per kWhr and the cost of electrical energy for CO_2 compression was calculated. The capital cost of the compressors was calculated using an empirical correlation found in the literature and is given by

$$C_{pcomp} = F_d F_M C_B \tag{32}$$

where F_d accounts for how the compressor is driven (electrical driven motor, F_d = 1.15) and F_M depends on the materials of construction (F_M = 2.5 for stainless steel construction). C_{Bcomp} is given by

$$C_{Bcomp} = \exp\left(7.2223 + 0.8\ln(W_{comp})\right) \tag{33}$$

An installation multiplier of 5 was used to finalize the capital cost of the CO_2 compressors. Some assumptions in the cost calculation are plant lifetime of 20 years, the cost of electricity is \$0.10 per kWhr, and the cost of steam is taken from a literature source.[29] It should be noted that this cost analysis takes no credit for the avoidance of CO_2 emission penalties. For example, from the stoichiometry of the WGS reaction, for every 1000 kg of H_2 produced, 22,000 kg of CO_2 is produced. For the simulated 91% conversion of CO to H_2, and the 70.1% recovery of CO_2 at elevated pressure (40.5 atm), this process avoids the emission of 14,214 kg of CO_2 per 1000 kg of H_2 produced. Depending on the price associated with CO_2 emissions, the costs can nearly be offset by the savings of CO_2 capture. For example, if the penalty of CO_2 emissions is \$100/metric ton of CO_2, then this process will save \$1.42/kg of H_2 produced. There is also an estimated capital cost for the cost of chemisorbent/catalyst mixture and heat exchange equipment for the heat integrated process shown in Figure 17.

Table 3 also lists the operating costs of the CO_2 compressors for compressing the CO_2 to 140 atm, the cost of steam for desorption, and the additional heat needed to perform the thermal

swing process. A credit is taken for heat recovery from a constant pressure evaporator/condenser that is being modeled to recover heat from the desorption gas stream, producing the pure, compressed CO_2 by-product. This unit's position in the integrated scheme is shown in Figure 16. This schematic assumes that the feed gas has been scrubbed of sulfur components and other trace impurities. Other opportunities for heat recovery from the effluent H_2 stream (contains a lot of steam) and from the low pressure desorption steps still need to be investigated to fully integrate the process.

5. Experimental study on effect of sulfur compound on CO_2 adsorption

Two CO_2 selective chemisorbents, K_2CO_3 promoted hydrotalcite and Na_2O promoted alumina, have been recently evaluated for direct production of fuel-cell grade H_2 by (a) low temperature steam methane reforming and (b) water gas shift of synthesis gas employing the concept of thermal swing sorption enhanced reaction (TSSER). These sorbents are hydrophobic, and reversibly sorb CO_2 with high selectivity in presence of steam while exhibiting decent CO_2 working capacity under the conditions of a thermal swing sorption process mode. Furthermore, these sorbents can be easily regenerated by steam purge.

This work reports the results of an experimental study to evaluate the tolerance of these chemisorbents for trace SO_2 and H_2S by measuring the CO_2 capacity of the materials before and after exposure to the sulfur compounds. The tests were conducted using a small adsorber containing about a gram of the sorbent, passing a stream of 15 % CO_2 in N_2 at near ambient pressure and a temperature of 250 ~ 400 ^oC over the sorbent and monitoring the effluent gas CO_2 concentration with time, and cyclically repeating the experiment after exposing the sorbent with a trace amount of SO_2 (~1,000 ppm in N_2) and H_2S (~190 ppm in N_2) for a period of time. The

CO_2 capacity was estimated by integration of the effluent gas concentration profiles. Desorption of the sulfur compounds by N_2 purge was also tested periodically.

The results indicate that (a) SO_2 is sorbed on both chemisorbents, and the effective CO_2 capacities are significantly reduced after the exposure to SO_2, (b) the sorbed SO_2 can be desorbed by very prolonged N_2 purge, thereby restoring the CO_2 capacity nearly fully, which indicates reversible but very slow desorption of SO_2, and (c) H_2S is also sorbed on both chemisorbents, and the sorbed H_2S reacts with CO_2 presumably to form COS which causes an apparent increase in the CO_2 capacity by the chemisorbents after exposure to H_2S.

These qualitative results suggest that these chemisorbents cannot be exposed to trace SO_2 or H_2S impurities in the TSSER feed gas, and they must be removed by a conventional method using a pretreatment system.

5.1 Background

The thermal swing sorption enhanced reaction (TSSER) concept has been extensively studied for direct production of fuel-cell grade H_2 by (a) low temperature steam methane reforming (SMR) and (b) water gas shift (WGS) of synthesis gas produced by coal gasification.[32-35] The concept carries out the SMR or the WGS reaction in a single sorber-reactor containing an admixture of a SMR or WGS catalyst and a CO_2 selective chemisorbent such as K_2CO_3 promoted hydrotalcite for SMR-TSSER and Na_2O promoted alumina for WGS-TSSER in order to remove the by-product CO_2 from the reaction zone, thereby circumventing the thermodynamic limitations of these reactions.

The purpose of this communication is to report on the tolerance of these chemisorbents to exposure to trace SO_2 and H_2S. The goal is to find out whether trace sulfur impurities (e.g. SO_2

and H_2S), which are generally present in the feed gas to SMR and WGS reactors, have to be removed by employing traditional desulfurization methods such as selective sorption on ZnO[36,37] prior to their introduction to the TSSER sorber-reactors.

5.2 Experimental protocol

The tests were conducted using a small adsorber containing about a gram of the chemisorbent, passing a stream of 15 % CO_2 in N_2 at near ambient pressure and a temperature of 250 to 400 ^oC over the chemisorbent, and monitoring the effluent gas CO_2 concentration with time, and cyclically repeating the experiment after exposing the sorbent with a trace amount of SO_2 (~1,000 ppm in N_2) and H_2S (~190 ppm in N_2) for a period of time. The specific CO_2 capacities of the chemisorbent (moles/kg) were estimated by integration of the effluent gas concentration - time profiles. Desorption of the sulfur compounds by N_2 purge at the temperature of sorption was also tested periodically.

A laboratory scale sorption system was designed and built for the experimental study. Figure 18 is a schematic drawing of the system. It consists of a gas pre-heater, a gas humidifier, an adsorption vessel, a condenser cooler, a water trap, a filter, a GOW MAC CO_2 analyzer, a trace sulfur analyzer (BW Extreme Single Gas Monitor) and a sulfur scrubber. The entire system was placed inside a safety-certified hood. A data control and acquisition system was also built for the system. Figure 19 shows a photograph of the apparatus.

The feed gas to the adsorber was at 1.4 bar pressure and pre-heated to the sorption temperature. Gas flow rates were measured by using Omega rotameters. Temperatures (preheater, adsorber, and condenser cooler) were measured by Omega sheathed K-type thermocouples. The adsorber was operated isothermally at the desired temperature (200 – 400

^{o}C) by heating it with wrapped heating tapes and employing an Omega temperature controller (CNi3244). The effluent gas from the adsorber was sent to the gas analyzer (GOW MAC for CO_2 or sulfur analyzer for SO_2 or H_2S), and then to the sulfur scrubber before venting into the hood. The measured temperature and gas concentration data were collected by a PC through data acquisition board.

The sorption capacities of bulk CO_2 (15 % in N_2) and then trace SO_2 (1,000 ppm in N_2) or H_2S (190 ppm in N_2) on the chemisorbents were measured first. The capacity of bulk CO_2 in presence of pre-sorbed sulfur compounds on the chemisorbent was then measured by carrying out the following sequential tests:

Expose freshly regenerated chemisorbent to bulk CO_2 in N_2, followed by desorption of CO_2 by N_2 purge, followed by exposing the sorbent to trace sulfur compound in N_2, followed by desorption of sulfur compound by N_2 purge, followed by re-exposure of the sorbent to bulk CO_2 in N_2, and then repeating the sequence for many times. The CO_2 capacity on the sorbent can thus be estimated before and after exposure of the chemisorbent to sulfur compounds.

The cyclic tests were conducted at 400 ^{o}C using the K_2CO_3 promoted hydrotalcite and at 250 and 400 ^{o}C using the Na_2O promoted alumina. The gas flow rates used in all experiments was ~ 90 cc/min. The dead volume of the apparatus was measured by blank tests using helium before each test.

5.3 Results and discussions

Sorption of trace SO_2 and H_2S from N_2 on the chemisorbents

Figure 20 shows the typical adsorber effluent gas SO_2 composition as a function of time for tests using fresh samples of the chemisorbents. The ordinate represents normalized SO_2

concentration (y/y^o) where y^o is the feed gas SO_2 concentration (=1,000 ppm). The tests show that SO_2 is sorbed by both chemisorbents. The estimated capacities of SO_2 on the promoted alumina were, respectively, 0.09 and 0.06 moles/kg at temperatures of 250 and 400 ^oC. The capacity of SO_2 on the promoted hydrotalcite was 0.02 moles/kg at 400 ^oC.

The very diffused nature of the effluent gas concentration profiles in Figure 20 indicates that the kinetics of sorption of trace SO_2 on the promoted alumina is rather slow. The promoted hydrotalcite, which has a much less capacity for sorption of trace SO_2 than the promoted alumina at 400 ^oC, exhibits a relatively faster kinetics of sorption of SO_2.

A very interesting result of these tests was that the sorbed SO_2 could be completely desorbed by N_2 purge alone albeit requiring a very large amount of purge gas indicating very strong sorption and probably slow kinetics of desorption. However, the sorption was not irreversible.

Trace H_2S (190 ppm in N_2) was also sorbed by both chemisorbents at 250 - 400 ^oC but no specific sorption capacity could be measured because of very high capacity requiring a very long time for H_2S to appear in the effluent gas from the sorber. On the other hand, the sorbed H_2S could be desorbed by a very prolonged N_2 purge exhibiting reversibility of H_2S sorption on both chemisorbents.

Effect of trace SO_2 on CO_2 chemisorption

Figure 21 shows cyclic pattern of CO_2 chemisorption capacities on the chemisorbents before and after exposure to SO_2 on Na_2O promoted alumina at 250 and 400 ^oC and on K_2CO_3 promoted hydrotalcite at 400 ^oC. It may be seen that the effective CO_2 capacities were significantly reduced after the exposure of SO_2. However, Figure 21 also shows that the CO_2

chemisorption capacity was restored after desorption of SO_2 from the chemisorbent using prolonged N_2 purge for about 12 hours. The CO_2 sorption capacities appear to become stable after several cycles of operation, albeit at a significantly reduced level compared to that of the fresh material due to the exposure to trace SO_2.

Effect of H_2S on CO_2 adsorption

Limited cyclic tests similar to those described by Figure 21 were also carried out using trace H_2S (193 ppm in N_2) exposure to the promoted alumina at 250 ^oC and measuring the CO_2 sorption capacities before and after the exposure. Figure 22 summarizes the results.

It may be seen from Figure 22 that there is initially a drop in the CO_2 chemisorption capacity after exposure to trace H_2S, but there after the CO_2 capacity increases with repeated exposure to H_2S. It may be surmised that the sorbed H_2S reacted with CO_2 to presumably form COS ($H_2S + CO_2 = H_2O + COS$) which causes an apparent increase in the CO_2 capacity by the chemisorbents after exposure to H_2S. The chemisorbent may have even catalyzed this reaction. Further work is needed to verify this hypothesis.

Scanning Electron Microscopy (SEM)

SEM images were taken to look at the surfaces of chemisorbents before and after exposure to the sulfur compounds SO_2 and H_2S. Figure 23 shows SEM images for Na_2O promoted alumina of (a) before exposure, (b) after exposure to SO_2 and (c) after exposure to H_2S. Figure 24 shows images for K_2CO_3 promoted hydrotalcite of (a) before exposure and (b) after exposure to H_2S. In the future we will be able to perform a qualitative chemical analysis of

the surfaces using the SEM and that will be reported in a future report once the proper way of carrying this analysis is decided.

5.4 Summary

This report presents the results of an experimental study to evaluate the tolerance of two CO_2 selective chemiorbents (K_2CO_3 promoted hydrotalcite and Na_2O promoted alumina) to exposure to trace SO_2 and H_2S with respect of their CO_2 capacities. The CO_2 capacities on these chemisorbents were measured cyclically before and after exposure to trace SO_2 and H_2S with desorption of the sulfur compounds by N_2 purge in between.

The results indicate that (a) SO_2 is sorbed on both chemisorbents, and the effective CO_2 capacities are significantly reduced after the exposure to SO_2,(b) the sorbed SO_2 can be desorbed by very prolonged N_2 purge, thereby restoring the CO_2 capacity nearly fully, which indicates reversible but very slow desorption of SO_2, and (c) H_2S is also sorbed on both chemisorbents, and the sorbed H_2S presumably reacts with CO_2 to form COS , thus causing an apparent increase in the CO_2 capacity by the chemisorbents after exposure to H_2S.

These qualitative results suggest that these chemisorbents cannot be exposed to trace SO_2 or H_2S impurities in the TSSER feed gas, and they must be removed by a conventional method such as selective sorption on ZnO employing a pretreatment system.

6. Experimental Study of CO_2 Adsorbent Surfaces by Temperature Programmed Techniques and Spectroscopy

The research carried out in our laboratories for the last five years has been focused on the characterization and practical application of two different chemisorbent materials that chemisorb CO_2 at high temperatures. The materials are Na_2O-promoted Al_2O_3 (150-450°C)[31] and K_2CO_3-

promoted hydrotalcite (400-590°C).[30] Both materials display unique properties in that both exhibit infinite selectively over other gases such as N_2, H_2O, CH_4, and H_2. The chemisorption process is reversible, allowing for repeated cycling of the material. The materials both exhibit relatively low isosteric heats of chemisorptions (64.9 kJ/mol on Na_2O-alumina, 20.9 kJ/mol on K_2CO_3 hydrotalcite) when compared with bulk CO_2 sorbents such as CaO which facilitates the subsequent desorption of CO_2 from the materials. This is an important property, as a practical adsorption system requires that the adsorbent be regenerated so the material can be reused in subsequent cycles of adsorption/desorption with heat being removed at low temperature to dissipate the heat of adsorption, and heat added at higher temperatures to supply the heat of adsorption for CO_2 removal. The kinetics of CO_2 sorption on these sorbents has been found to be rapid, and they have both have stable sorption capacities upon repeated cycling. The materials exhibit decent cyclic CO_2 sorption capacities at high temperatures (150-450°C for Na_2O-alumina and 400-550°C for K_2CO_3-hydrotalcite), and the measured sorption isotherms have a favorable shape. These properties have made the two materials attractive for use in several cyclic sorption processes, such as sorption enhanced reactions[1,2,32,33,36,] and CO_2 separation from flue gases,[37,38] that have great potential for finding use in practical systems.

Despite the large amount of experimental and simulated data collected on these materials, the actual surface structures that interact with the CO_2 molecule are generally unknown. In the last 30 years, new and more refined characterization techniques have become available to analyze the complex surfaces of metal oxide supported materials. Metal oxide supported systems are much more complex than metal-based systems due to the potential for the presence of multiple oxidation states, variable local coordination, mixed bulk and surface phases, and different surface termination functionalities. The use of IR[39-42]/Raman[39,41-45]/UV-vis Diffuse

Reflectance[39,42-45] spectroscopy, nuclear magnetic resonance (NMR),[39,44-46] chemical probes,[39,47-49] X-ray absorption spectroscopy,[39] and temperature programmed desorption (TPD)[39,50] techniques have now allowed for the determination of the surface structures present on catalytic and adsorbent materials.

The literature contains many examples of the use of spectroscopy and other characterization techniques to analyze the surfaces of bare and supported Al_2O_3 surfaces[39-41, 43,49,51] as well as bare and promoted hydrotalcites[48,52-55], but most of the promoters examined have been transition metal oxides and very little exists in the literature concerning our particular materials. The knowledge of the surface composition would allow for the determination of the actual CO_2 reaction mechanism on the materials. This work uses a combination of surface characterization techniques to elucidate the chemical nature of the activechemisorption sites of both Na_2O-promoted Al_2O_3 and K_2CO_3-promoted hydrotalcite. The fundamental knowledge of the surface will allow for the future synthesis of optimized Na_2O-alumina and K_2CO_3-hydrotalcite for CO_2 adsorption

6.1 Experimental Description

Temperature Programmed Desorption (TPD)

Temperature Programmed Desorption (TPD) is a technique that is used frequently in the analysis of heterogeneous catalysts and adsorbent materials. It gives insight into the number and types of different sorption sites available on the material. A new apparatus to carry out TPD measurements was constructed by the author and is shown in Figures 25 & 26. The apparatus is built on a cage constructed from angle iron. Two Alicat mass flow controllers (Alicat Scientific, model MC flow controllers, Tuscon Arizona) deliver the gas into the system. The gas flows

through steel tubing and through a ½" tube that serves as the reaction column. This tube is ~8" in length and is sealed at both ends with VCR fittings to prevent leakage. The tube has a thermocouple bored into the sidewall about 6.5" from the front end of the column. This allows accurate monitoring of the temperature inside the adsorbent bed. The gas leaves the column, passes through a pressure gauge, and then into a Pfeiffer Quadrupole Mass Spectrometer (model QME200, Pfeiffer Vacuum Inc.,) for accurate analysis of the effluent gas. A needle valve is used to control the flow of gas into the mass spectrometer. The system pressure is generally held slightly above atmospheric (1.07 atm) to ensure that gas properly flows through the system and into the mass spectrometer, and the pressure is controlled using the aforementioned needle valve. The mass spectrometer has been calibrated to detect CO_2 in N_2 mixtures; CO_2 is the adsorbate and N_2 is both the carrier and purge gas for the TPD experiments. An Omega (model CNi44, Omega Engineering, Inc.,) temperature controller receives the temperature signal from the thermocouple and sends the appropriate control output to a heating tape that is wrapped around the column. The heating tape is wrapped with insulation to minimize heat losses and allow for near-isothermal column operation.

A typical TPD experiment is carried out in the following manner: The column is packed with non-porous alumina pellets until just below the thermocouple. This material does not react with the gas, it serves to distribute gas flow and maintain a uniform column temperature. A ceramic wool plug is placed on top of the non-porous alumina layer. When looking into the top end of the column, the thermocouple is visibly sitting just above the wool plug. Approximately 1g sorbent (either Na_2O Alumina or K_2CO_3 Hydrotalcite) is then situated on the thermocouple,

assuring that it is completely covered in sorbent material. This is critical to accurately know the bed temperature during the experiment. Another wool plug is placed on top of the sorbent, and the remaining column section is packed with more non-porous alumina. The materials were heated in 50 mL/min N_2 to 450°C to purge off any adsorbed water, usually for 2-4 hours or until only N_2 is detected in the Mass Spectrometer. The column is then brought to an appropriate CO_2 sorption temperature (250°C for the alumina or 400°C for the hydrotalcite). The gas flow is lowered to 25 ccm and the pressure is allowed to stabilize at ~1.07 atm by adjusting the needle valve. The feed gas is then switched from pure N_2 to a feed gas containing from 40%- 80% CO_2 in N_2. The data acquisition system is started at this point and measures feed gas flow rates, sorbent temperature, and mass spectrometer signals for CO_2 and N_2. The sorbent is allowed to saturate with CO_2 for 30-60 minutes. Following saturation, the data acquisition is turned off. The column is then cooled down to room temperature under the flowing CO_2 and N_2 mixture. This ensures that the CO_2 is not desorbed from the surface during the cool down process, however, more CO_2 is adsorbed as the sorbent bed cools. This additional CO_2 does not alter the results of the TPD experiment.

Once the column is cooled to room temperature (22-30°C), the feed is switched to pure N_2. After purging the void gas from the system, the CO_2 signal reaches a steady value. At room temperature, the CO_2 will not desorb from the material, and this is confirmed by a rapid rise and fall of CO_2 signal coming only from void gas CO_2. The data acquisition system is then turned on, and the temperature controller is manually controlled to achieve a linear column temperature ramp up to ~600°C. An example of a typical temperature ramp is shown in Figure 27. When

exposed to the temperature ramp, the CO_2 desorbs from the material, and different species of adsorbed CO_2 display a maximum in the Mass Spectrometer signal at different temperatures. This gives insight into the types and number of adsorbed species on the material.

Temperature Programmed Surface Reaction (TPSR) Using Methanol

The new TPD unit has also been used to investigate the chemical nature of the surfaces of both materials using methanol as a probe molecule in Temperature Programmed Surface Reaction (TPSR) experiments. These experiments are executed almost identically to the CO_2 TPD experiments described before, except that Ar is used in place of N_2 to avoid the overlapping mass/charge signals that would occur if N_2 were used as purge gas. The primary mass/charge signal for each species to be detected is monitored in the MS, and the fragmentation products created in the MS are not utilized in these experiments. The feed gas of 25 mL/min Ar is bubbled though a sealed container of methanol (CH_3OH) that is held at 0°C by submerging the container in an ice water bath. The temperature of the bath was measured by a thermometer placed in the ice water bath. The Ar is thus saturated with methanol vapor (P_{vap} = 0.039 atm at 0°C), and is passed through the column containing sorbent held at 100°C to allow the methanol to adsorb on the material. The sorbent was allowed to saturate with methanol until breakthrough was observed in the Mass Spectrometer. The column is then cooled down to room temperature under the flowing Ar and methanol mixure. Once the column is cooled to room temperature (22-30°C), the feed is switched to pure Ar by bypassing the methanol container using a set of ball valves. After purging the void gas from the system and only Ar is detected from the system, the

data acquisition system is then turned on, and the temperature controller is manually controlled to achieve a linear column temperature ramp up to ~600°C. Figure 27 shows a typical experimental temperature ramp, and the heating rate is generally ~16 °C/min. The effluent is monitored by the mass spectrometer which has been set up to monitor several mass/charge (m/e^-) ratios, including $m/e^- = 2$ for detection of H_2, $m/e^- = 28$ for detection of CO, $m/e^- = 30$ for detection of formaldehyde (CH_2O), $m/e^- = 31$ for detection of methanol, $m/e^- = 44$ for detection of CO_2, and $m/e^- = 45$ for detection of dimethyl ether (DME, CH_3OCH_3). The products formed by the desorption of methanol are dependent on the chemical nature of the sorption sites, and different types of sites (redox, acidic, basic) give rise to different products.

In methanol TPSR, the formation of CO, CO_2, and H_2 correspond to methanol reacting on basic surface sites. The formation of formaldehyde (H_2CO) corresponds to methanol reacting on surface redox sites. It should be noted that in these TPSR experiments, a signal for m/e^- was detected but it always followed the same trend as the $m/e^- = 31$ (methanol), so it can be said that the $m/e^- = 30$ in this case is associated with the breakdown of methanol inside the MS chamber and not with the formation of formaldehyde. Dimethyl ether can also be formed by methanol reacting on surface acidic sites.

Diffuse Reflectance Infrared Fourier Transform Spectroscopy (DRIFTS) and Raman Spectroscopy

The Infrared Spectra of the promoted materials were examined using a ThermoScientific Nicolet 8700 IR Spectrometer (Thermo Fisher Scientific, Waltham, Massachusetts). A few

pellets of the Na_2O promoted Alumina (or K_2CO_3 promoted hydrotalcite) were crushed into a powder and placed into the sample holder of a Harrick cell. This cell was placed in a Praying Mantis Window attachment for acquisition of the DRIFT spectrum of the material. The Harrick cell was connected to a temperature controller to heat up the sample while water cooling lines were attached to allow for cooling the cell. A gas inlet connected the cell to gas cylinders to allow for *in situ* monitoring of the spectra when the sorbent was exposed to CO_2. The sample was initially heated to 400°C at 10°C/min in 15 mL/min 99% O_2 in Helium (from gas cylinder) and held there for ~1 hour, until the observed IR spectrum no longer changed. A spectrum was acquired approximately every 1.5 min during this period.

Once the dehydration spectrum of the sample was obtained and full dehydration was achieved, the sorbent temperature was set to an appropriate sorption temperature (200°C for industrial and synthesized Na_2O promoted alumina and 400°C for K_2CO_3 promoted hydrotalcite). After stabilization of the temperature, the gas feed was switched to 5 mL/min of pure CO_2 obtained from a gas cylinder. An initial IR spectrum was obtained prior to CO_2 exposure, and a new spectrum was obtained every 1.5 min for approximately 1 hour. Each spectra taken during CO_2 exposure was subtracted from the initial spectrum for ease of interpreting the experimental data.

An attempt to measure the Raman spectra of both the Na_2O promoted alumina and K_2CO_3 promoted hydrotalcite was made with a high resolution, dispersive Raman spectrometer system (Horiba-Jobin Yvon LabRam HR) equipped with three laser excitation wavelengths (532, 442, and 325 nm). The visible laser at 532 nm (green) was generated by a Coherent Compass

315M-150, Nd:YAG double diode pumped laser (output power of 150 mW, power at the sample of 10 mW). The visible laser at 442 nm (violet) and the UV laser at 325 nm (not visible) were generated by a He-Cd laser (Kimmon, model IK5751I-G; 441.6 nm output power of 110 mW, power at sample of 28 mW; 325.0 nm output power of 30 mW, power at sample of ~7 mW). The green laser (532 nm) was used to collect Raman spectra, and the laser was focused on the samples with a confocal microscope equipped with a 50X long working distance objective (Olympus BX-30- LWD) for the visible lasers and 15X objective (OFR LMU- 15X-NUV) for the UV laser. The LabRam HR spectrometer was optimized for the best spectral resolution by employing a 900 groves/mm grating (Horiba-Jobin Yvon 51093140HR) for the visible lasers and a 2400 grooves/mm grating (Horiba-Jobin Yvon 53011140HR) for the UV laser. The resolution for both gratings is ~2 cm^{-1}. The optimal resolution, or minimum number of data points required to resolve a Raman band, is based on the grating and laser excitation energy. For the 900 grooves/mm grating, the achievable resolution is 1.88 cm^{-1} (532 nm) and 2.76 cm^{-1} (442 nm), and for the 2400 grooves/mm grating, it is 1.76 cm^{-1} (325 nm). The Rayleigh scattered light was rejected with holographic notch filters (Kaiser Super Notch). The notch filter window cutoffs were ~100 cm^{-1} with the visible lasers and ~300 cm^{-1} with the UV laser. The scattered light, after removing the Rayleigh scattering, was directed into a UV-sensitive liquid N_2 cooled CCD detector (Horiba-Jobin Yvon CCD-3000V). The calibration of each laser line was performed with an Hg lamp by adjusting the groove gratings to match the zero position and minimize the error of the linearity across the full Raman spectrum range. The Hg lines chosen to represent the 532, 442, and 325 nm lasers were 546.07, 441.6, and 365.02 nm, respectively. Additionally, wavenumber calibration of the Raman spectrograph was checked using the silicon line at 520.7 cm^{-1}.

The sorbent pellets were placed in an environmentally controlled high-temperature cell reactor (Linkam TS1500) containing a quartz window and O-ring seals that were cooled with flowing cooling water. The sample temperature was controlled by a temperature controller (Linkam TMS94), providing linear heating rates of over 50 °C/min through an S-type thermocouple (Pt 10% Rh/Pt, accuracy of 1.5 °C from 0 to 1450 °C). The sorbent bed temperature, however, was calibrated externally with a second thermocouple (K type: Ni-Cr/Ni-Al, accuracy of 2.2 °C from -200 to 1250 °C). Typical reactor cell conditions were room temperature (RT) - 400 °C, 10-20 °C/min heating and cooling rates, atmospheric pressure, and ~40 sccm gas flow rates metered by mass flow controllers (Brooks, Model 5850E series).

The protocol for obtaining *in situ* Raman spectra under an Ar environment was as follows. The sample was initially heated at a rate of 10 °C/min in the *in situ* cell to 400 °C and held for 45-60 min under flowing Ar obtained from a gas cylinder. For the acquisition of the Raman spectra, only the laser angles parallel to the incident beam were allowed to hit the catalyst sample, where the accumulation was collected at 10 s/scan for 7 scans with a 200 micrometer size hole. The Raman spectra were collected with the 532 nm laser.

An attempt was made to use the Operando *in situ* Raman System to look at the Na_2O promoted alumina surface, but no signal was able to be obtained from this material even after several different lasers were tried.

6.2 Experimental Results & Discussion of Na_2O promoted Alumina

DRIFTS and Raman Analysis

The dehydrated DRIFTS of both the industrial Na_2O promoted alumina and a high surface area bare γ-alumina (~200 m^2/g) obtained from Engelhard (Engelhard, now of BASF Catalyst

LLC., 25 Middlesex-Essex Turnpike, Iselin, NJ) appears in Figure 28. On the γ-alumina four bands are observed in the hydroxyl region at 3762, 3723, 3675, and 3566 cm^{-1} and the positions of these peaks corresponds well with earlier DRIFTS studies on γ-alumina.[51] The band at 3762 cm^{-1} is corresponds with a type I_6 OH group, the 3723 cm^{-1} band with a type II_{66} OH group, and the 3675 cm^{-1} band with a type III OH group. The 3566 cm^{-1} band has been attributed to hydrogen bonded –OH groups. The Roman numerals in these assignments indicate how many surface Al^{3+} ions are associated with the particular hydroxyl group. The subscript of the Roman numeral indicates the coordination of the Al^{3+} ion. For example, II_{66} means that the hydroxyl group is attached to two tetrahedrally coordinated Al ions.[51] The literature has noted that usually five different bands are seen in the hydroxyl region, but only four were observed on the sample in question in this work. A missing band at 3512 cm^{-1} could be explained by the broad shape of the peak seen at 3566 cm^{-1}. It may be overlapping the peak at the lower wavenumber. The literature still debates the exact assignments for these bands.[51]

The dehydrated DRIFTS spectra of Na_2O promoted alumina shows the evolution of different surface structures as indicated by the new bands in Figure 28. Bands at 1571 and 1353 cm^{-1} are observed and are attributed to a carboxylate species. The hydroxyl band at 3723 cm^{-1} indicates that there are still some (although a very small amount) hydroxyl groups situated on an exposed aluminum site on the material as evidenced by the presence of this band at the exact same position on the bare γ-alumina. There also remains a very broad band centered at 3457 cm^{-1} which is due to hydroxyl groups shifting from sitting on aluminum to sitting on sodium on the surface. Figure 29 shows a picture of a carboxylate species and also the IR bands associated with this structure.[56] After stabilization of

the temperature at 200°C, the gas feed was switched to 5 mL/min of pure CO_2 obtained from a gas cylinder. An initial IR spectrum was obtained prior to CO_2 exposure, and a new spectrum was obtained every 1.5 min for approximately 1 hour. Each spectra taken during CO_2 exposure was subtracted from the initial spectrum. The flat line at the bottom of the figure is the sorbent prior to CO_2 exposure.

Figure 30 shows the results of CO_2 sorption on γ-alumina. Several of the peaks (3730, 3702, 3625, and 3597 cm^{-1} as well as the band between ~2250-2400 cm^{-1}) are attributed to gas phase CO_2. Three other peaks are observed and are located at 1653, 1438, 1228 cm^{-1}. These three peaks are respectively assigned to the ν_{as} vibration of bicarbonate, the ν_s vibration of bicarbonate, and the γ vibration of a hydroxyl group associated with the bicarbonate species.

Figure 31 shows the DRIFTS of the industrially produced Na_2O promoted alumina during CO_2 adsorption. The evolution of several peaks was observed as the material was exposed to more and more CO_2. The peaks located at3730, 3702, 3625, and 3597 cm^{-1} as well as the band between ~2250-2400 cm^{-1} are attributed to gas phase CO_2. Four other peaks evolve and are located at 1654, 1524, 1407, and 1313 cm^{-1}.

In the first scan following exposure to CO_2, two peaks centered at 1654 and 1313 cm^{-1} are seen as small humps, and these have been attributed in the literature to the ν_s and ν_{as} vibrations of a bidentate species of adsorbed CO_2. The band split has $\Delta\nu = 341$ cm^{-1}, and as reported by Biusca and Lorenzelli, this Δν value corresponds well with a bidentate species.[57] In the next few scans, these peaks grow, and we see two more bands take form centered at 1523 and 1407 cm^{-1}. These bands have been assigned to the ν_s and ν_{as} vibrations of a monodentate species of adsorbed

CO_2 and the observed band splitting value of $\Delta\nu = 116$ cm^{-1} matches well with the literature values for a monodentate species.[57]

The concept of band splitting is a useful measure of the effect of coordination of the surface species to the metal on the surface.[58] Coordination causes shifts in the spectrum according to the vibrational modes. When coordination lowers the symmetry of the ligand, new vibrations of the ligand are allowed, and degenerate vibrations are split. A stronger metal-ligand bond results in a larger splitting of the degenerate mode.[58]

An interesting point to notice is that the bidentate species appears to form before the monodentate species as shown in Figure 31. This observation is consistent with the previously described new CO_2 sorption model that accounts two separate adsorption processes occurring. The model predicts that the first formed, the surface bidentate species, will have a much larger heat of adsorption (64.9 kJ/mol) than the less energetic second species formed, the surface monodentate species with a heat of adsorption of 37.5 kJ/mol. The bidentate species with two oxygens involved with the sodium is expected to have a stronger interaction than a monodentate species where only one oxygen is involved in the bonding.

CO_2 TPD on Industrial Na_2O promoted Alumina

CO_2 TPD experiments performed on the industrially produced Na_2O promoted alumina confirms the presence of energetically different forms of bound CO_2. Figure 32 shows several results of CO_2 TPD from the industrially produced Na_2O promoted alumina and the reproducibility of the results. It can be seen from each of these that three peaks in the CO_2 desorption rate associated with different temperatures occur when the saturated adsorbent is exposed to a linear temperature ramp. Now, the DRIFTS of CO_2 adsorption showed two distinct

structural groups form as CO_2 adsorbed onto the surface yet we see three desorption peaks in the TPD spectra. This can be resolved in the following manner. The highest temperature desorption peak located ~280-285°C is due to the formation of the surface bidentate species as it would be the most stable of the two species observed. The energetically stronger bidentate species would require a higher temperature (and hence energy input) to desorb it from the surface. The next largest desorption peak located ~180-190°C is due to the formation of the weaker surface monodentate species that requires lower temperature and thus lower energy to desorb. It is difficult to quantify the relative amounts fo bidentate and monodentate species from the collected TPD data. The surface area of the CO_2 TPD peaks gives the relative amounts of surface sites corresponding with that particular surface species and it can be seen from the Figure 32 that the higher temperature peak corresponding to the surface bidentate species is the dominant form of bound CO_2. To resolve the final low temperature peak seen around ~75-100°C, it should be noted that this low of a temperature for desorption is indicative of physisorbed CO_2. Due to the much higher temperatures used in the DRIFTS (T=200°C), the physisorbed state of CO_2 would be driven from the material and would not be observable in the spectra.

Methanol TPSR on Industrial Na_2O promoted Alumina

Figures 33-35 show examples of the TPSR studies of methanol on the Na_2O promoted alumina. As can be seen from the figures, the primary products detected in the effluent gas are those associated with surface basic sites, indicated by the formation of CO, CO_2, and H_2. The other main species coming off the material is unreacted methanol. This indicates that the surface is not too strongly basic, and not all of the sorption sites are active enough to convert the adsorbed methanol into other products. Looking at Figures 33-35 four different temperature

peaks are observed for four different gas species. Figurew 36-38 show the TPSR signal peaks for the experimental run shown in Figure 33. The peaks have been separated in these figures for clarification. The first of these is a broad peak associated with desorbed methanol ($m/e^- = 30$ and 31) and centered near 190°C. The methanol adsorbed onto sites that were not chemically active enough to convert the methanol into other products. The second peak is associated with CO_2 ($m/e^- = 44$) and is centered near 300-320°C. This indicates that the methanol was adsorbed on surface basic sites. A third peak is associated with a small amount of dimethyl ether ($m/e^- = 45$), and its signal appears on the right hand axis of Figures 33-35. The intensity for this signal is 3 orders of magnitude lower than that observed for all other detected species, and this means that only a very small fraction of the methanol adsorbed on these surface acidic sites. It should be noted that the formation of dimethyl ether is not a result of it forming in the mass spectrometer, the signal obtained from putting methanol alone through the mass spectrometer did not result in the formation of any dimethyl ether. This acidic reaction product is due to the small amount of hydroxyl groups bonded to exposed aluminum on the surface as evidenced by the previous DRIFTS data. Alumina is known to be an acidic material. The final peak is associated with H_2 and CO ($m/e^- = 2$ and 28) and is centered near 420-440°C, and the relatively large size of these peaks reveals that the majority of the methanol had been adsorbed onto these stronger surface basic sites. The very high temperature peak ($T > 500$°C) seen in Figures 34 and 35 is associated with the decomposition of the material. The strength of the particular sorption sites can be directly related to the temperature at which they desorb; lower desorption temperatures indicate a weaker interaction with the surface. The peaks, except for the dimethyl ether peak associated with a slight amount of surface acidity, correlate well with the TPD data of Figure 33-35. Three adsorbed species from three different sites ranging in bascisity are observed in both TPD and

TPSR studies. As with the TPD data, the low temperature peak seen in TPSR is associated with a physisorbed state of methanol that desorbs unreacted from the surface. The low intensity of the dimethyl ether signal indicates that the while the surface is overall basic, there are a very few sites of acidic nature on the material, but the promoter is dispersed quite evenly over the sorbent surface.

6.3 Experimental Results & Discussion of K_2CO_3 promoted Hydrotalcite

DRIFTS and Raman Analysis

Raman and DRIFT spectra were collected on samples of K_2CO_3 promoted hydrotalcite, and DRIFTS was collected on a bare SASOL hydrotalcite (Puralox MG70). The Raman spectra of the K_2CO_3 promoted hydrotalcite was compared with the spectra of pure K_2CO_3 and the results appear in Figure 39. The very sharp peak seen on both samples centered at 1063 cm^{-1} is characteristic of crystalline K_2CO_3, confirming the presence of the promoter on the surface. The K_2CO_3 promoted hydrotalcite has more than monolayer coverage as indicated by the presence of the crysatalline K_2CO_3. Matching bands are also observed at lower wavenumbers (186, 134, and 116 cm^{-1}). The literature describes several Raman and IR studies on bare hydrotalcites,[52,59] and were consulted to identify some of the remaining peaks seen on the K_2CO_3 promoted hydrotalcite. Klopperage et al[59] report a doublet band at 388 and 303 cm^{-1} associated with a hydroxyl group bonded on aluminum, and we see a similar although shifted doublet occurring at 340 and 316 cm^{-1} corresponding to the same hydroxyl group. The bands at 1402 and 687 cm^{-1} correspond to vibrations arising from the interlayer carbonate in the hydrotalcite structure.[59]

The dehydrated DRIFTS of the bare MG70 hydrotalcite is shown in Figure 40. Initially after heating, peaks are observed to form at 1056, 1323, 1573, and 3723 cm^{-1}. The peaks at 1056, 1323, and 1573 cm^{-1} can be to assigned to the vibration associated with a carbonate species

as has been observed in the literature review by Busca and Lorenzelli.[57] The band observed at 3723 cm^{-1} is assigned to hydroxyl stretching.[59] A decrease in the absorbance intensity at a broad peak centered at 1655 cm^{-1} is observed on this material, and the peak is typical of the O-H bending mode of water.[52] Accordingly, as the material is exposed to a longer period of heat treatment, this band decreases.

Similarities between the K_2CO_3 promoted hydrotalcite and the unpromoted MG70 are observed in the dehydrated DRIFTS. Figure 41 shows the dehydrated DRIFTS of the K_2CO_3 promoted hydrotalcite. After the initial heating period in the first scan from the baseline, the evolution of 4 peaks is observed, with one at 1076, 1424, 1598, and 3698 cm^{-1}. The peaks at 1076, 1424, and 1598 cm^{-1} appear quite similar, albeit somewhat shifted, from those seen on the unpromoted material. These bands are assigned to a surface carbonate species,[57] and the shifted band at 3698 cm^{-1} is associated with hydroxyl stretching.[59] On successive scans, these peaks grow, and are accompanied by the formation of several new peaks at 1783, 1331, and 1043 cm^{-1}. These bands respectively correspond to the ν_{as}, ν_s, and γ_{COO-} vibrations of a bridged carbonato complex, where the carbonate bonds with two of the potassium sites on the surface. This configuration of K_2CO_3 has been suggested by Ogden et al.[60] A picture of a bridged structure appears in Figure 29. Interestingly, a decrease in absorbance is observed at a shoulder centered around 1655 cm^{-1}, and this has been assigned to the O-H bending mode of water.[52] As with the MG70, this band decreases in size as heat treatment proceeds.

Following the dehydration of the samples in the IR unit, the DRIFTS spectra of both materials under exposure to CO_2 was recorded. The spectra recorded during CO_2 adsorption on

MG70 and K_2CO_3 promoted hydrotalcite respectively appear in Figures 42 and 43. In both spectra, the straight line at the bottom is the normalized spectra obtained at the end of the dehydration experiments. This has been done to easily observe the changing surface.

Figure 42 shows how the surface of MG70 evolves as CO_2 adsorbs on the surface. In the first scan, several peaks located at 1224, 1418, and 1669 cm^{-1} are observed to form. The peaks that are forming in the higher wave number region (including the broad band between 2250-2400 cm^{-1} and the peaks centered at 3597, 3625, 3702, and 3730 cm^{-1}) are all attributed to the presence of gas phase CO_2. Evans and Whateley[61] report that the three peaks at 1224, 1418, and 1669 are characteristic of the formation of a bicarbonate species on magnesium oxide. These three peaks are assigned to the ν_{as} vibration of bicarbonate (1669 cm^{-1}) , the ν_s vibration of bicarbonate (1418 cm^{-1}), and the γ vibration of a hydroxyl group associated with the bicarbonate species (1224 cm^{-1}).[57] It is reported as being present in the dimer form as shown in Figure 44. This hydrotalcite contains a large amount of magnesium (70:30 Mg:Al ratio) so this assignment is valid.

Figure 43 shows how the K_2CO_3 promoted hydrotalcite changes during CO_2 adsorption. As with the MG70, the same peaks typical of gas phase CO_2 are observed (broad band between 2250-2400 cm^{-1} and the peaks centered at 3597, 3625, 3702, and 3730 cm^{-1}) in the spectra even after the first scan. Two other peaks that are centered at 1300 and 1672 cm^{-1} begin to form in this scan as well. This band pair has been assigned to a bidentate surface ligand.[62] Smart et al report that the broadness seen around 1670 cm^{-1} suggests that two overlapping bands occur here.[62] This indicates the presence of two separate but similar forms of bidentate surface ligands forming. These bands arise from the C-O stretching modes of the adsorbed bidentate species.

Comparing the promoted and unpromoted hydrotalcites, both have surface carbonates on the dehydrated samples. On the promoted hydrotalcite, some of the carbonates are bonded with two potassium sites on the surface. The promoted material also has crystalline K_2CO_3 as evidenced by Raman spectroscopy and this means that more than monolayer coverage has been achieved on this particular sample. The unpromoted MG70 reacts with CO_2 by forming a surface bicarbonate on the exposed Mg sites, while the K_2CO_3 promoted hydrotalcite reacts with CO_2 by forming two different surface bidentate ligands bonded to the potassium. The potassium behaves similarly to sodium as both are alkali metals and both form bidentate structures with CO_2.

CO_2 TPD from K_2CO_3 promoted Hydrotalcite

CO_2 TPD experiments performed on the K_2CO_3 promoted hydrotalcite also confirms the presence of energetically different forms of bound CO_2. Figure 45 shows examples of several CO_2 TPD experiments from the K_2CO_3 promoted hydrotalcite. These tests were performed in the test unit built by the author shown in Figures 25 and 26. Except for one of the curves (blue, at bottom of chart), these experiments show 3 maximum desorption peaks of CO_2 from the material. The broadness of the peak is due to overlap with another peak near a similar temperature as seen in the rest of the TPD experiments. The DRIFTS of CO_2 adsorption showed that two different bidentate structural groups form as CO_2 adsorbed onto the surface yet three desorption peaks in the CO_2 TPD spectra are observed. This can be resolved in the following manner. The two higher temperature desorption peak located between 420-490°C are due to the formation of the two surface bidentate species. The energetically strong bidentate species would require a higher temperature (and hence energy input) to desorb it from the surface. The two

desorption peaks at different temperatures also confirms the CO_2 adsorption model presented in Chapter 2 in which two separate heats of adsorption have been observed. The lower temperature peak with T_{peak} ~ 420°C corresponds to the first less energetic Langmuirian chemisorptions with a heat of adsorption of 21 kJ/mol, while the higher temperature peak with T_{peak} ~ 490°C corresponds to the second chemical complexing reaction with a higher heat of adsorption of 42.2 kJ/mol.[32] The third low temperature peak observed near 50°C can be resolved in a similar fashion to the Na_2O promoted alumina. This small desorption peak corresponds to some physisorbed CO_2 that would not be present at the much higher temperatures encountered in the DRIFTS studies of the K_2CO_3 promoted hydrotalcite.

Methanol TPSR from K_2CO_3 promoted Hydrotalcite

Figure 46 shows the methanol TPSR spectra of the K_2CO_3 promoted hydrotalcite, and three different temperature peaks are observed for four different gas species. Figures 47-49 show separated signals on different plots from the TPSR experiment. This has been done to easily read the Figures. The first of these is a broad peak associated with desorbed methanol (m/e^- = 30 and 31) and centered at 116°C. This methanol physisorbed onto sites that were not chemically active enough to convert the methanol into other products. The second peak is associated with dimethyl ether (m/e^- = 45) and is centered at 276°C. This indicates that the methanol was adsorbed on surface acidic sites, and its signal appears on the right hand axis of Figure 24. The intensity for this signal is 2 orders of magnitude lower than that observed for all other detected species, and this means that only a very small fraction of the methanol adsorbed on these surface acidic sites. A final peak is associated with a large amount of CO_2 (m/e^- = 44) and it increases past the the temperature limitations of the system and is due to breakdown of the

hydrotalcite structure.[54] The relatively large size of these peaks reveals that the majority of the methanol had been adsorbed onto these stronger surface basic sites. The strength of the particular sorption sites can be directly related to the temperature at which they desorb; lower desorption temperatures indicate a weaker interaction with the surface. The peaks, except for the dimethyl ether peak which will be described later, correlate well with the TPD data of Figure 45. Two adsorbed species from two different sites ranging in bascisity are observed in both TPD and TPSR studies. The low intensity of the dimethyl ether signal indicates that while the surface is overall basic, there are a very few sites of acidic nature on the material, but the promoter is dispersed quite evenly over the sorbent surface.

One issue that has not been addressed yet concerns the TPSR data of Figure 46, which shows a relatively small but clear peak associated with the presence of some small fraction of surface acidic sites. This may be resolved by examining the dehydrated DRIFTS of the K_2CO_3 promoted hydrotalcite in Figure 41, where we see a small vibration in the hydroxyl region at 3698 cm^{-1}. The surface is not completely covered with promoter and a small amount of hydroxyl groups bonded on Al from the hydrotalcite is exposed on the surface, forming acidic sites on the surface that are very small in number.

7. Conclusions

A condenser was modeled by a combination of two differential equations with split boundary conditions and a nonlinear algebraic equation for the interfacial temperature. A numerical scheme was made by using an iterative numerical scheme and a one dimensional finite difference method (FDM) with forward differencing. Process conditions for modeling of case studies were taken with variable flow rates of CO_2 and steam during desorption cycle. A graphical method was also presented by using a bounded constraint diagram which was made by three lines: lines of inlet coolant enthalpy, inlet gas enthalpy and equilibrium temperature. The results of the numerical simulation match well the graphical method of the bounded constraint diagram. Predicted heat recovery rates from the desorption gas side to the cooling water side ranged from 11.3 to 32 %. The heat recovered was best occurred at the beginning of the process when superheated steam was generated.

The CO_2 sorption apparatus was retrofitted with high pressure tolerant mass flow controllers and solenoid valves to allow for measurement of high pressure CO_2 adsorption data. The system was thoroughly leak tested to ensure that no gas leaked. The first high pressure adsorption measurements at a CO_2 partial pressure of 4.1 atm and a temperature of 250°C have shown that high pressure CO_2 sorption data is larger than predicted by the novel analytical chemisorption model proposed for CO_2 sorption. Model parameters were readjusted to better fit the new high pressure sorption data. Future work would include measurement of CO_2 sorption characteristics at even higher pressures than those obtained in this work as it appears that the saturation capacity of the sorbent may increase at higher pressures.

A heat integration scheme and first pass economic evaluation was performed for the 5 step thermal swing sorption enhanced reaction process for the production of 30 MMSCFD fuel cell grade H_2. The system consists of 16 parallel fixed-bed-sorber reactors of shell and tube

design, where the tubes are packed with an admixture of WGS reaction catalyst and Na_2O promoted alumina as the CO_2 chemisorbent. Four of these vessels process synthesis gas at any given time. The calculated capital cost of the system was calculated to be \$0.28/kg of H_2, and the operating costs were calculated to be \$2.08/kg of H_2. The capital cost accounts for the 16 sorber-reactor vessels, CO_2 product compressors for compressing CO_2 to 140 atm for subsequent sequestration, heat exchangers, and chemisorbent/catalyst mixture. The operating costs include the steam for regeneration, the additional heat needed for the thermal swing, and the electrical power needed to compress the recovered CO_2 to pipeline pressure. A credit is taken for the heat recovered by the previously described constant-pressure-condensing heat exchanger modeled for this purpose. This first pass cost analysis shows that the cost of the H_2 produced by the process is not prohibitive; a more detailed economic evaluation including detailed heat integration schemes and real chemical plant cost analysis would be beneficial to get a more detailed understanding of the costs of the TSSER process.

An experimental study was carried out in order to evaluate the tolerance of two CO_2 selective chemiorbents (K_2CO_3 promoted hydrotalcite and Na_2O promoted alumina) to exposure to trace SO_2 and H_2S with respect of their CO_2 capacities. The CO_2 capacities on these chemisorbents were measured cyclically before and after exposure to trace SO_2 and H_2S with desorption of the sulfur compounds by N_2 purge in between. The results indicate that (a) SO_2 is sorbed on both chemisorbents, and the effective CO_2 capacities are significantly reduced after the exposure to SO_2,(b) the sorbed SO_2 can be desorbed by very prolonged N_2 purge, thereby restoring the CO_2 capacity nearly fully, which indicates reversible but very slow desorption of SO_2, and (c) H_2S is also sorbed on both chemisorbents, and the sorbed H_2S presumably reacts with CO_2 to form COS , thus causing an apparent increase in the CO_2 capacity by the

chemisorbents after exposure to H_2S. It should be noted that the formation of COS is irreversible. These qualitative results suggest that these chemisorbents cannot be exposed to trace SO_2 or H_2S impurities in the TSSER feed gas, and they must be removed by a conventional method such as selective sorption on ZnO employing a pretreatment system.

Several techniques were employed to investigate the chemical structures of the surfaces of Na_2O promoted alumina before and during CO_2 to help understand how this material interacts with CO_2. A new experimental apparatus was constructed to perform CO_2 Temperature Programmed Desorption and methanol Temperature Programmed Surface Reaction experiments. Diffuse Reflectance Infrared Fourier Transform Spectroscopy was used as an optical method to see what functionalities are present on both surfaces in the dehydrated state, as well as to learn what complexes form during the CO_2 adsorption process. The dehydrated Na_2O promoted alumina was found to have carboxylate on the surface in addition to a small amount of acidic hydroxyl groups as confirmed by TPSR and DRIFTS. When exposed to CO_2 the surface reacts to form two different structures. The first to form is a more stable bidentate structure followed a short time after by a less stable monodentate structure. This is consistent with the newly proposed CO_2 sorption model previously developed for this material. The first heat of adsorption is calculated to be 64.9 kJ/mol while the milder heat of complexation is measured to be 37.5 kJ/mol[24] and the difference in energy is attributable to the stronger bonding of the bidentate structure. Raman Spectroscopy was not able to be used as the surface was Raman inactive. The promotion of the alumina substrate altered the surface species formed during CO_2 adsorption. On bare γ-alumina, bicarbonate species were formed. Upon promotion the hydroxyl

groups on aluminum disappeared, and the surface structures formed during CO_2 adsorption changed to bidentate and monodentate structures.

The dehydrated K_2CO_3 promoted hydrotalcite was found to have some crystalline K_2CO_3 dispersed on the surface as shown by Raman Spectroscopy. DRIFTS also revealed the presence of multiple functionalities on the surface such as surface carbonates and a small amount of acidic hydroxyl from exposed hydrotalcite. Some of the surface carbonato complexes are coordinated on one potassium while others are coordinated on two potassium. When exposed to CO_2 the surface develops two forms of bidentate surface ligands. This correlates well with the proposed analytical sorption model previously developed for this material. Two heats of adsorption have been observed by calorimetry[3], and the DRIFTS shows that indeed two different sorption processes are occurring on the surface of the K_2CO_3 promoted hydrotalcite. The promotion of the hydrotalcite substrate altered the surface species formed during CO_2 adsorption. On the Puralox MG70, bicarbonate species were formed coordinated on Mg. The K_2CO_3 promoted hydrotalcite formed multiple bidentate species coordinated with potassium during CO_2 adsorption.

References

[1] Lee, K.B., M.G. Beaver, H.S. Caram and S. Sircar, Reversible chemisorptions of carbon dioxide: simultaneous production of fuel-cell grade H2 and compressed CO2 from synthesis gas, Adsorption, Vol. 13, pp. 385-397, 2007

[2] Lee, K.B., M.G. Beaver, H.S. Caram and S. Sircar, Performance of Na2O promoted alumina as CO2 chemisorbent in sorption-enhanced reaction process for simultaneous production of fuel-cell grade H2 and compressed CO2 from synthesis gas, Journal of Power Sources, Vol. 176, Issue 1, 2007

[3] Webb, Ralph L. and A. S. Wanniarachchi, The effect of noncondensible gases in water chiller condensers – Literature survey and theoretical predictions, ASHRAE Transactions, Vol. 80, pp. 142-159, 1980

[4] Osakabe, M., T. Itoh and K. Yagi, Condensation heat transfer of actual flue gas on horizontal tubes, Proceedings of the 5th ASME/JSME Joint Thermal Engineering Conference, 1999

[5] Osakabe, M., Thermal-hydraulic behavior and prediction of heat exchanger for latent heat recovery of exhaust flue gas, Proceedings of the ASME Heat Transfer Division, Vol. 2, 1999

[6] Osakabe, M., Latent Heat Recovery from Oxygen-Combustion Flue Gas, Energy Conversion Engineering Conference and Exhibit, Vol. 2, pp. 804-812, 2000

[7] Osakabe, M., K. Yagi, T. Itoh and K. Ohmasa, Condensation Heat Transfer on Tubes in Actual Flue Gas (Parametric Study for Condensation Behavior), Heat Transfer – Asian Research, Vol. 32, 2003

[8] Oh, S., S.T. Revankar, Investigation of the noncondensable effect and the operational modes of the passive condenser system. Nucl. Technol. 152, 71–86., 2005

[9] Oh, S., S.T. Revankar, Effect of noncondensable gas in a vertical tube condenser. Nucl. Eng. Des. 235, 1699–1712., 2005

[10] Oh, S., S.T. Revankar, Complete condensation in a vertical tube passive condenser. Int. Commun. Heat Mass Trans. 32, 593–602., 2005

[11] Lee, Kwon-Yeong and Moo Hwan Kim, Modeling of condensation heat transfer for a PRHRS heat exchanger in a SMART-P plant, Nuclear Engineering and Design, Vol. 238, pp. 3252-3262, 2008

[12] Jeong, K., Condensation of water vapor and sulfuric acid vapor in boiler flue gas, Ph.D. dissertation, Lehigh University, ISBN 9781109121285, 2009

[13] Jeong, K., M. Kessen, H,. Bilirgen and E.K. Levy, Analytical modeling of water condensation in condensing heat exchanger, Vol. 53, Issue 11-12, pp. 2361-2368, 2010

[14] Schrock, V.E. and L.M. Grossman, Forced convection boiling in tubes, Nuclear science and engineering, Vol. 12, pp. 474-481, 1962

[15] Wojtan, Leszek, T. Ursenbacher, J.R. Thome, Investigation of flow boiling in horizontal tubes: Part I – A new diabatic two-phase flow pattern map, I. J. of Heat and Mass Transfer, Vol. 48, pp. 2955-2969, 2005

[16] Wojtan, Leszek, T. Ursenbacher, J.R. Thome, Investigation of flow boiling in horizontal tubes: Part II – Development of a new heat transfer model for stratified-wavy, dryout and mist flow regimes, I. J. of Heat and Mass Transfer, Vol. 48, pp. 2970-2985, 2005

[17] Mori, H., S. Yoshida, K. Ohishi, Y. Kokimoto, Dryout quality and post dryout heat transfer coefficient in horizontal evaporator tubes, Proc. Of 3rd European Thermal Sciences Conference, pp. 839-844, 2000
[18] Colburn, A. P. and O. A. Hougen, "Design of Cooler Condensers for Mixtures of Vapors with Noncondensing Gases", Ind. Eng. Chem., Vol. 26, pp. 1178-1182, 1934
[19] A.P. Colburn, Trans. Am. Inst. Chem. Eng., Vol. 29, pp. 174, 1933
[20] T.H. Chilton and A.P. Colburn, Ind. Eng. Chem., Vol. 26, pp. 1183, 1934
[21] K. Stephan, Heat Transfer in Condensation and Boiling, Springer-Verlag, NewYork, 1992
[22] F.P. Incropera, D.P. Dewitt, T.L. Bergman, and A.S. Lavine, Fundamentals of Heat and Mass Transfer, 6th Edition, Wiley, 2007
[23] A. Zhukauskas, Heat Transfer from Tubes in Cross Flow, Advances in Heat Transfer, Vol. 8, Academic Press, New York, 1972
[24] V. Gnielinski, Int. Chem. Eng., Vol. 16, pp. 359-368, 1976
[25] Morooka, Shin-ichi, Nobuhiko Inai, Tohimi Tobimatsu, "Experimental Investigation of Heat Transfer in BWR LOCA", Journal of Nuclear Science and Technology, Vol. 18(6), pp. 473-475, 1981
[26] Thermophysical Properties of Fluid Systems, NIST, http://webbook.nist.gov/chemistry/fluid/
[27] Hoffman, J.S., Richards, G.A., Pennline, H.W., Fischer, D., Keller, G., "Factors in Reactor Design for Carbon Dioxide Capture with Solid Regenerable Sorbents," Clearwater Coal Conference, Clearwater, FL 2008
[28] Seider, W.D., Seader, J.D., Lewin, D.R., *Product and Process Design Principles: Synthesis, Analysis, and Evaluation.* Wiley, New York, 2004
[29] Smith & Varbanov, "What's the Price of Steam?" CEP, July 2005, pp 29-33
[30] Lee KB, Verdooren A, Caram HS, Sircar S. Chemisorption of carbon dioxide on potassium-carbonate-promoted hydrotalcite. J Colloid Interface Sci, 308(1):30-39, 2007
[31] Lee KB, Beaver MG, Caram HS, Sircar S. Chemisorption of Carbon Dioxide on Sodium Oxide Promoted Alumina. AIChE J., 53(11), 2824-2831, 2007;
[32] Lee KB, Beaver MG, Caram HS, Sircar S. Reversible Chemisorbents for Carbondioxide and their Potential Applaications. Ind. Eng. Chem. Res., 47, 8048-8062, 2008
[33] Beaver MG, Lee, KB, Caram HS, Sircar S. Rapid Thermal Swing Sorption Enhanced Reaction Concepts for Production of Fuel-Cell Grade H_2. Chapter in "Sorption Enhanced Reaction Concepts for Hydrogen Production: Materials and Processes", Published by Research Signpost, S. Sircar and K. B. Lee (Eds), Chapter 4: 119-136, 2010
[34] Siriwardane, R.V., J.A. Poston, Interaction of H_2S with zinc titanate in the presence of H_2 and CO, Applied Surface Science, 45:131-139, 1990
[35] Siriwardane, R.V., D.C. Cicero, S. Jain, R.P. Gupta, B.S. Turk, Durable zinc oxide containing sorbents for moving bed and fluid-bed applications, Proceedings – 15th Annual International Pittsburgh Coal Conference, pp.373-391, 1998
[36] Lee, K.B., Beaver, M.G., Caram, H.S., Sircar, S., "Novel Thermal-Swing Sorption-Enhanced Reaction Process Concept for Hydrogen Production by Low-Temperature Steam-Methane Reforming," *Ind. Eng. Chem. Res.*, 46, 5003, 2007
[37] Lee, K.B., Sircar, S., "Removal and Recovery of Compressed CO_2 from flue gas by a Novel Thermal Swing Chemisorption Process," *AIChE. J.*, 54, 2293-2302, 2008
[38] Beaver, M.G., Sircar, S., "Adsorption Technology for Direct Recovery of Compressed, Pure CO_2 from a Flue Gas without Pre-compression or Pre-drying," accepted for publication in *Adsorption*, DOI 10.1007/s10450-010-9219-0

[39] Wachs, I.E., "Recent conceptual advances in the catalysis science of mixed metal oxide catalytic materials" *Catalysis Today,* 100, 79-94, 2005
[40] Wachs, I.E., "Infrared spectroscopy of supported metal oxide catalysts," *Colloids and Surfaces,* 105, 143-149, 1995
[41] Wachs, I.E., "Raman and IR studies of surface metal oxide species on oxide supports: Supported metal oxide catalysts," *Catalysis Today,* 27, 437-455, 1996

[42] Lee, E. L., Wachs, I.E., "In Situ Spectroscopic Investigation of the Molecular and Electronic Structures of SiO_2 Supported Surface Metal Oxides," *J. Phys. Chem. C,* 111, 14410-14425, 2007
[43] Vuurman, M.A., Wachs, I.E., "In Situ Raman Spectroscopy of Alumina-Supported Metal Oxide Catalysts," *J. Phys. Chem.,* 96, 5008-5016, 1992

[44] Gao, X., Jehng, J.M., Wachs, I.E., "*In Situ* UV-vis-NIR Diffuse Reflectance and Raman Spectroscopic Studies of Propane Oxidation over ZrO_2-Supported Vanadium Oxide Catalysts," *Journal of Catalysis,* 209, 43-50, 2002

[45] Ross-Medgaarden, E.I., Wachs, I.E., "Structural Determination of Bulk and Surface Tungsten Oxides with UV-vis Diffuse Reflectance Spectroscopy and Raman Spectroscopy," *J. Phys. Chem.,* 111, 15089-15099, 2007
[46] Pfeifer, H., "Characterization of Bronsted and Lewis Acidity by Nuclear Magnetic Resonance Spectroscopy" Acidity and Basicity of Solids: Theory, Assessment, and Utility, Eds. Jacques Fraissard and Leonidas Petrakis, Dordrecht. Kluwer Academic Publishers 255-277, 1993
[47] Wachs, I.E., Jehng, J.M., Ueda, W., "Determination of the Chemical Nature of Active Surface Sites Present on Bulk Mixed Metal Oxide Catalysts," *J. Phys. Chem. B,* 109, 2275-2284, 2005
[48] Di Cosimo, J.I., Diez, V.K., Xu, M., Iglesia, E., Apeseguia, C.R. "Structure and Surface and Catalytic Properties of Mg-Al Basic Oxides *Journal of Catalysis,* 178, 499-510, 1998
[49] Crepeau, G., Montouillout, V., Vimon, A., Mariey, L., Cseri, T., Mauge, F., "Nature, Structure and Strength of the Acidic Sites of Amorphous Silica Alumina: An IR and NMR Study," *J. Phys. Chem. B.,* 110, 15172, 2006
[50] Redhead, P.A., "Thermal Desorption of Gases," *Vacuum,* 203-211, 1962
[51] Liu, X., Truitt, R.E., "DRFT-IR Studies of the Surface of Γ-Alumina," *J. Am. Chem. Soc.,* 119, 9856-9860, 1997
[52] Walspurger, S., Boels, L., Cobden, P.D., Elzinga, G.D., Haije, W.G., van den Drink, R.,W., "The Crucial Role of the K^+-Aluminum Oxide Interaction in K^+-Promoted Alumina- and Hydrotalcite-Based Materials for CO_2 Sorption at High Temperatures," *ChemSusChem,* 1, 643-650, 2008
[53] Valente, J.S., Figueras, F., Gravelle, M, Kumbhar, P., Lopez, J., Besse, J.P., "Basic Properties of the Mixed Oxides Obtained by Thermal Decomposition of Hydrotalcites Containing Different Metallic Compositions," *Journal of Catalysis,* 189, 370-381, 2000
[54] Hutson, N.D., "Structural Effects on the High Temperature Adsorption of CO_2 on a Synthetic Hydrotalcite," *Chem. Mater.,* 16, 4135-4143, 2004
[55] Braterman, P.S., Xu, Z.P., Yarberry, F., "Layered Double Hydroxides (LDHs)," Handbook of Layered Materials, Eds. Auerbach, S.M., Carrado, K.A., Dutta, P. K.,New York. Marcel Dekker, Inc. 373-474, 2004

[56] Turek, A.M., Wachs, I.E., DeCanio, E., "Acidic Properties of Alumina-Supported Metal Oxide Catalysts: An Infrared Spectroscopic Study," *J. Phys. Chem.*, 96, 5000-5007, 1992

[57] Busca, G., Lorenzelli, V., "Infrared Spectroscopic Identification of Species Arising from Reactive Adsorption of Carbon Oxides on Metal Oxide Surfaces," *Materials Chemistry,* 7, 89-126, 1982

[58] Nakamoto, K., Fujita, J., Tanaka, S., Kobayashi, M., "Infrared Spectra of Metallic Complexes. IV. Comparison of the Infrared Spectra of Unidentate and Bidentate Metallic Complexes,"*J. Am. Chem. Soc.*, 79, 4904-4908, 1957

[59] Kloprogge, J.T., Frost, R.L., "Infrared Emission Spectroscopic Study of the Thermal Transformation of Mg-, Ni-, and Co-Hydrotalcite Catalysts," *Applied Catalysis A: General,* 184, 61-71, 1999

[60] Ogden, J. S., Williams, S. J., "Matrix Isolation Studies on $Cs_2[CO_3]$, $Rb_2[CO_3]$, and $K_2[CO_3]$: The Shape of Molecular K_2CO_3," *J. Chem. Soc: Dalton Transactions,* 2, 456-462, 1981

[61] Evans, J.V., Whateley, T.L., "Infrared Study of Adsorption of Carbon Dioxide and Water on Magnesium Oxide," *Trans Faraday Soc.,* 61, 2769, 1967

[62] Smart, R.S.C., Slager., T.L., Little, L.H., Greenler, R.G., "Carbon Monoxide Adsorption on Magnesium Oxide," *J. Phys. Chem.*, 77, 1019-1023, 1973

TABLES

Table 1: New Sorption model parameters

K_c^o	K_r^o	m (mol/kg)	qc (J/mol)	Hr (J/mol)	a^o	E_a (J/mol)
0.00029	0.000540439	0.34	-64900	-37500	0.80183	4390

T (°C)	K_H (mol/kg/atm)	K_c (atm^{-a})	K_r (atm^{-a})	a
150	10124.02146	29776.5337	23.014569	2.8
250	297.795825	875.8700734	3.00000249	2.2
350	27.16427124	79.89491542	0.75204361	1.9
450	4.804918693	14.1321138	0.2764064	1.7

Table 2. Boundary conditions for modeling

	Pressure	Inlet Temp.	Species	Case I	Case II	Case III	Case IV
Gas side	40 bar	550 ^oC	CO_2 [kmol/s]	3.57	3.80	0.37	0.05
			H_2O (g) [kmol/s]	0.04	0.48	3.60	3.66
			Total [kmol/s]	3.61	4.28	3.97	3.71
			yCO_2 [vol%]	99.0	89.0	9.32	1.35
Coolant side	40 bar	200-240 ^oC	H_2O (l) [kmol/s]	1.34	2.93	9.0	7.57

Table 3: Cost Analysis for SE-WGS system for production of 30MM scfd H_2
All costs are per kg of H_2 product over 20 years of plant life

Item	**SE-WGS[a] (CO_2 Product at 40.5 bar) Recovery = 71.1 %**
Sorber-reactor vessels (16 units)	0.22
CO_2 Product Compressors (2 units)	0.03
Chemisorbent/Catalyst admixture (cost of $3.50/lb)	0.01
Heating Loop HX (2 units)	**0.02**
Total Capital Cost ($/kg H_2 produced)	**$0.28**
Electrical Cost of Power for Product CO_2 Compressor	0.21
Regeneration Steam Cost	0.53
% of Heat Recovered by HP condensation unit (~25%)	-0.13
Cost of External Heat for Thermal Swing[f] (0.34 MMBTU/kg H_2)	1.47
Total Operating Cost ($/kg H_2 produced)	**$2.08**

FIGURES

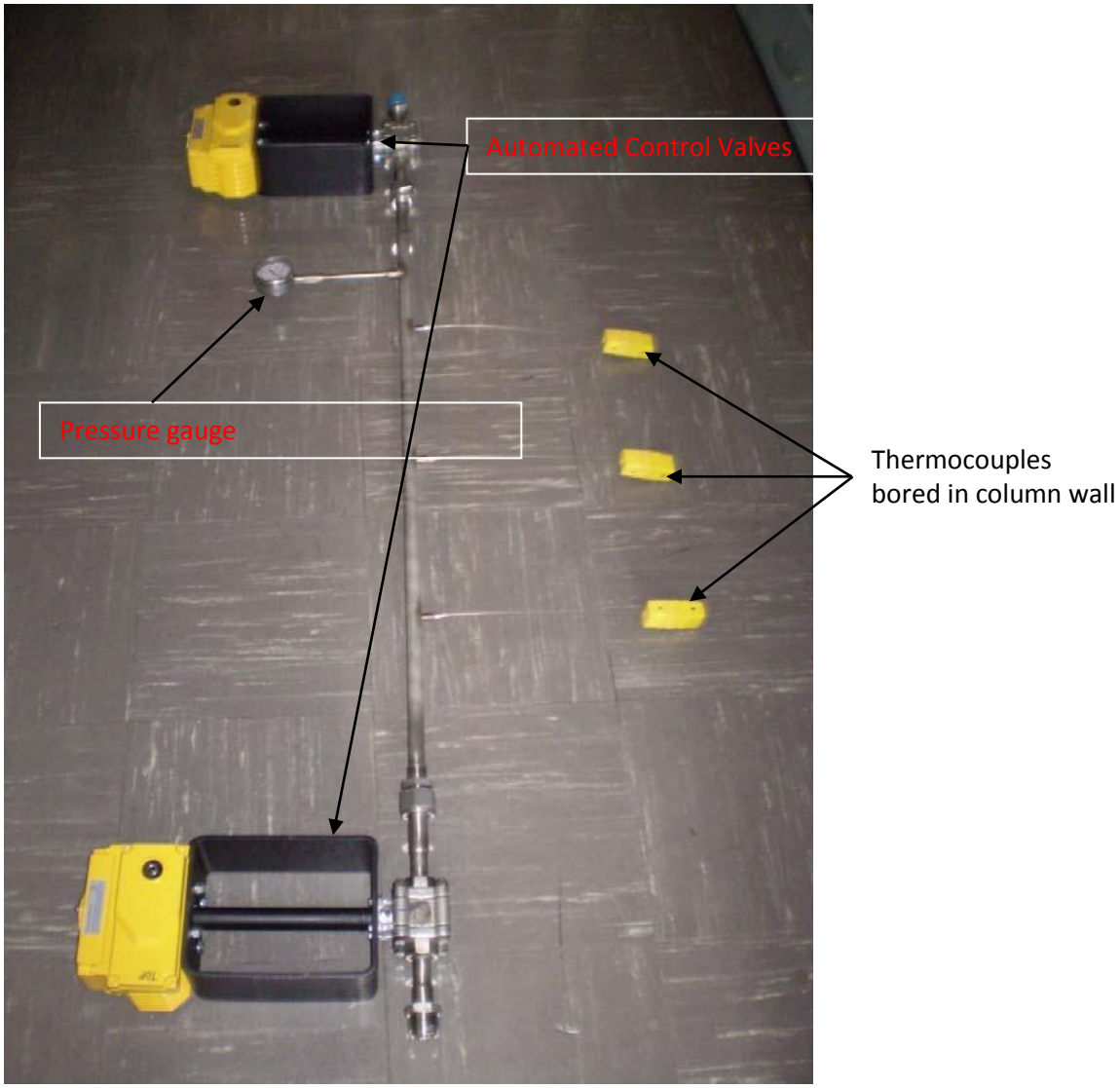

Figure 1: Newly constructed sorption column

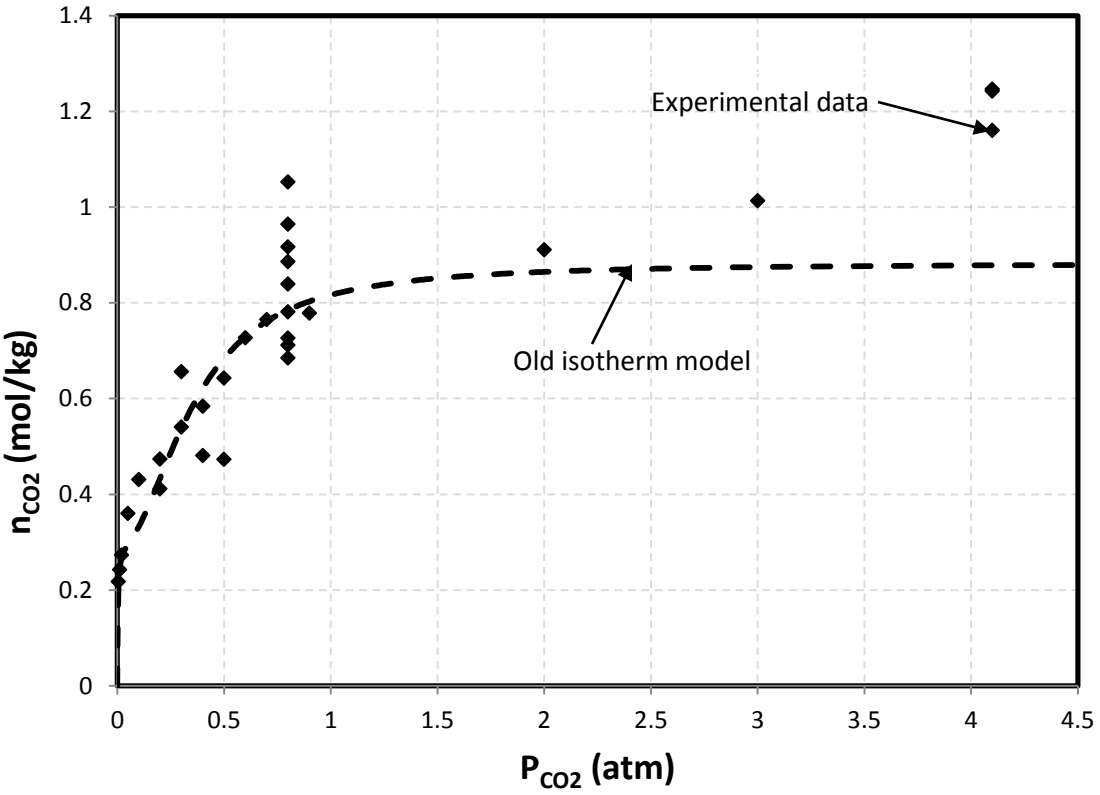

Figure 2: Updated isotherm plot at 250°C for Na_2O promoted alumina with new high pressure experimental data points

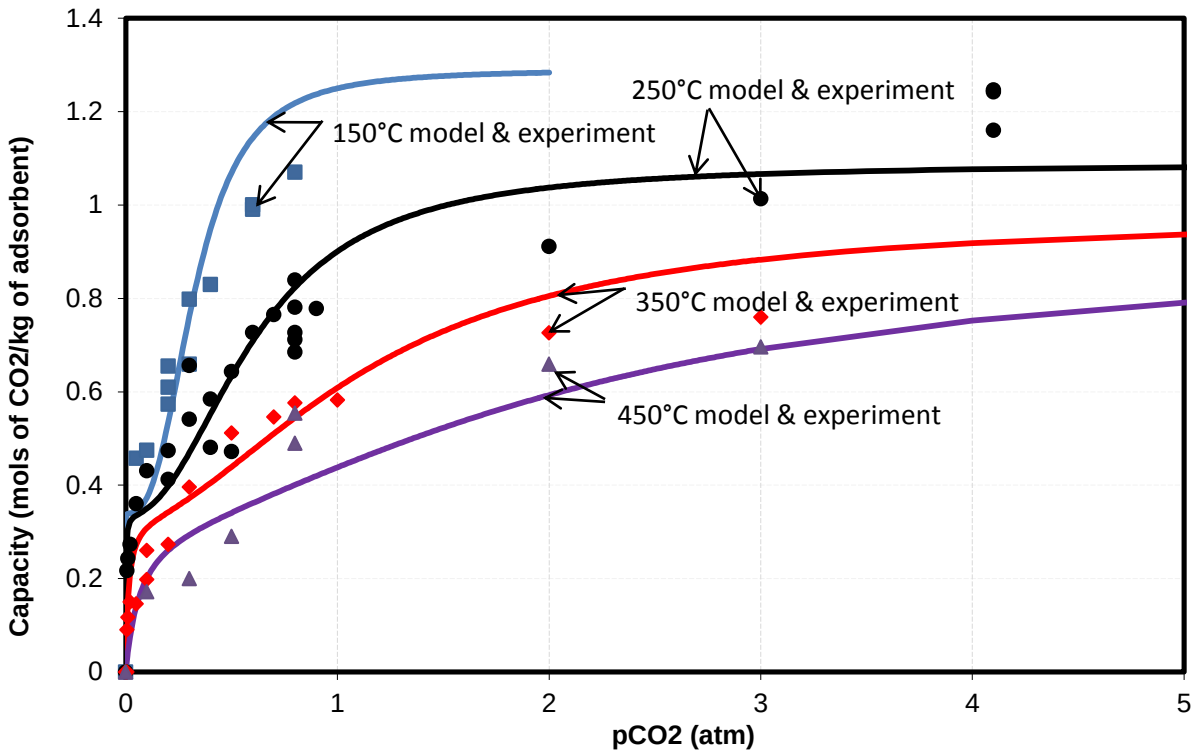

Figure 3: New fit of CO_2 sorption isotherm on Na_2O promoted alumina

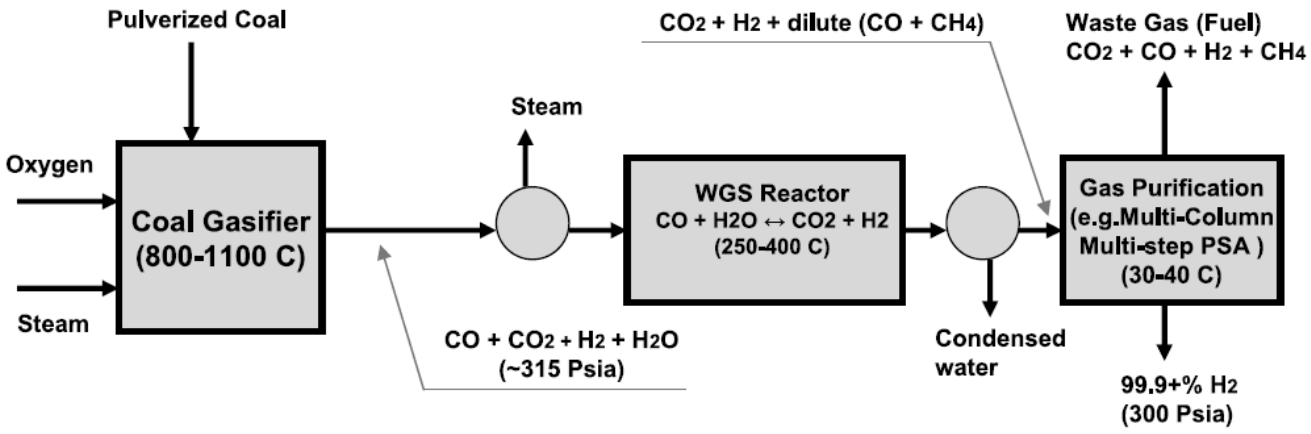

Figure 4. Schematic of conventional H_2 production system from coal gasification [1]

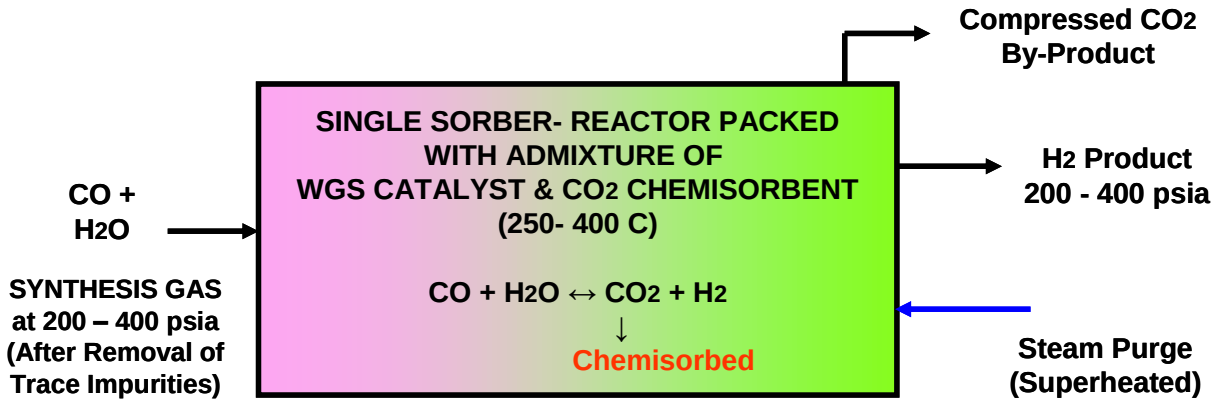

Figure 5. Schematic of TSSER for simultaneous H_2 and CO_2 production system [2]

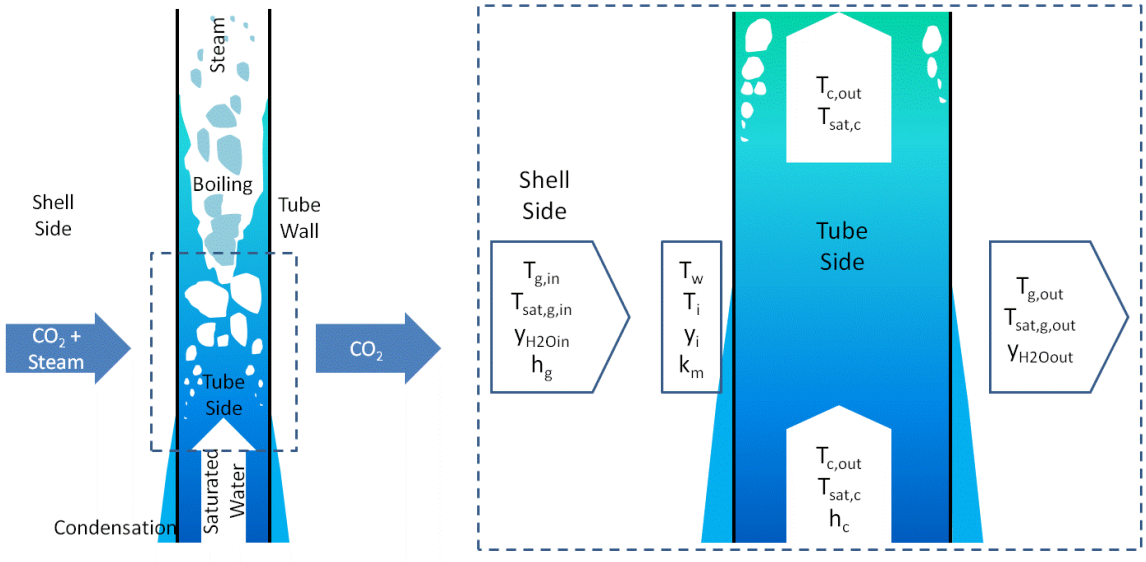

(a) (b)

Figure 6. Schematic of (a) control volume in heat exchanger and (b) main variables

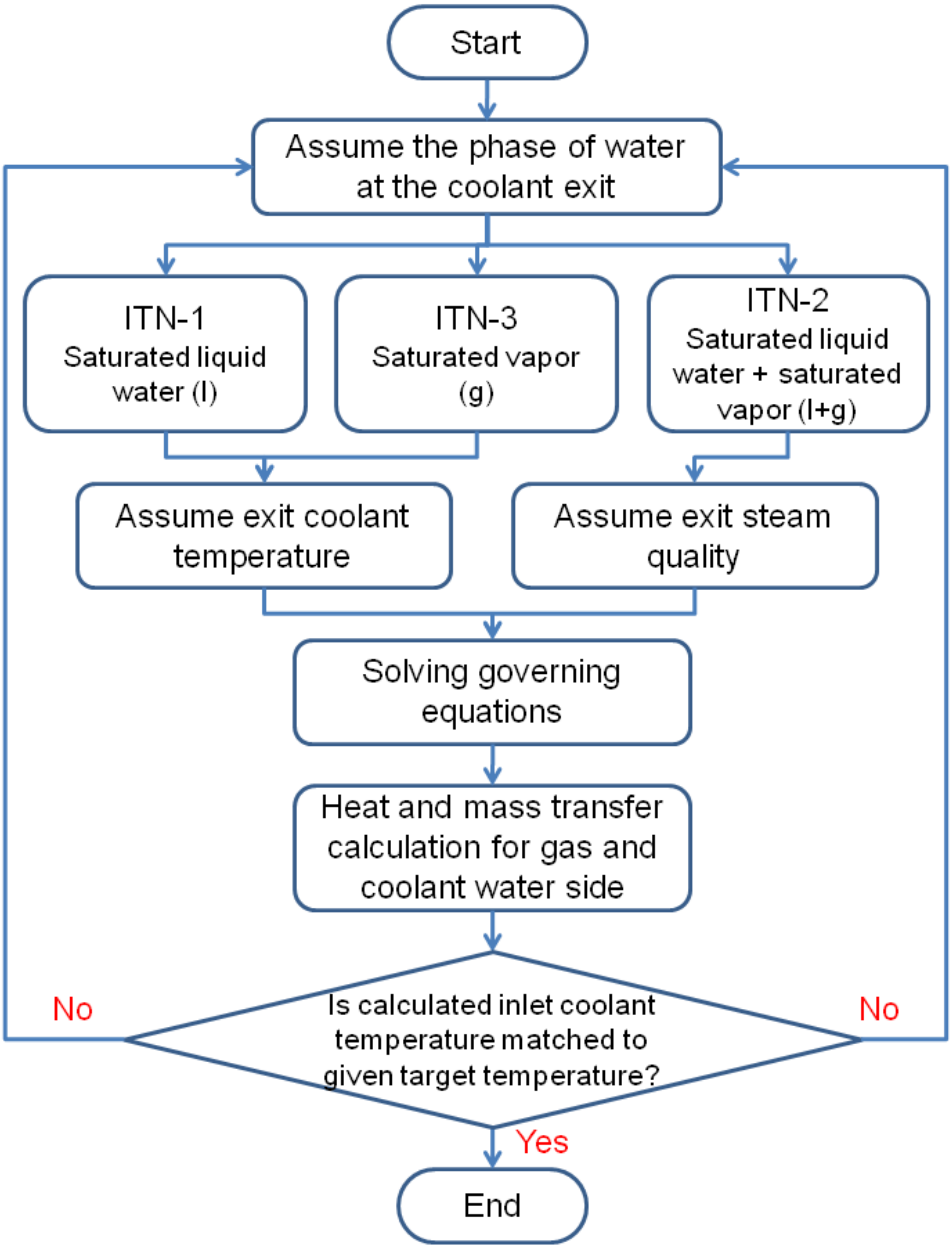

Figure 7. Schematic of numerical scheme for modeling

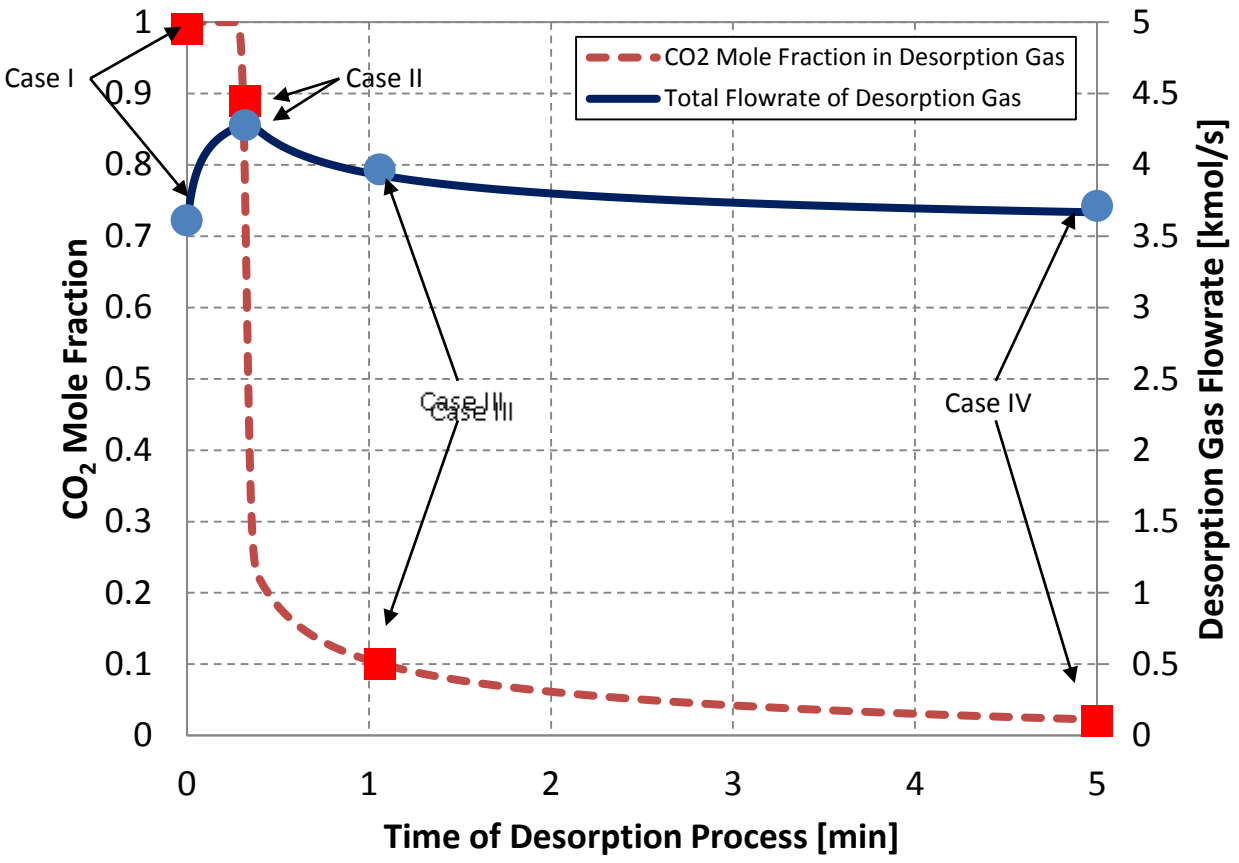

Figure 8. Variations of CO_2 mole fractions and total flow rates during the desorption cycle

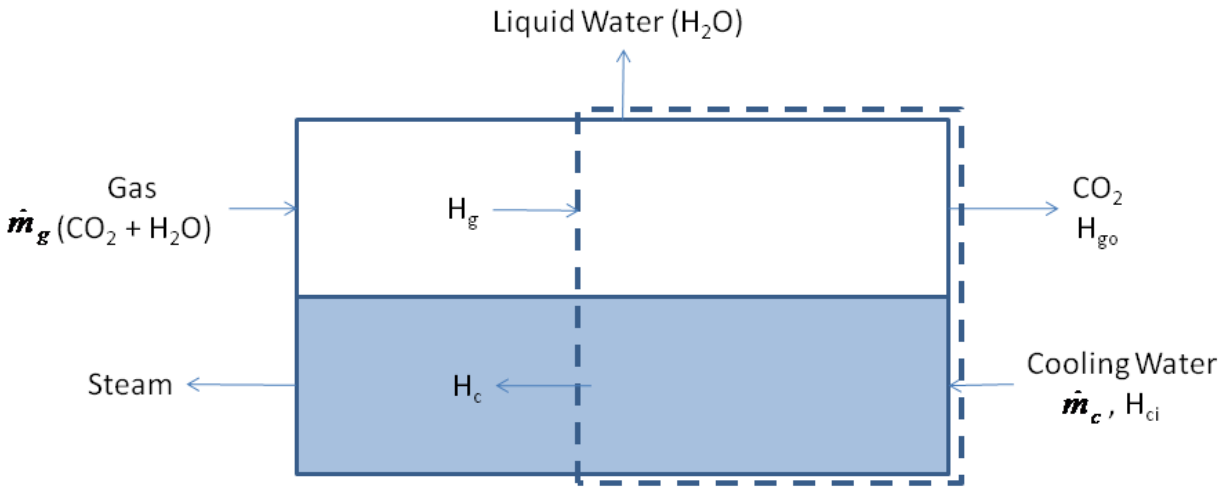

Figure 9. Control volume for bounded constraint diagram

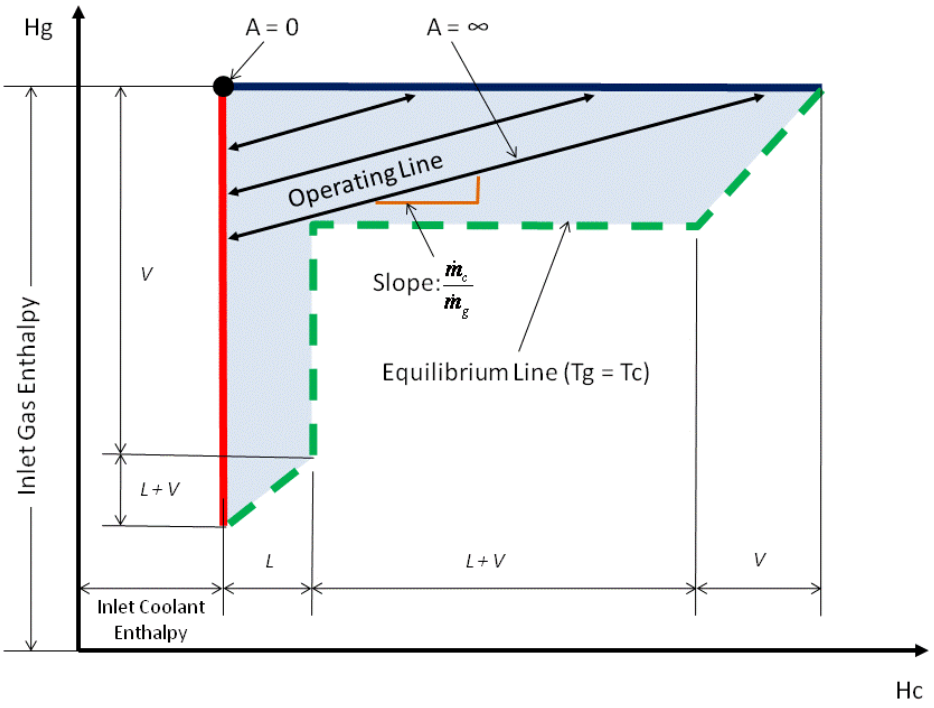

Figure 10. Schematic of bounded constraint diagram

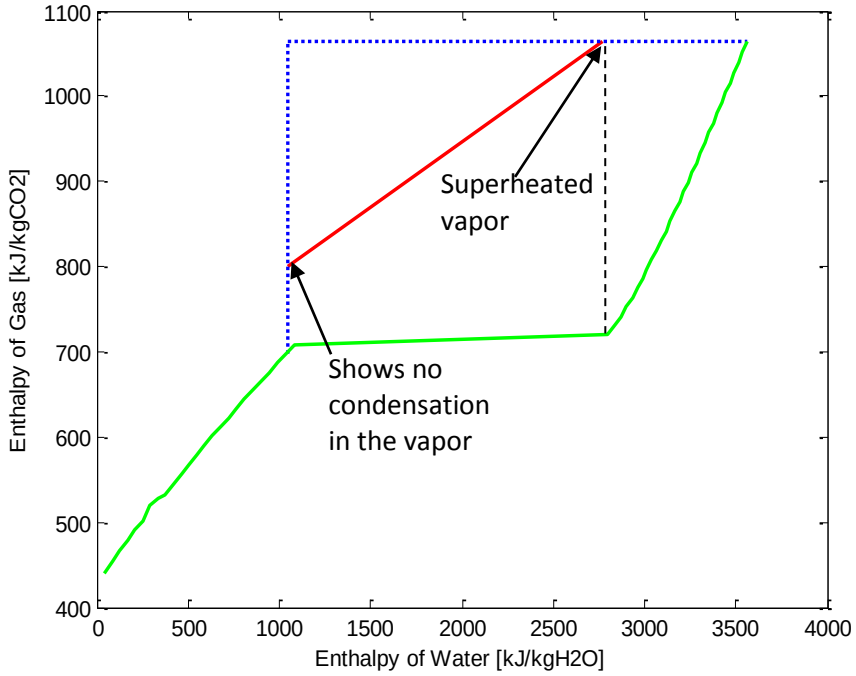

(a) Case I

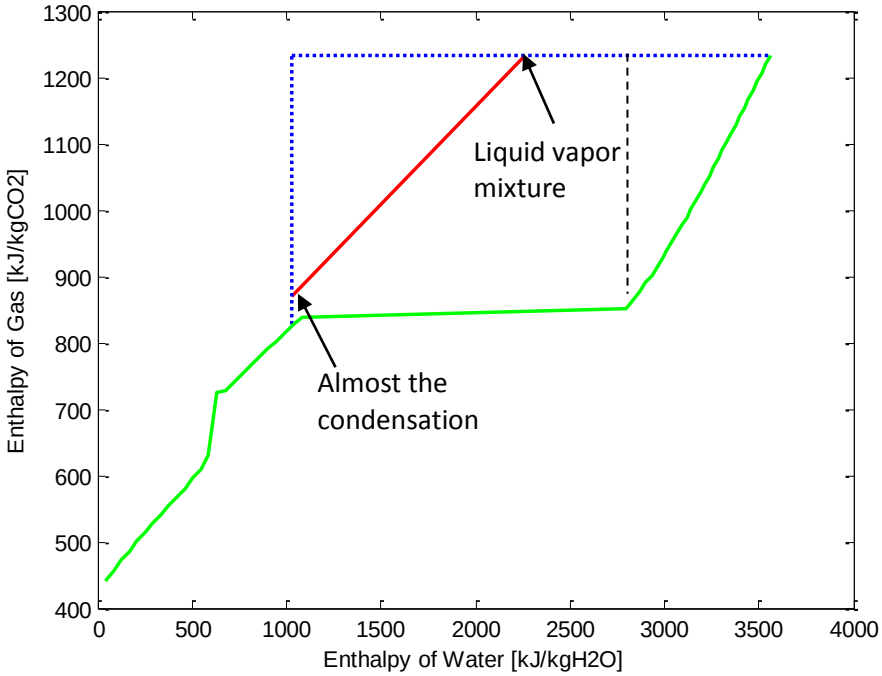

(b) Case II

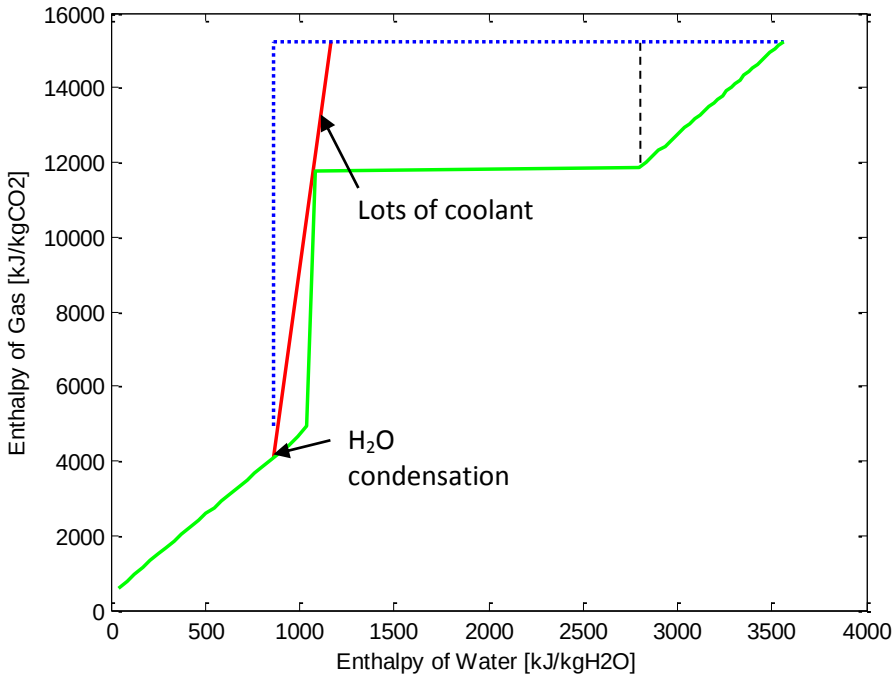

(c) Case III

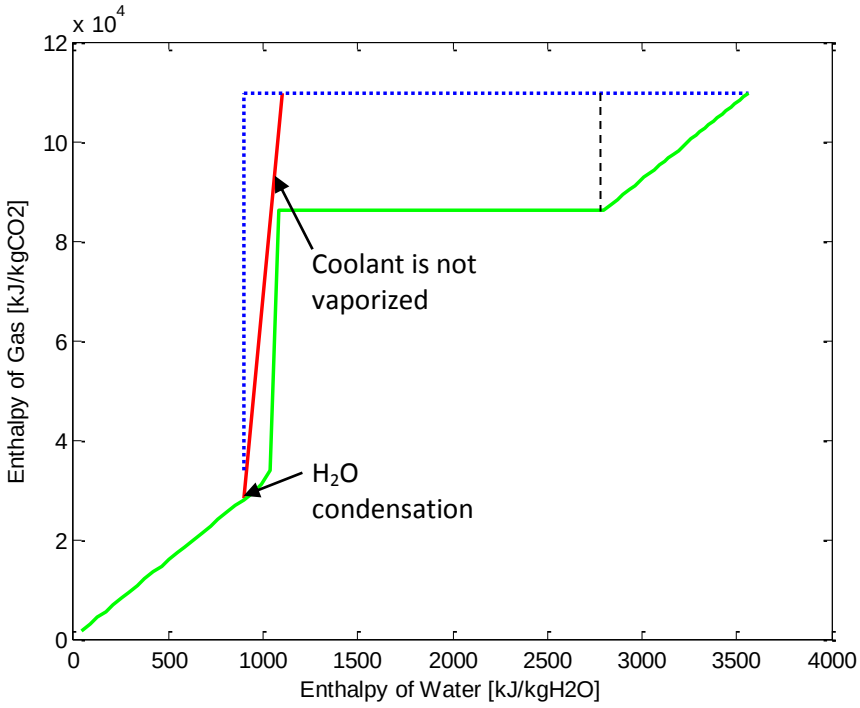

(d) Case IV

Figure 11. Verifications of modeling results using bounded constraint diagram

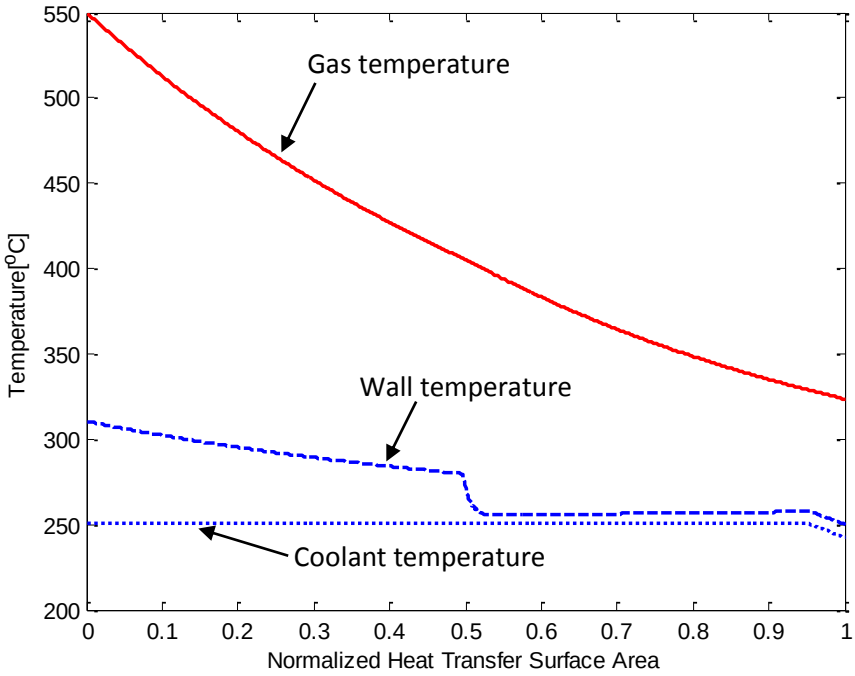

(a) Case I

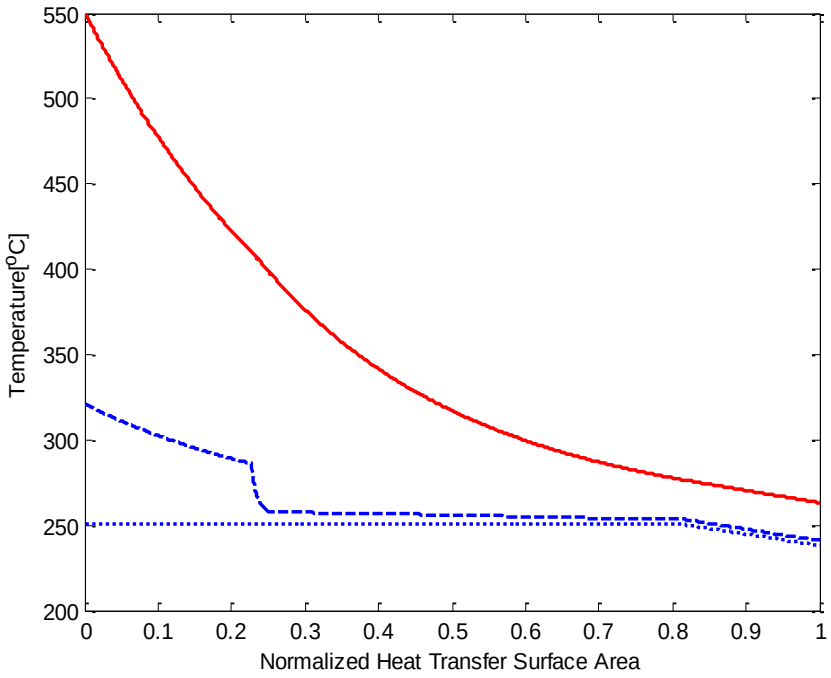

(b) Case II

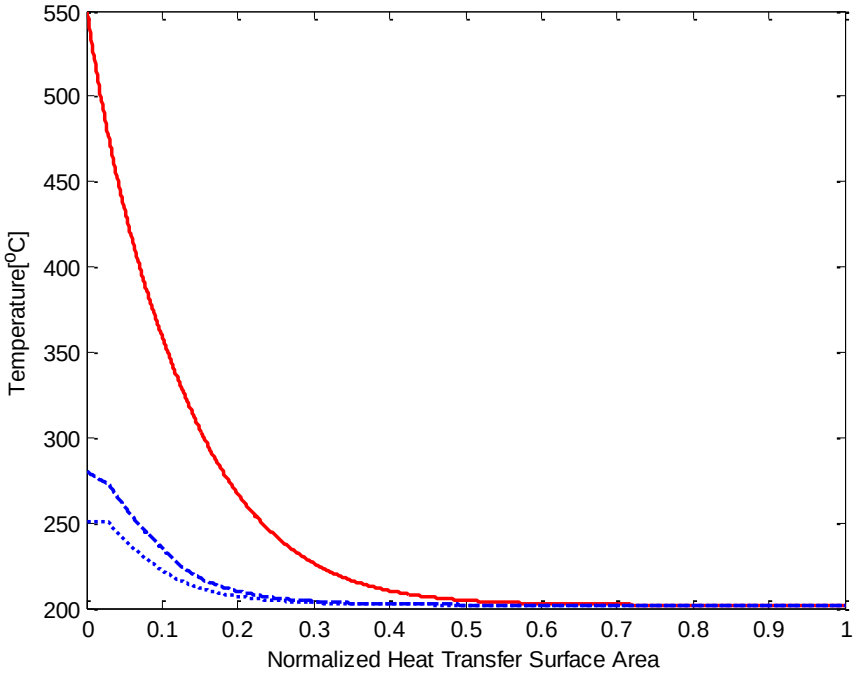

(c) Case III

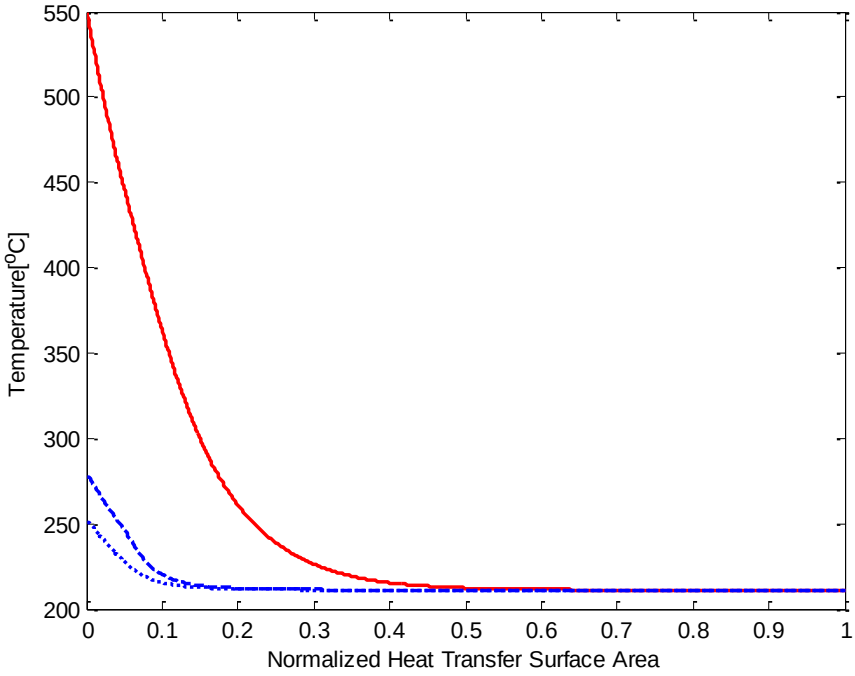

(d) Case IV

Figure 12. Temperature profiles as results of modeling

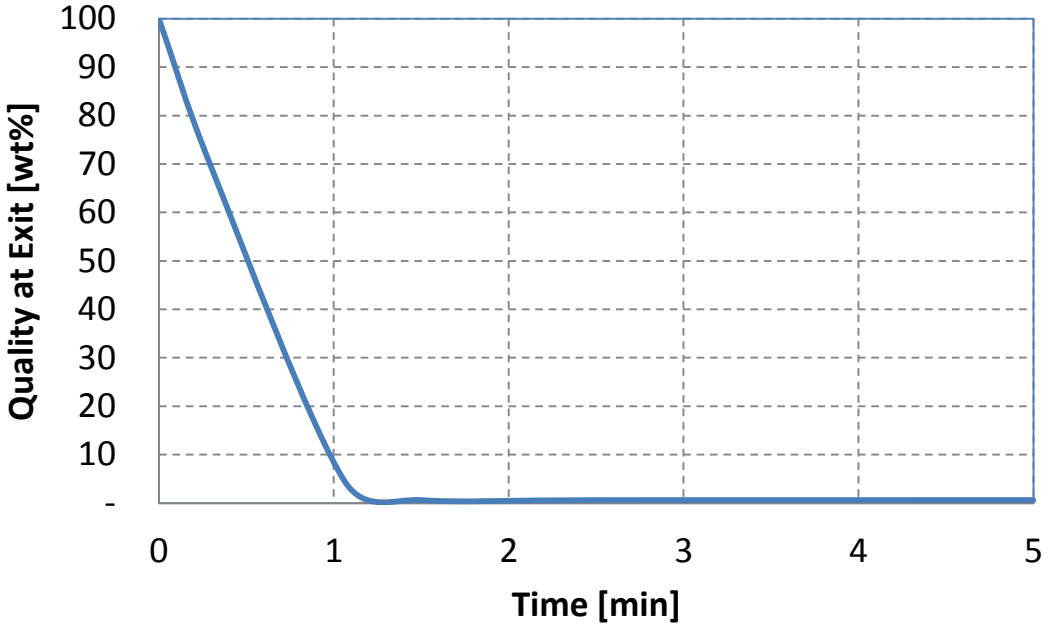

Figure 13. Steam quality at the coolant exit during the desorption cycle

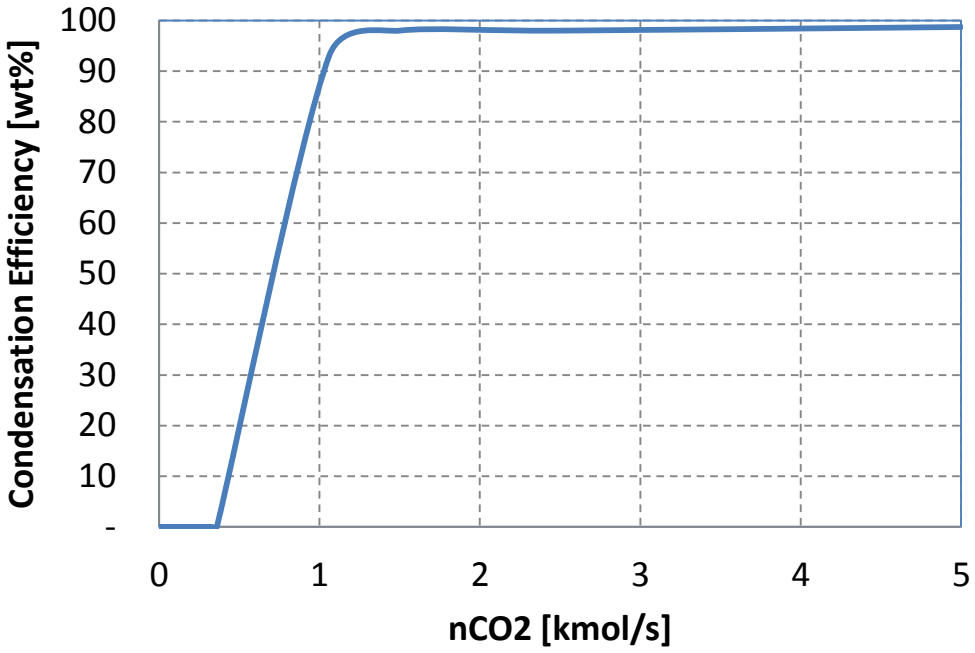

Figure 14. Condensation efficiency during the desorption cycle

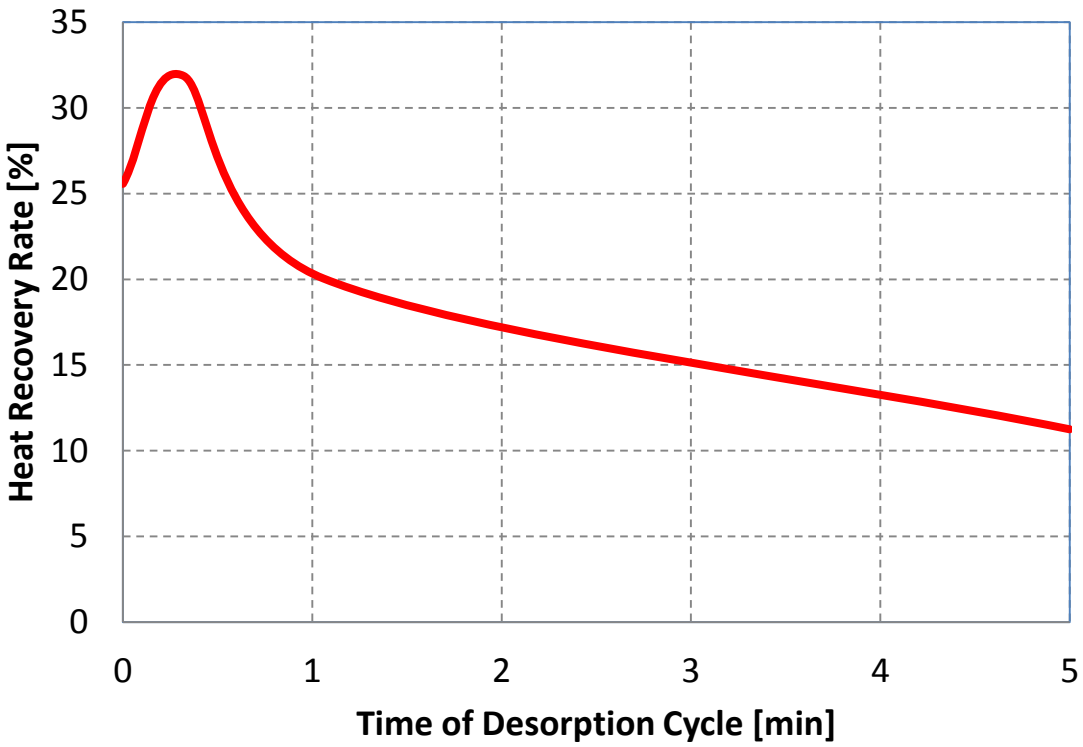

Figure 15. Heat recovery rate during the desorption cycle

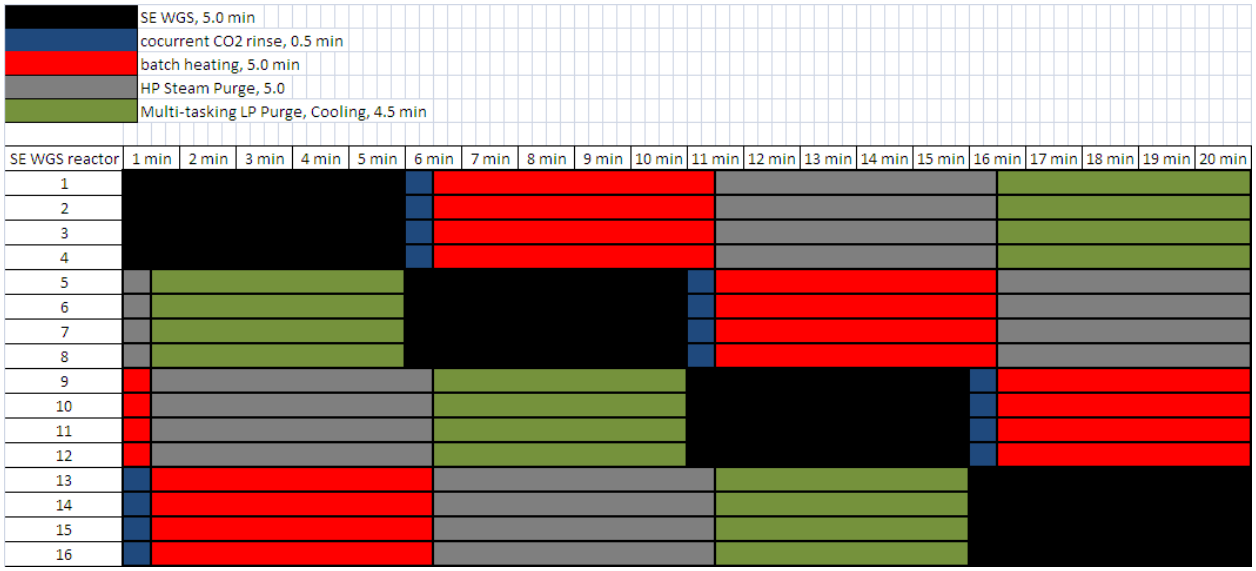

Figure 16: Cycle Scheduling of 16-bed TSSER process for production of 30 MMSCFD H_2

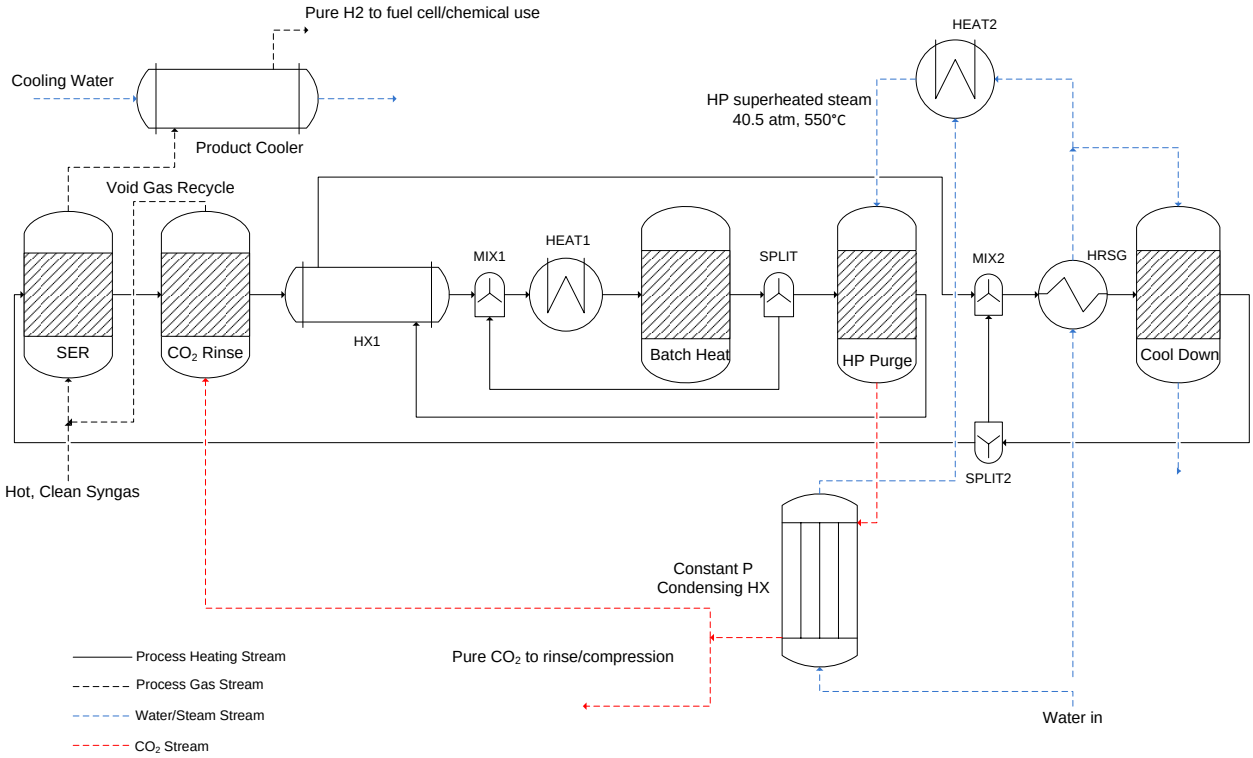

Figure 17: Heat Integrated Schematic of TSSER Process

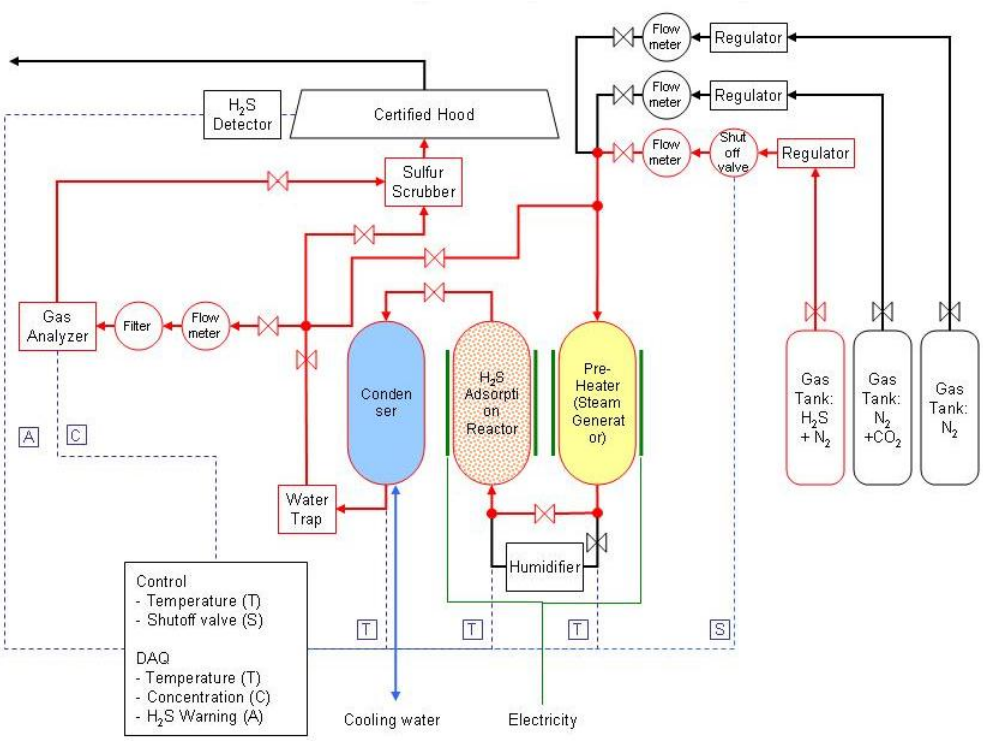

Figure 18. Schematic drawing of the experimental apparatus

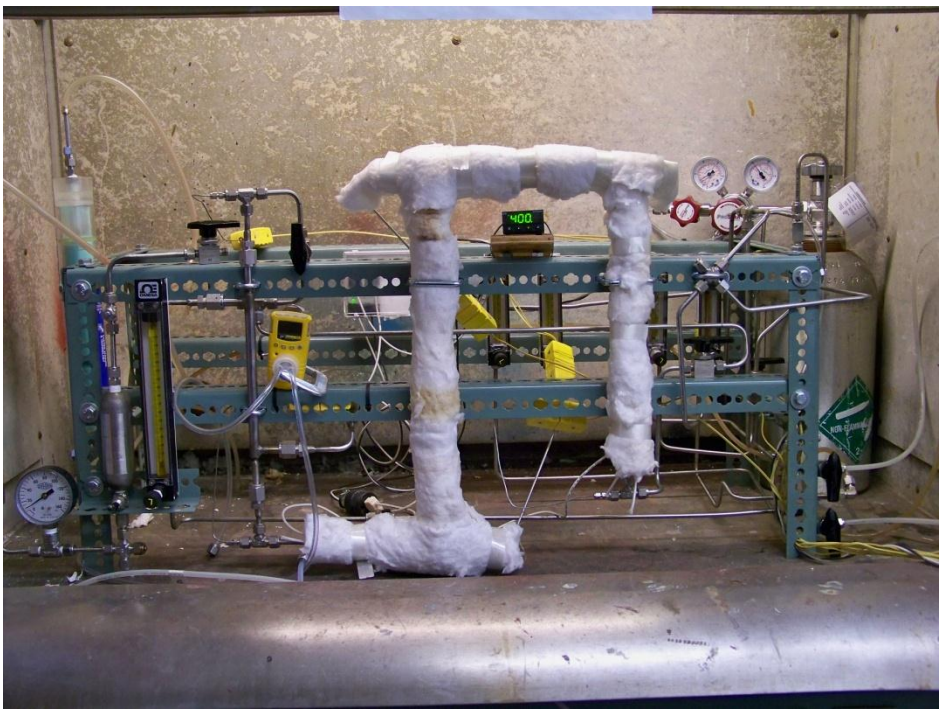

Figure 19. Photograph of the apparatus

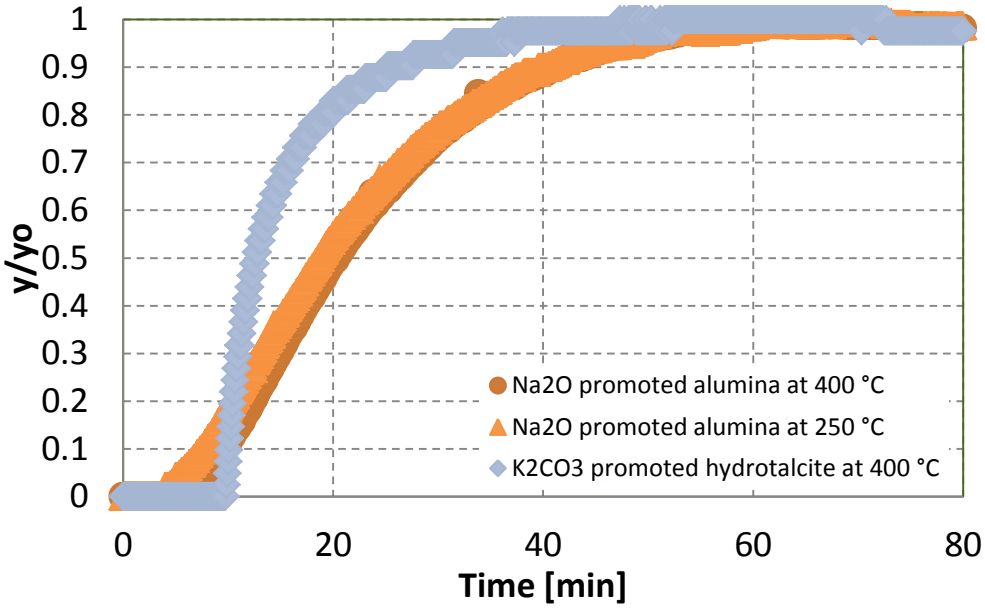

Figure 20. Adsorber effluent gas composition profiles for trace (1,000 ppm in N_2) SO_2 sorption on chemisorbents

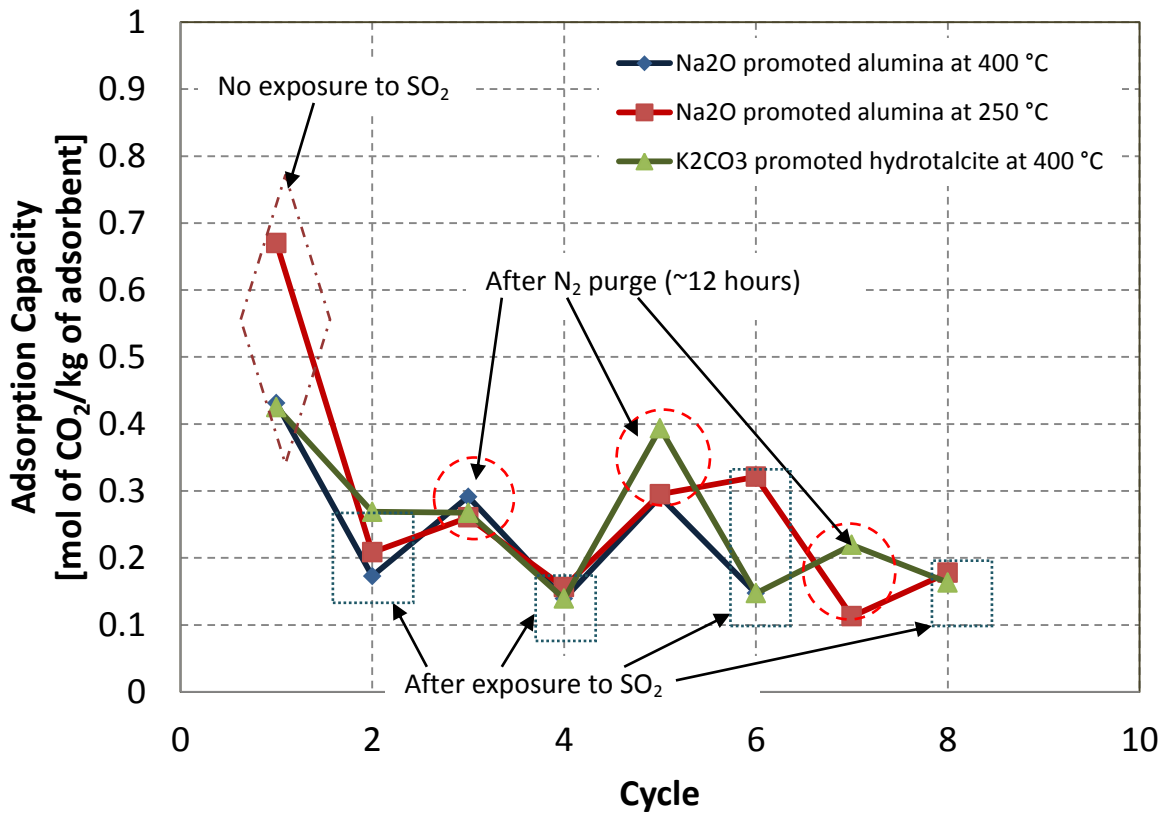

Figure 21. Cyclic behavior of CO_2 adsorption capacity before and after exposure to trace SO_2 on the chemisorbents.

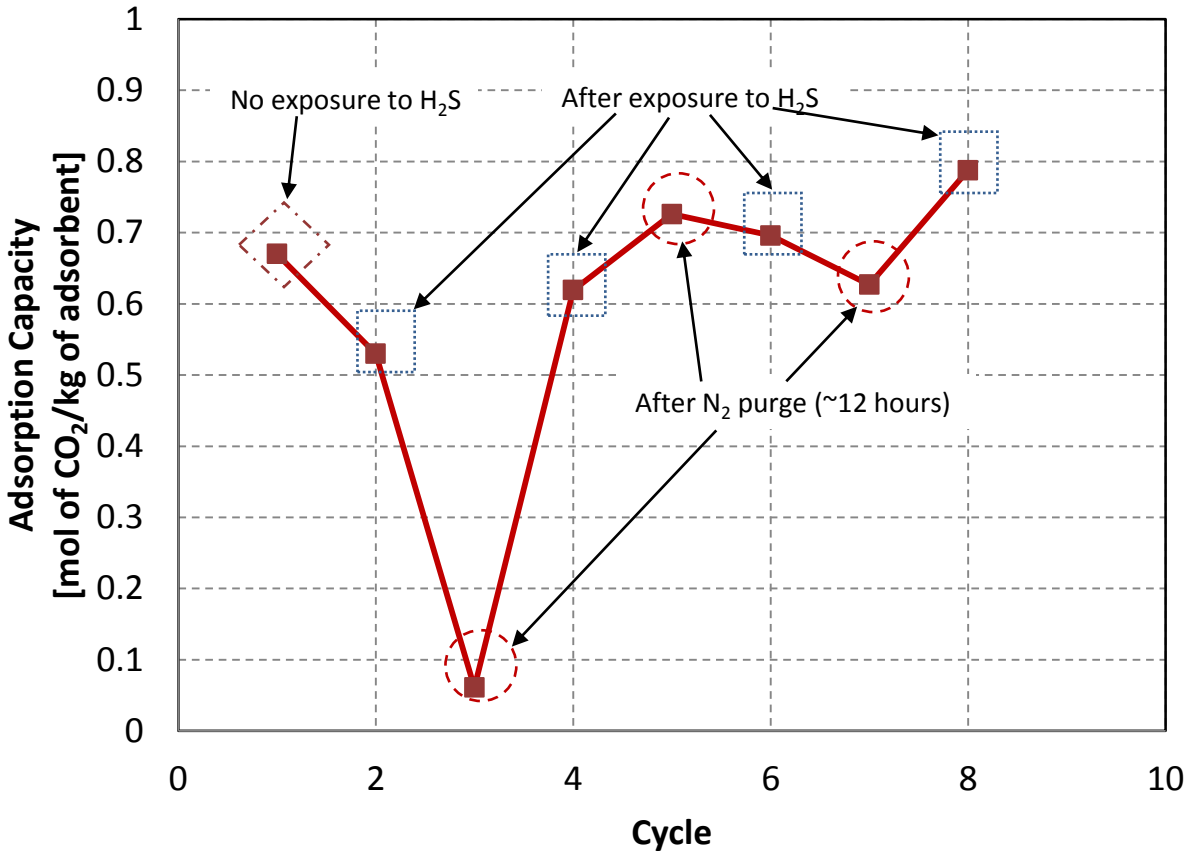

Figure 22. Cyclic behavior of CO_2 adsorption capacity before and after exposure to trace H_2S on promoted alumina at 250 ^oC.

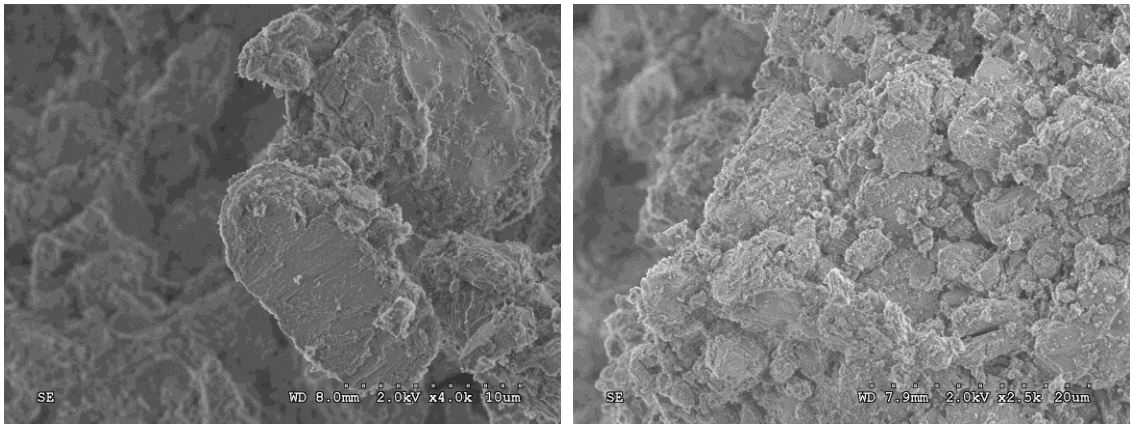

(a) Clean (b) Cycled with SO_2

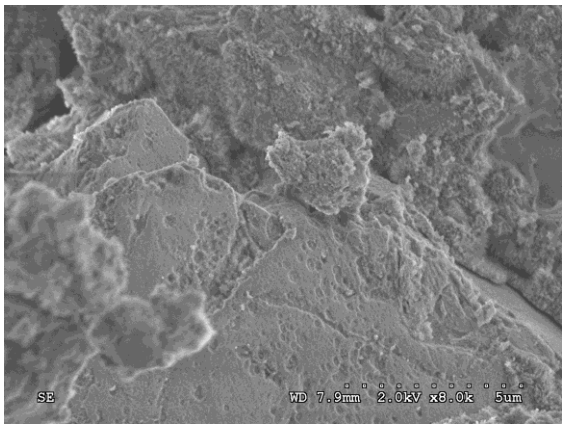

(c) Cycled with H_2S

Figure 23. SEM images of Na_2O promoted alumina for clean and cycled with sulfur compounds

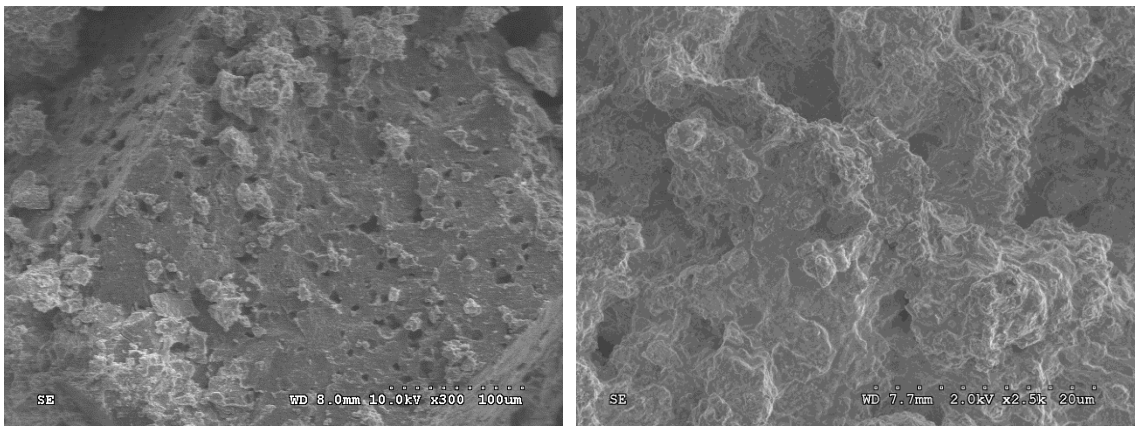

(a) Clean (b) Cycled with H_2S

Figure 24. SEM images of K_2CO_3 promoted hydrotalcite for clean and cycled with sulfur compounds

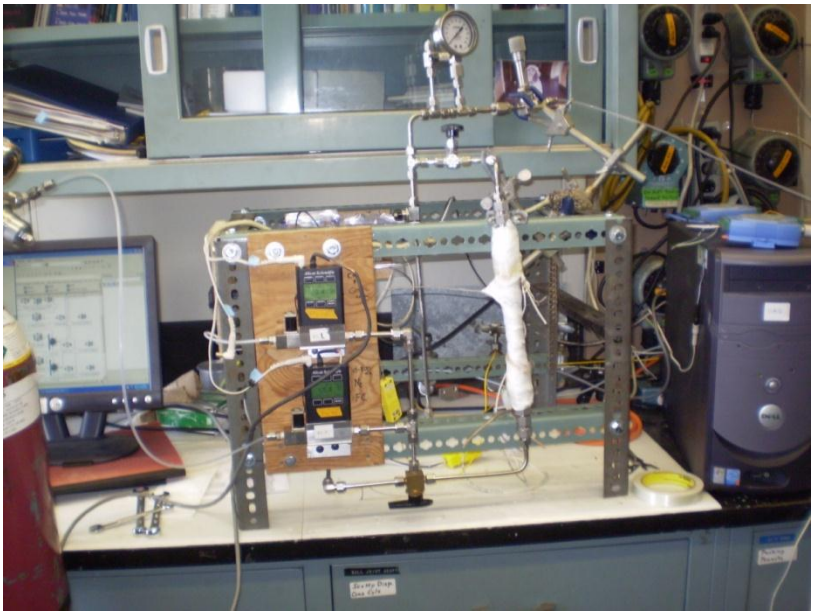

Figure 25: Front Picture of TPD unit

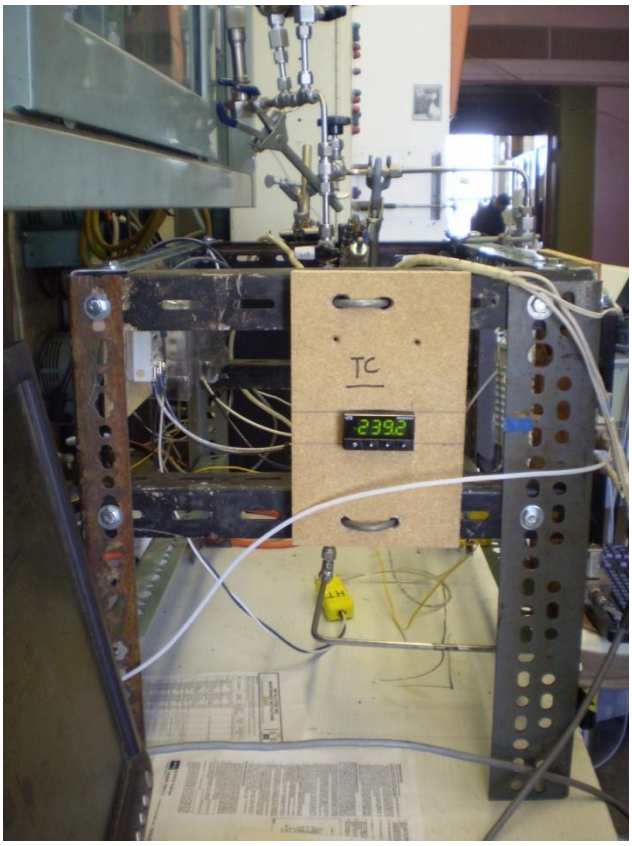

Figure 26: Side View of Temperature Controller on TPD unit

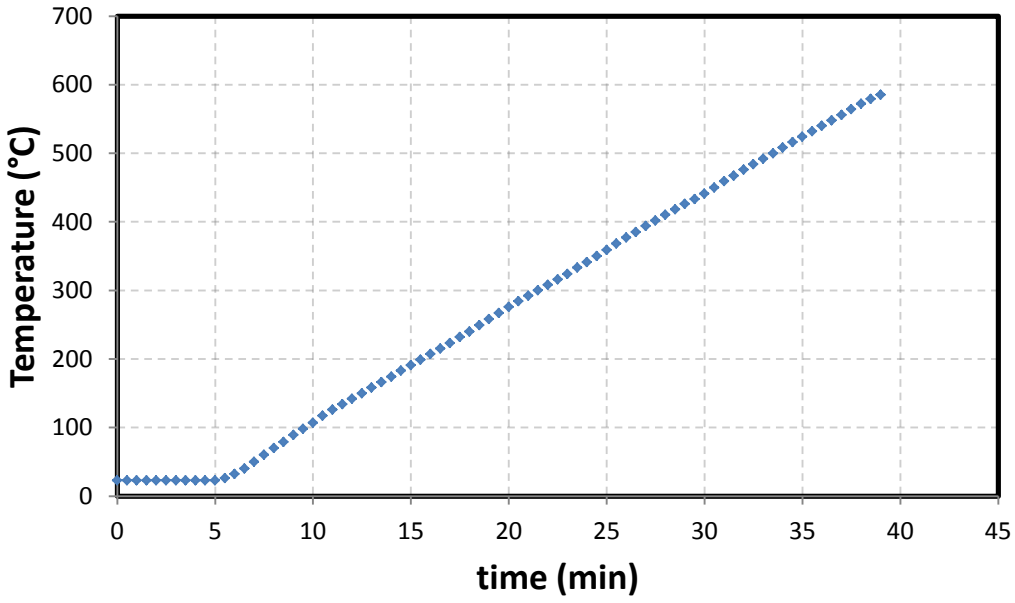

Figure 27: Temperature Ramp during typical TPD/TPSR experiment

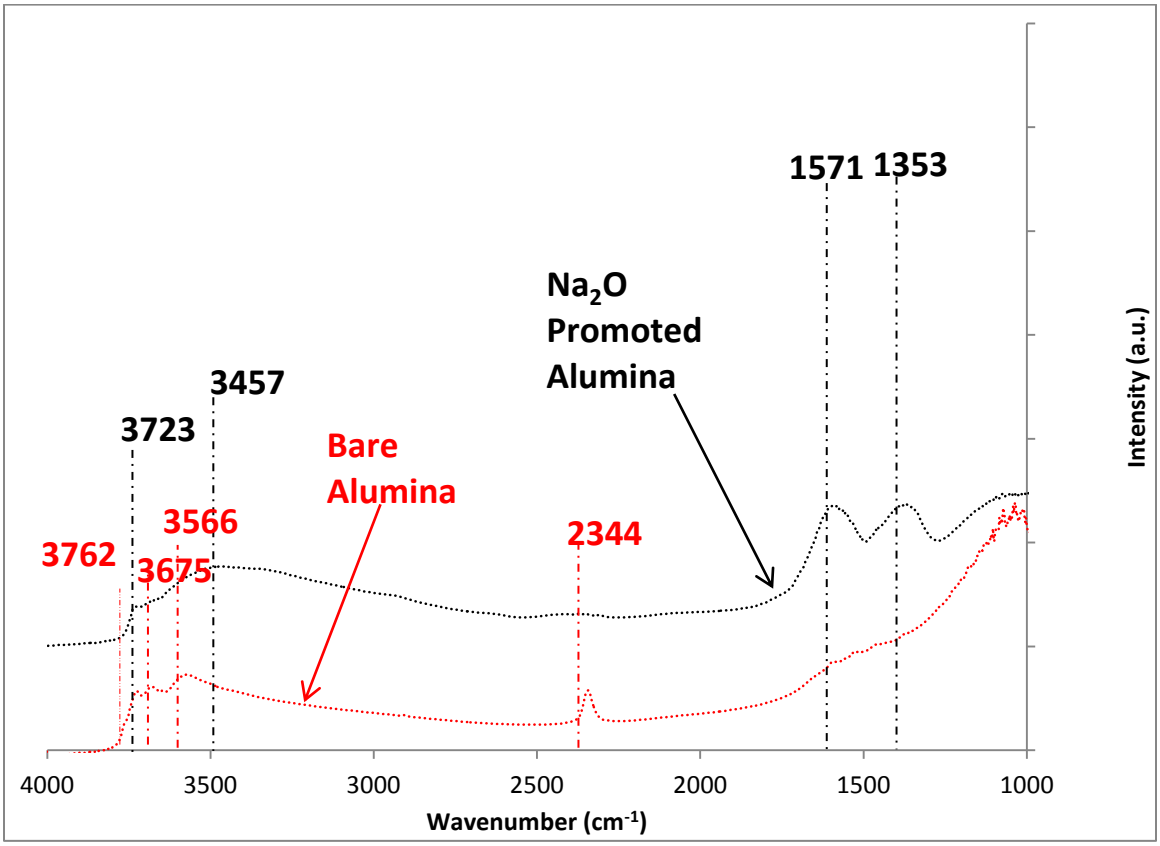

Figure 28: Dehydrated DRIFTS of Na_2O promoted alumina and bare γ-alumina

TABLE I: Assignment of IR Bands (cm^{-1}) Observed upon Chemisorption of CO_2 on Pure Metal Oxides[15]

species	wavenumber	structure
free carbonate	1415–1470 (ν_{as})	
monodentate	1420–1540 (ν_{as}) 1330–1390 (ν_s) 980–1050 (γ_{CO})	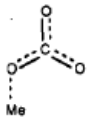
bidentate	1600–1670 (ν_s) 1280–1310 (ν_{as}) 980–1050 (γ_{COO^-}) 830	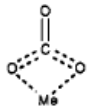
bridged	1780–1840 (ν_s) 1250–1280 (ν_{as}) 1000 (γ_{COO^-})	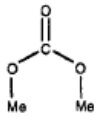
bicarbonate	3600 (γ_{OH}) 1615–1630 (ν_{as}) 1400–1500 (ν_s) 1225 (γ_{OH})	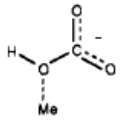
carboxylate	1570–1630 (ν_{as}) 1350–1390 (ν_s)	
formate	2740–2850 (ν_{CH}) 1580–1620 (ν_{as}) 1340–1390 (ν_s)	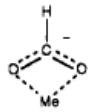

Figure 29: Suface structures and corresponding wavenumbers

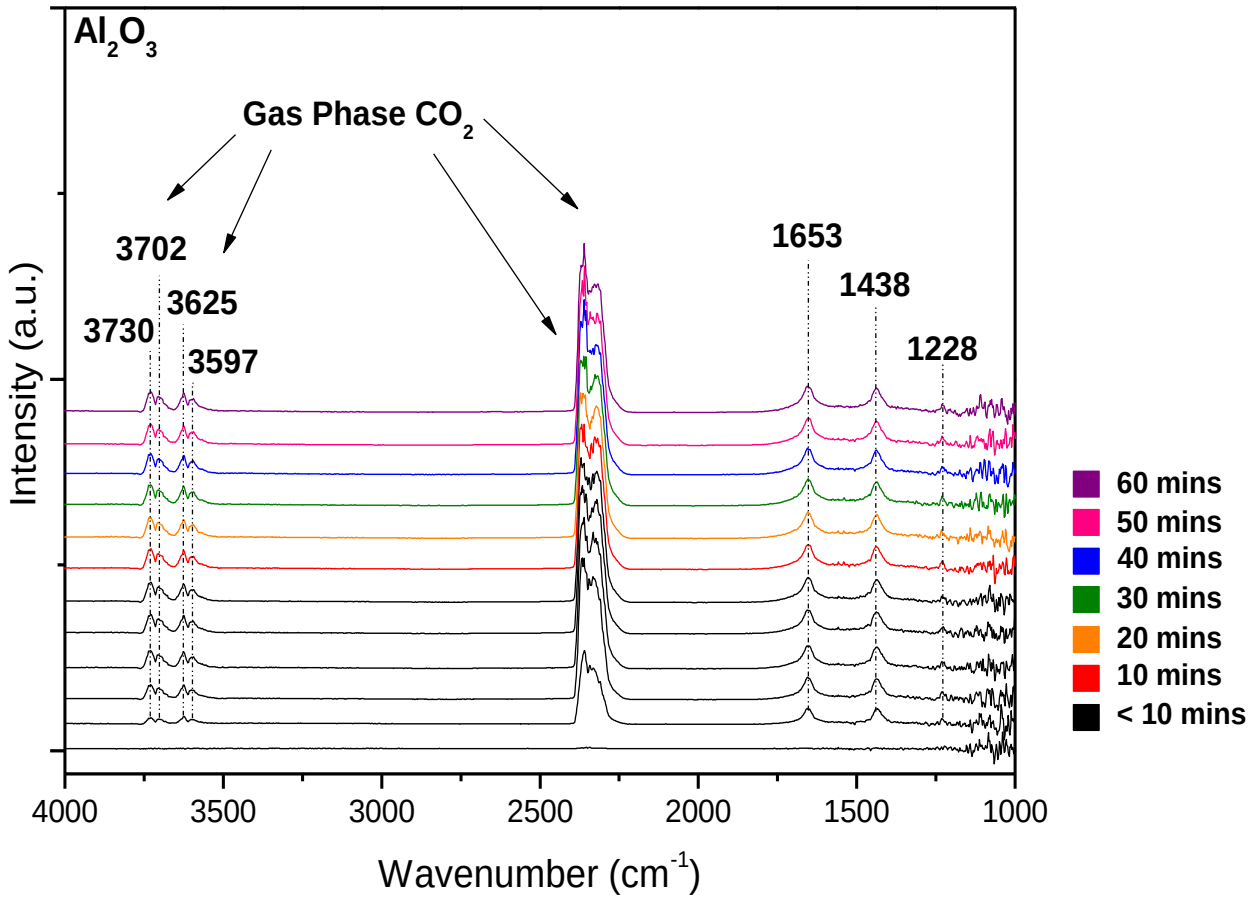

Figure 30: DRIFTS of γ-alumina during CO_2 adsorption at 200°C

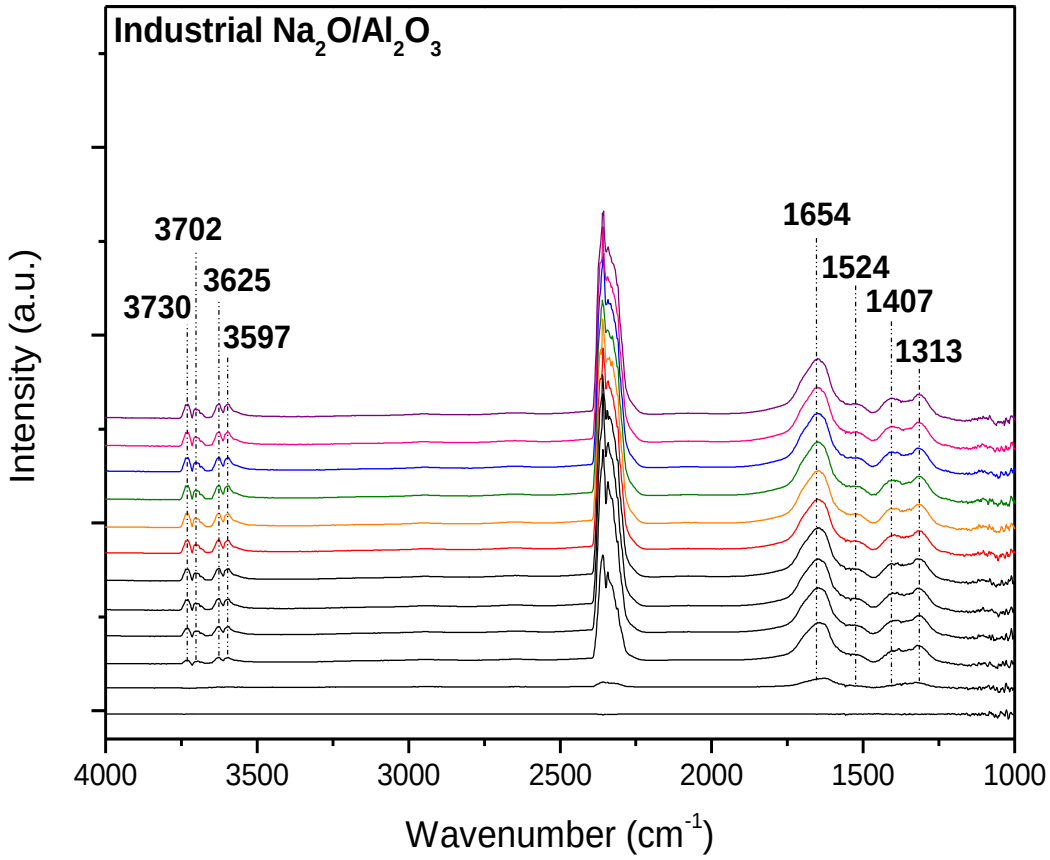

Figure 31: DRIFTS of Industrial Na_2O promoted Alumina during CO_2 exposure

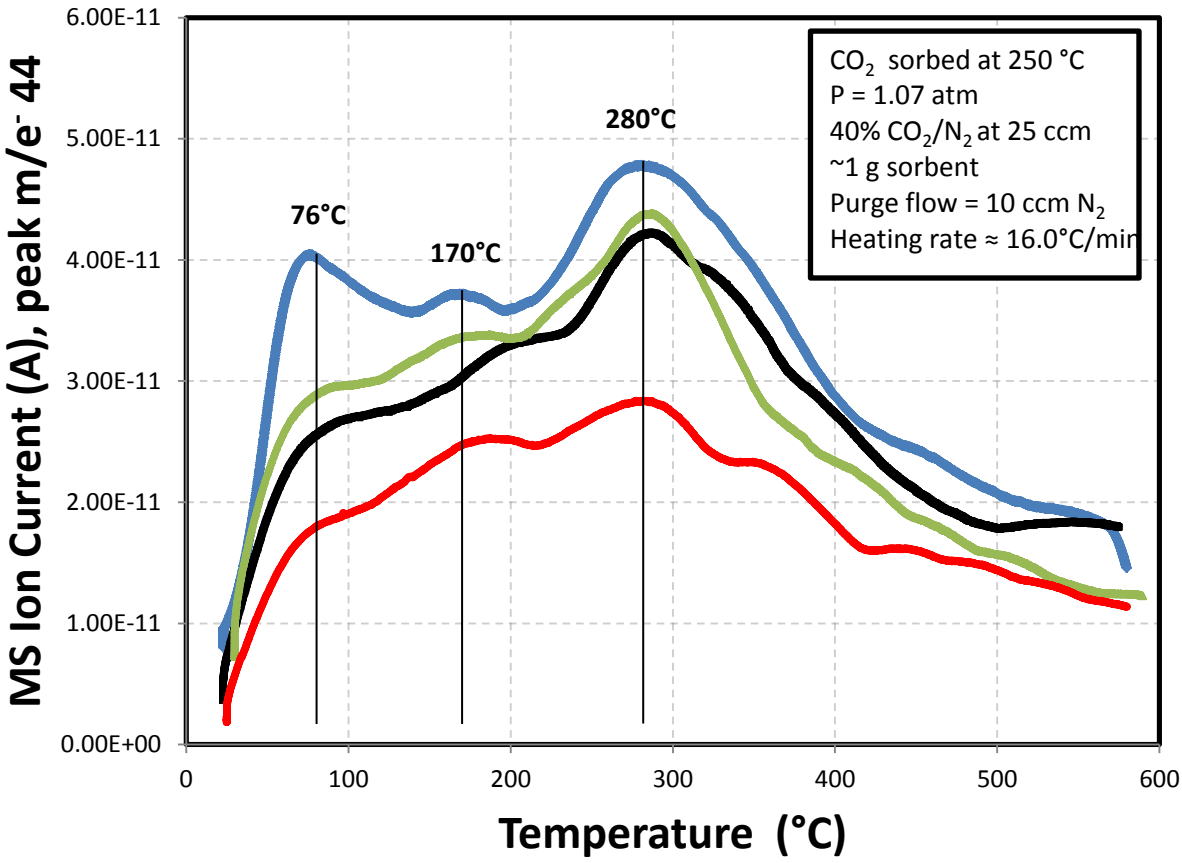

Figure 32: CO_2 TPD on Industrially Produced Na_2O promoted alumina

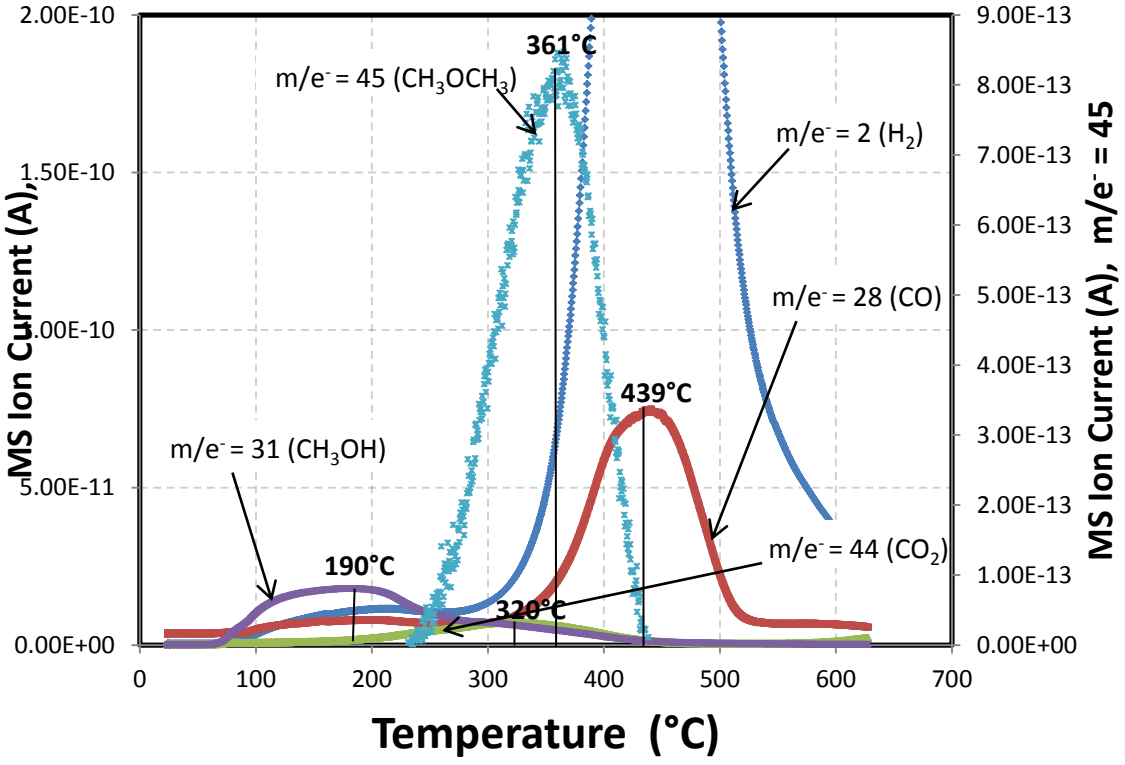

Figure 34: TPSR of methanol from Na_2O promoted Alumina (March 17, 2010)

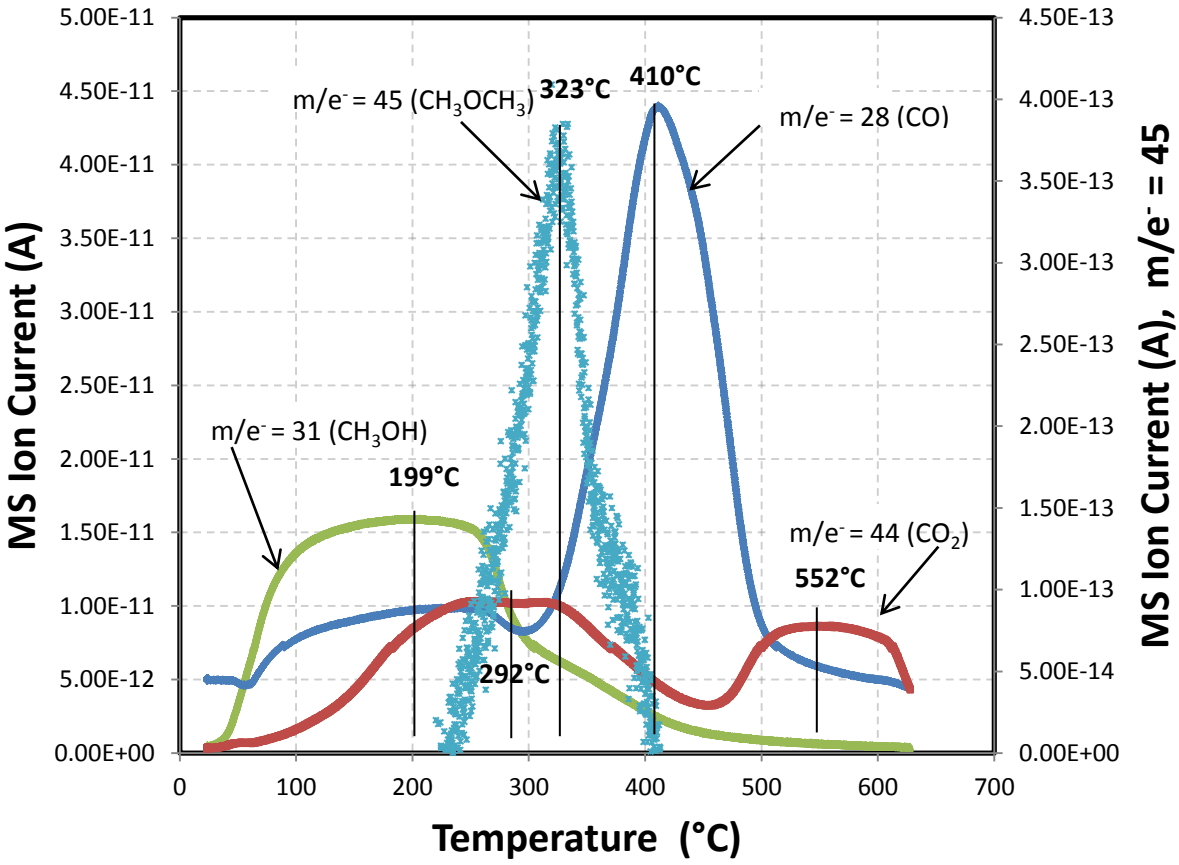

Figure 35: TPSR of methanol from Na_2O promoted Alumina (March 16, 2010)

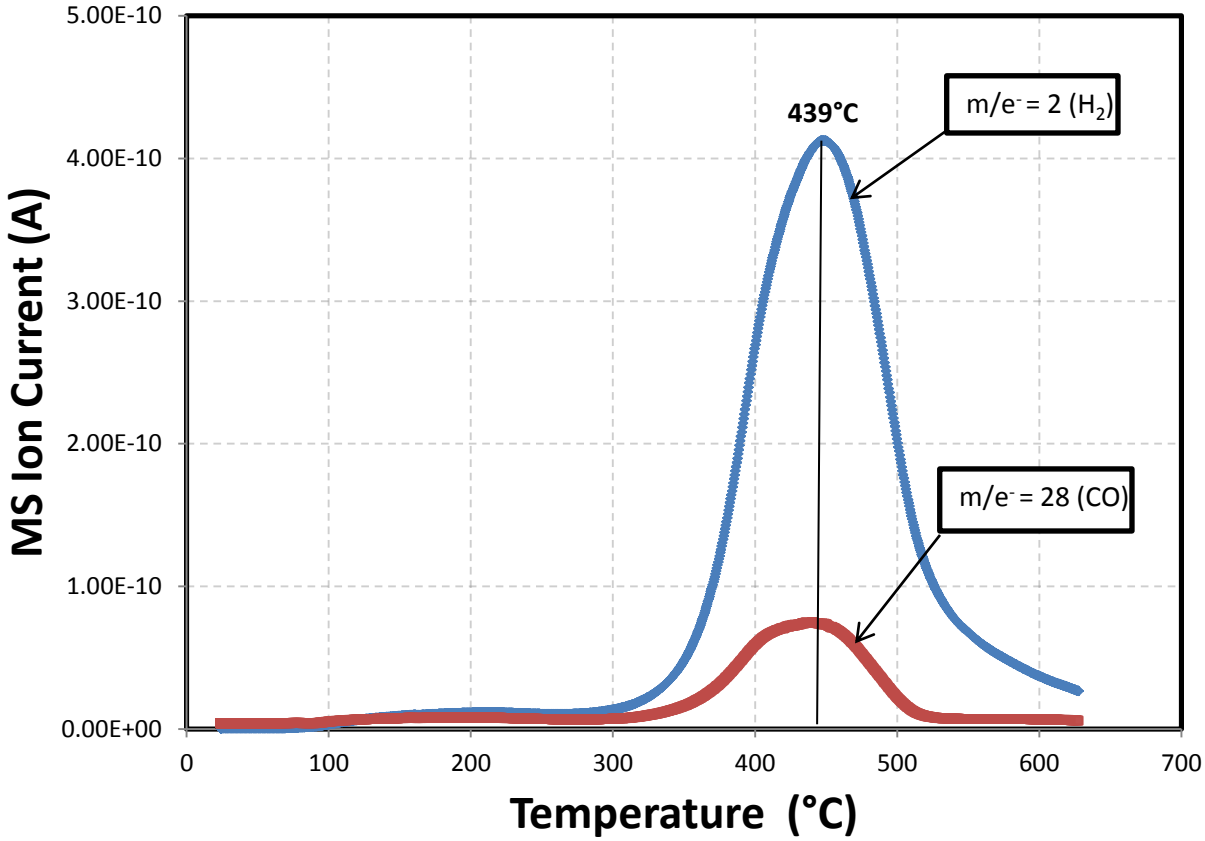

Figure 36: TPSR of methanol signal for H_2 and CO from March 18, 2010 experiment

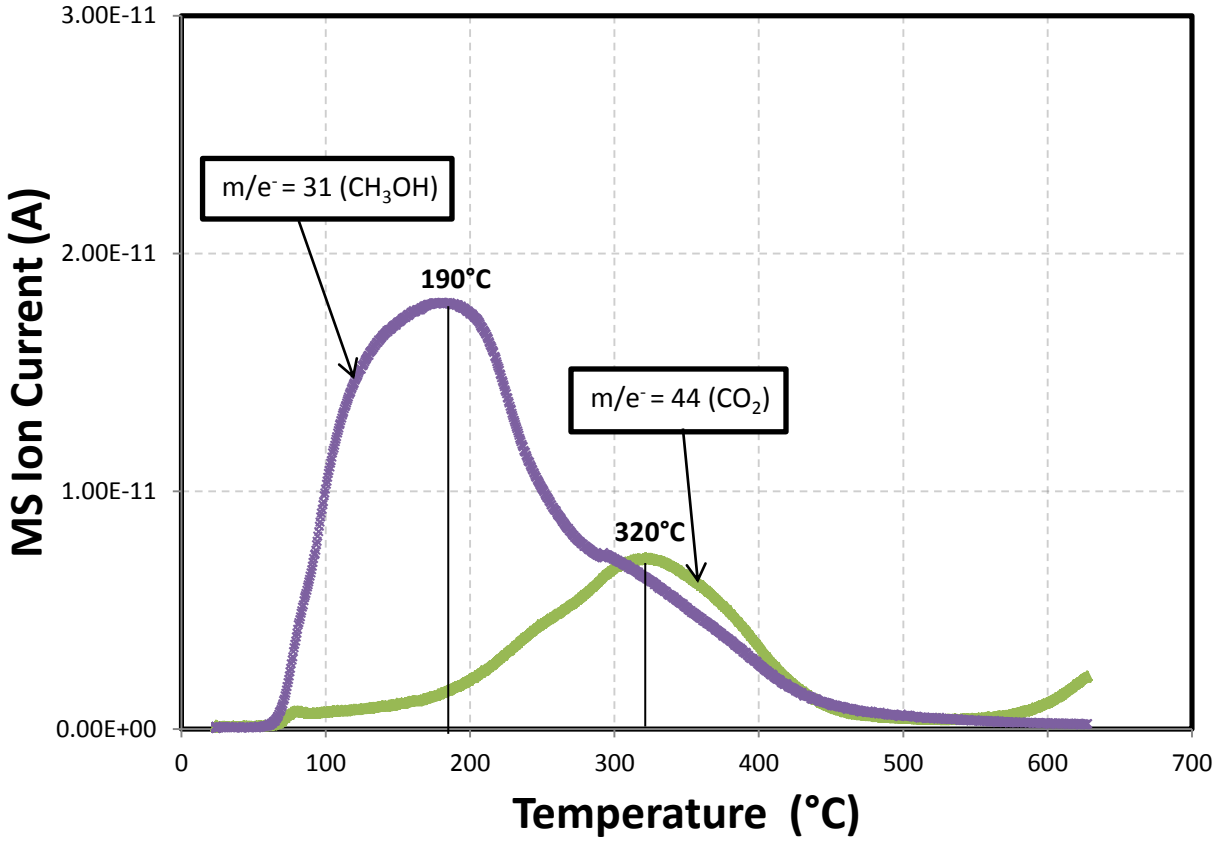

Figure 37: TPSR of methanol signal for CO_2 and methanol from March 18, 2010 experiment

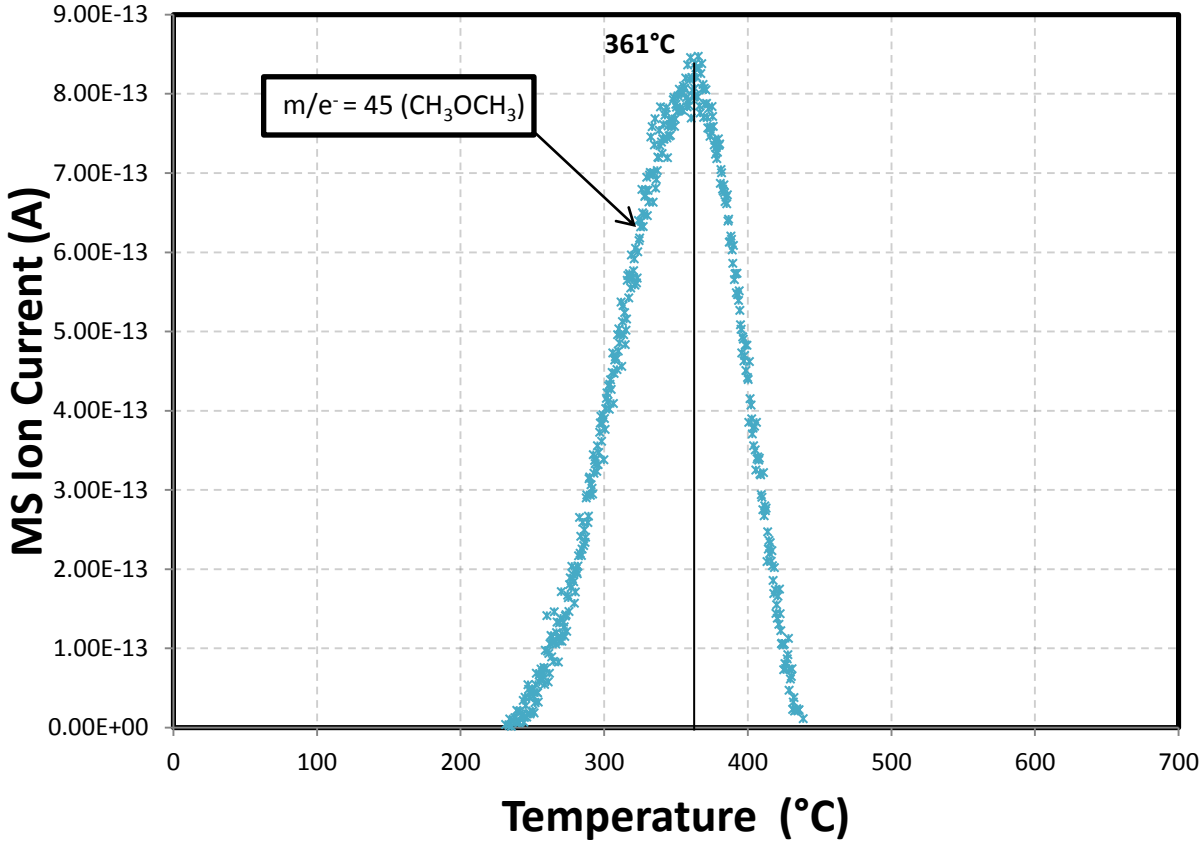

Figure 38: TPSR of methanol signal for di-methyl ether from March 18, 2010 experiment

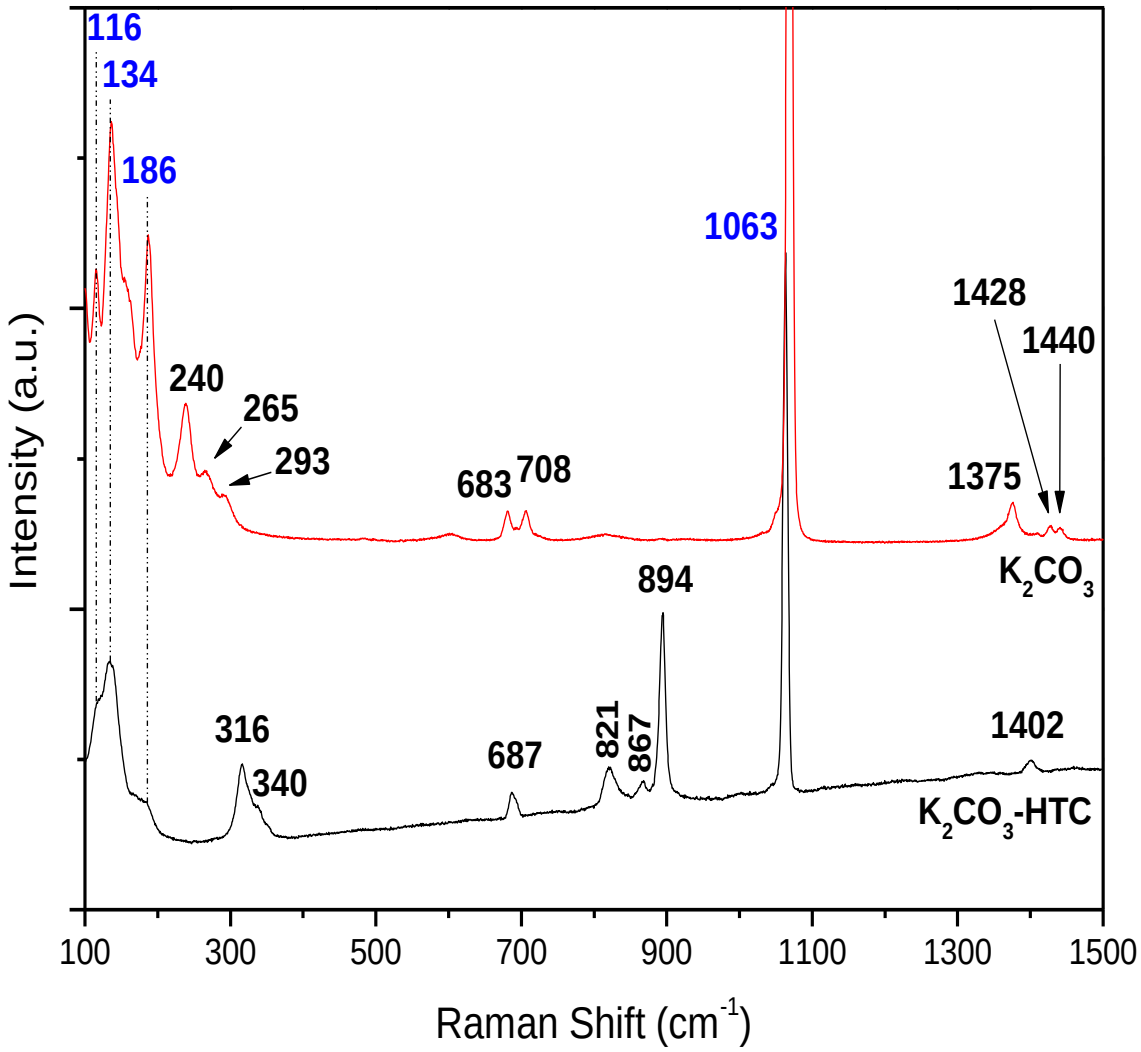

Figure 39: Dehydrated Raman Spectra of pure K_2CO_3 and K_2CO_3 promoted hydrotalcite at 400°C in flowing Ar

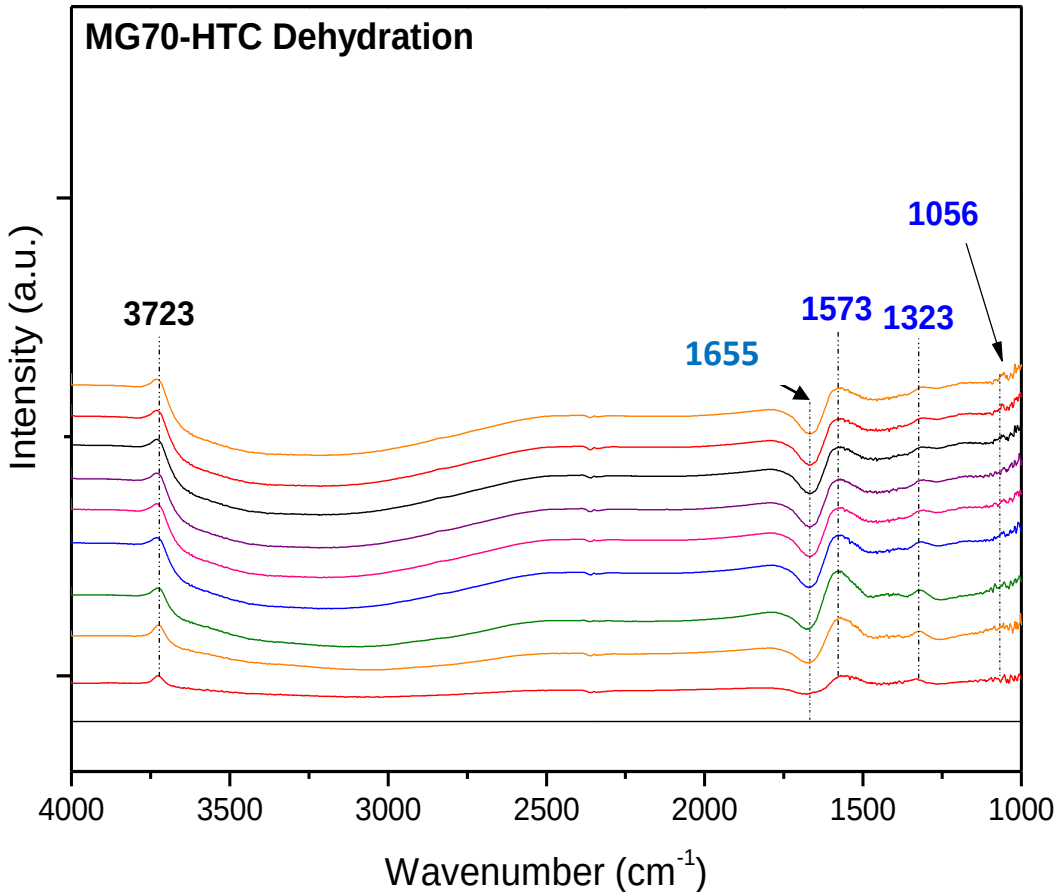

Figure 40: DRIFT spectra of SASOL MG70 hydrotalcite during dehydration at 400°C. Peak assignment: 1655 cm^{-1} = disappearance of H_2O from hydrotalcite structure, 1573, 1323, and 1056 cm^{-1} = surface carbonate, 3723 cm^{-1} = hydroxyl stretching.

Assignments from:

Busca, G., Lorenzelli, V., "Infrared Spectroscopic Identification of Species Arising from Reactive Adsorption of Carbon Oxides on Metal Oxide Surfaces," *Materials Chemistry,* 7, **(1982)**, 89-126,

Walspurger, S., Boels, L., Cobden, P.D., Elzinga, G.D., Haije, W.G., van den Drink, R.,W., "The Crucial Role of the K^+-Aluminum Oxide Interaction in K^+-Promoted Alumina- and Hydrotalcite-Based Materials for CO_2 Sorption at High Temperatures," *ChemSusChem,* 1 **(2008)** 643-650

Kloprogge, J.T., Frost, R.L., "Infrared Emission Spectroscopic Study of the Thermal Transformation of Mg-, Ni-, and Co-Hydrotalcite Catalysts," *Applied Catalysis A: General,* 184, **(1999),** 61-71

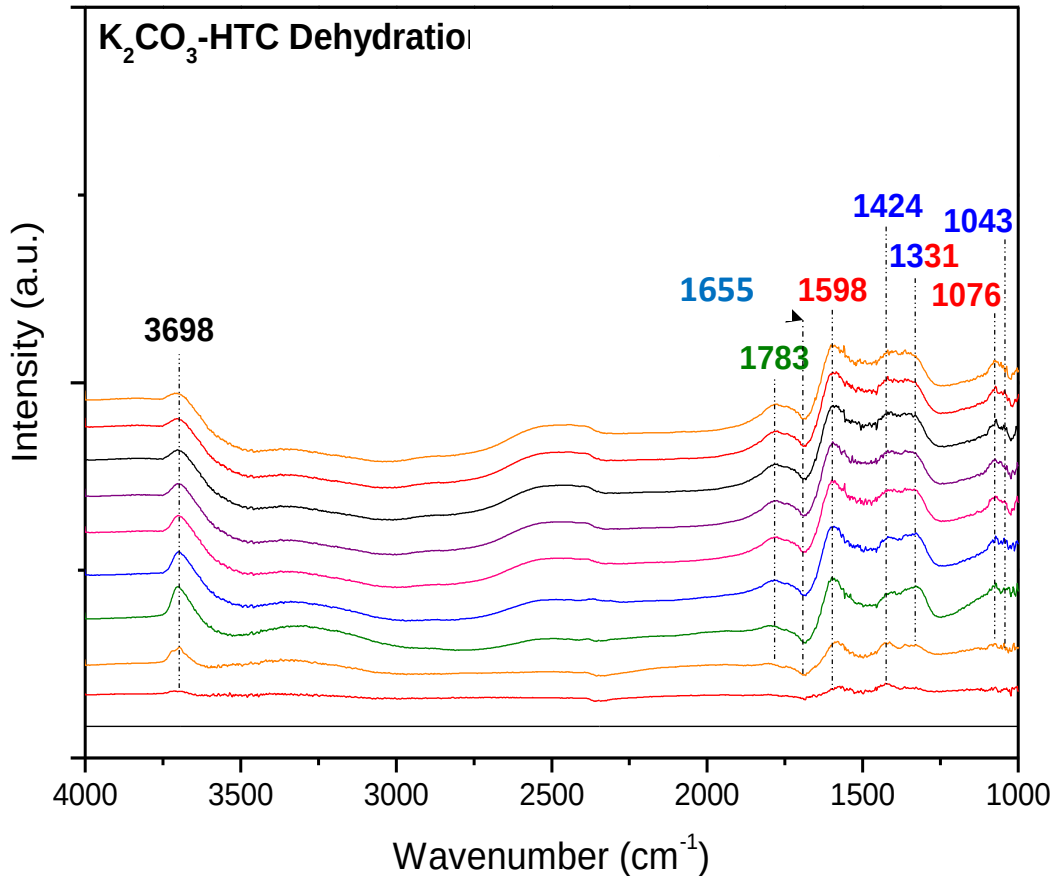

Figure 41: DRIFT spectra of K_2O_3 promoted hydrotalcite during dehydration at 400°C
Peak assignments: 1655 cm^{-1} = disappearance of H_2O from hydrotalcite structure, 1598, 1424, and 1076 cm^{-1} = surface carbonate, 1783, 1331, and 1043 cm^{-1} = surface bridged carbonate, 3723 cm^{-1} = hydroxyl stretching. Assignments from:

Busca, G., Lorenzelli, V., "Infrared Spectroscopic Identification of Species Arising from Reactive Adsorption of Carbon Oxides on Metal Oxide Surfaces," *Materials Chemistry,* 7, **(1982)**, 89-126,

Walspurger, S., Boels, L., Cobden, P.D., Elzinga, G.D., Haije, W.G., van den Drink, R.,W., "The Crucial Role of the K^+-Aluminum Oxide Interaction in K^+-Promoted Alumina- and Hydrotalcite-Based Materials for CO_2 Sorption at High Temperatures," *ChemSusChem,* 1 **(2008)** 643-650,

Kloprogge, J.T., Frost, R.L., "Infrared Emission Spectroscopic Study of the Thermal Transformation of Mg-, Ni-, and Co-Hydrotalcite Catalysts," *Applied Catalysis A: General,* 184, **(1999),** 61-71,

Ogden, J. S., Williams, S. J., "Matrix Isolation Studies on $Cs_2[CO_3]$, $Rb_2[CO_3]$, and $K_2[CO_3]$: The Shape of Molecular K_2CO_3," *J. Chem. Soc: Dalton Transactions,* **1981,** 2, 456-462

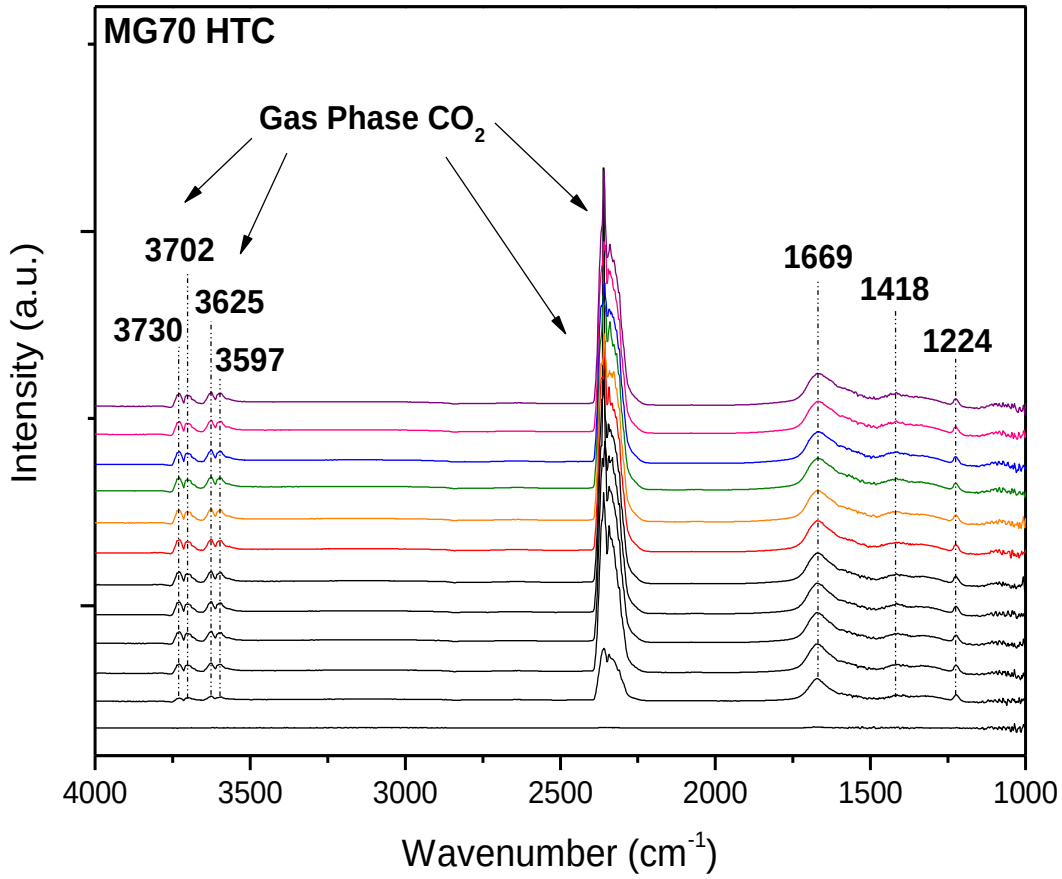

Figure 42: DRIFTS spectra of SASOL MG70 hydrotalcite during exposure to CO_2
Peak Assignment: 1669, 1419, and 1224 cm^{-1} = bicarbonate species bonded on Mg
Assignments from
Evans, J.V., Whateley, T.L., "Infrared Study of Adsorption of Carbon Dioxide and Water on Magnesium Oxide," *Trans Faraday Soc.*, 61, **(1967),** 2769

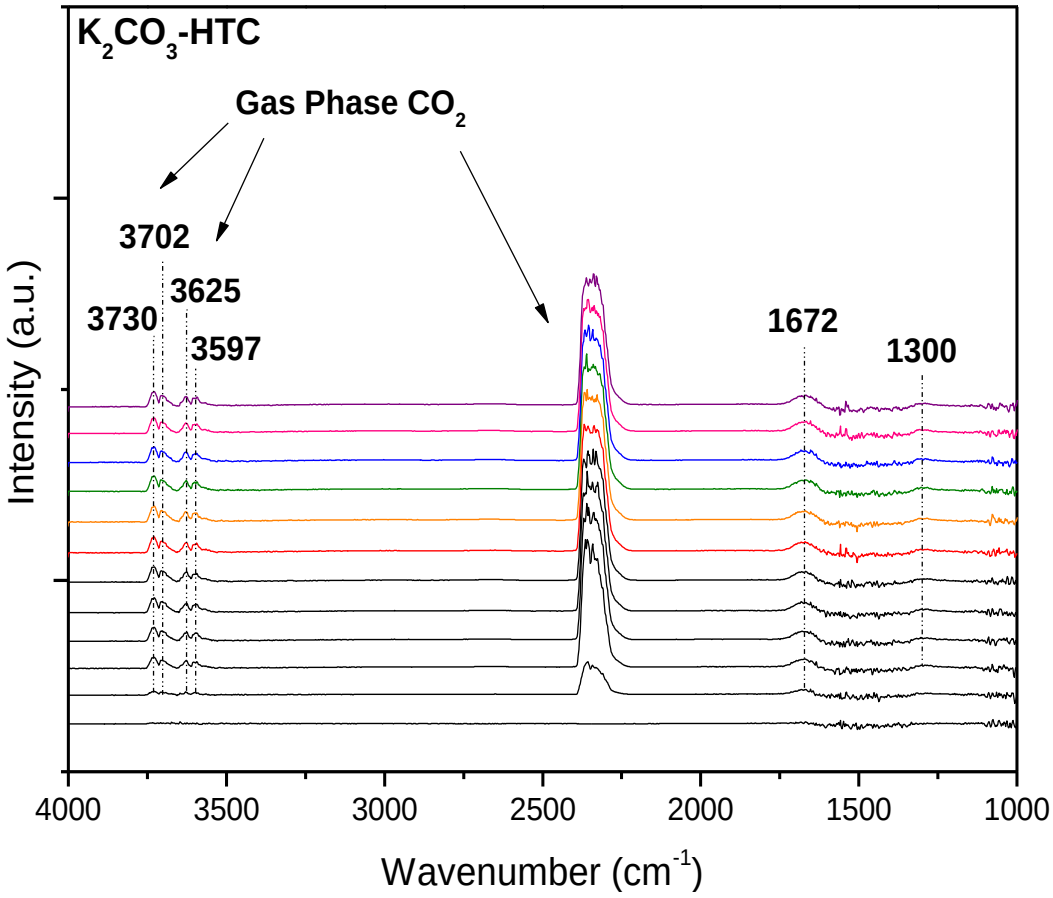

Figure 43: DRIFTS spectra of K_2O_3 promoted hydrotalcite during exposure to CO_2
Peak Assignments: 1672 and 1300 cm^{-1} = bidentate surface ligands (2) indicated by broadness of 1672 cm^{-1} peak
Assignments from
Smart, R.S.C., Slager., T.L., Little, L.H., Greenler, R.G., "Carbon Monoxide Adsorption on MagnesiumOxide," *J. Phys. Chem.*, 77, **(1973),** 1019-1023

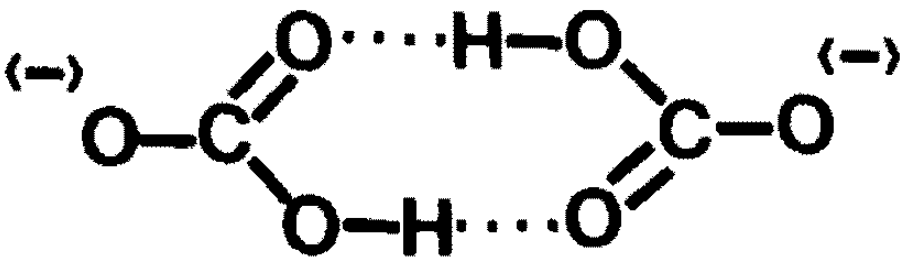

Figure 44: Picture of the dimer form of bicarbonate

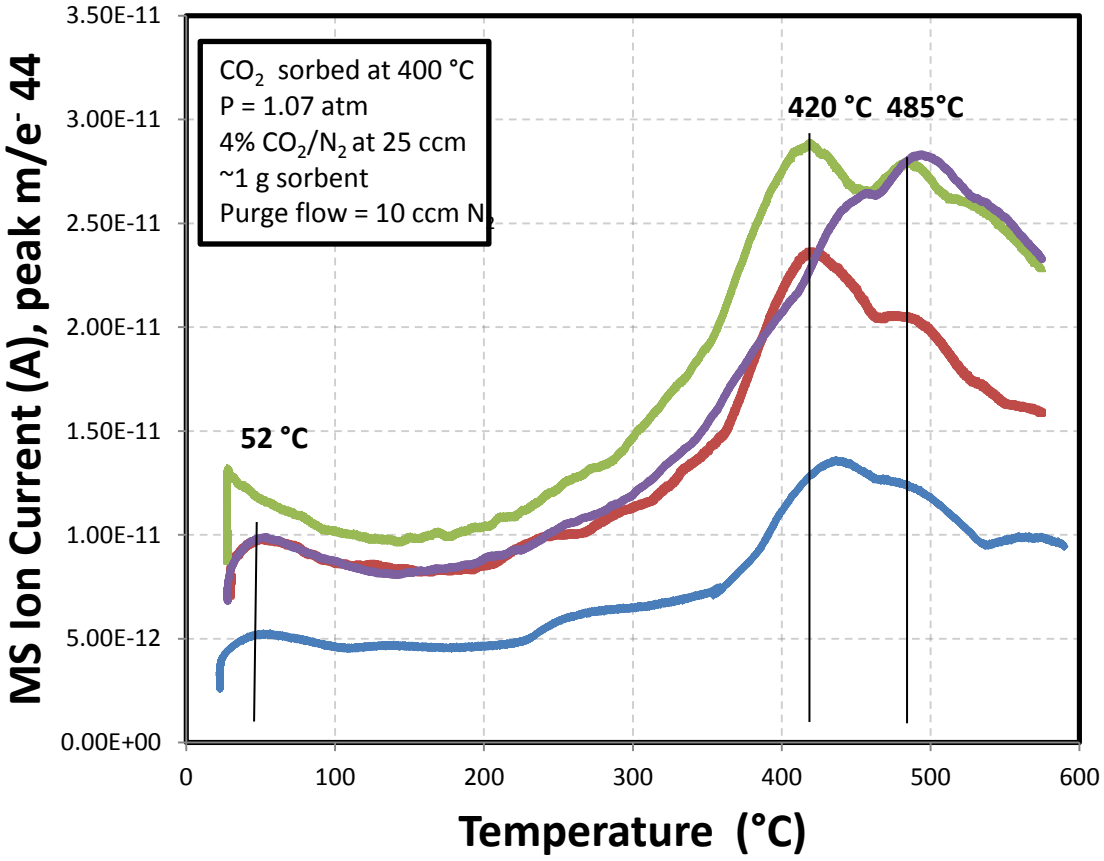

Figure 45: CO_2 TPD from K_2CO_3 promoted hydrotalcite

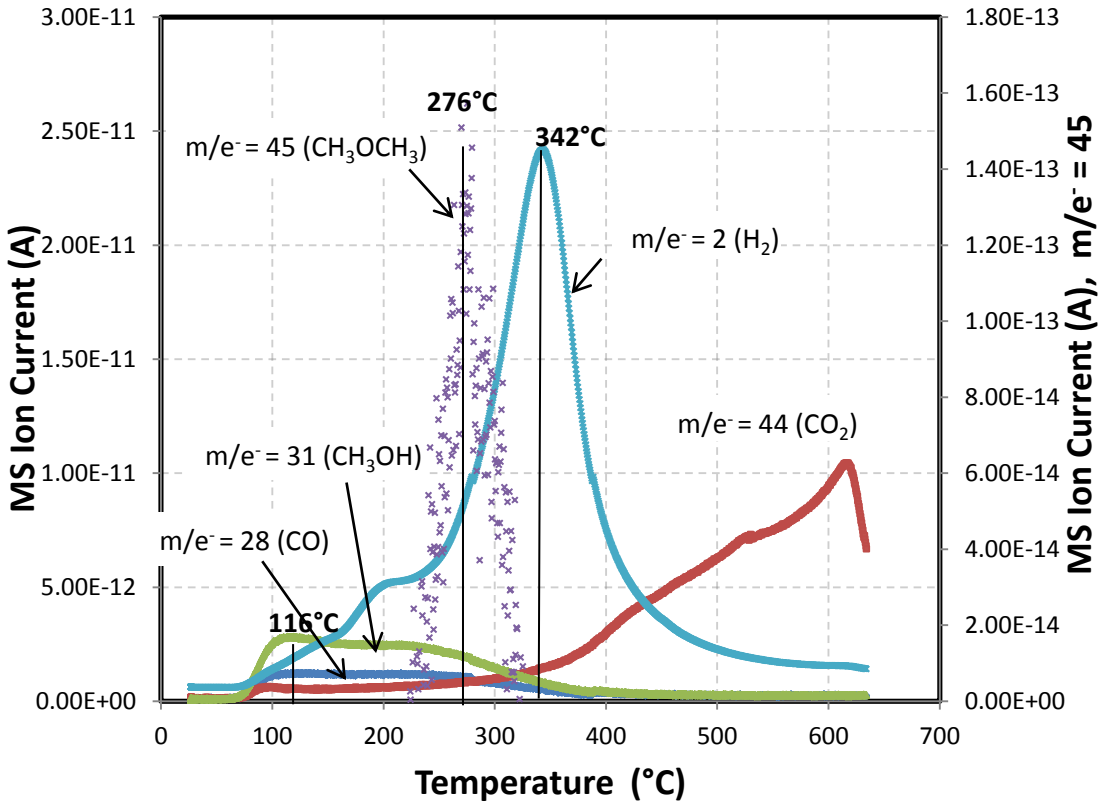

Figure 46: TPSR of methanol from K_2CO_3 promoted hydrotalcite

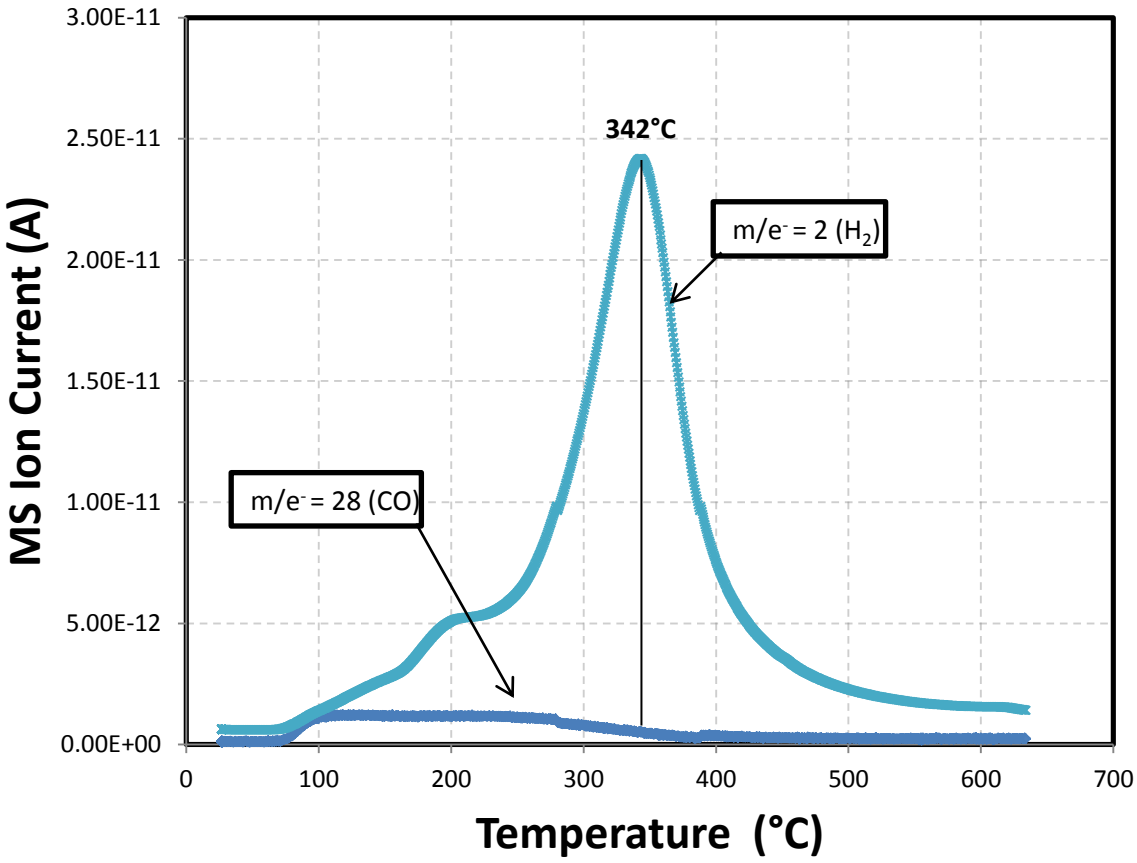

Figure 47: TPSR of methanol signal for H_2 and CO from March 22, 2010 experiment

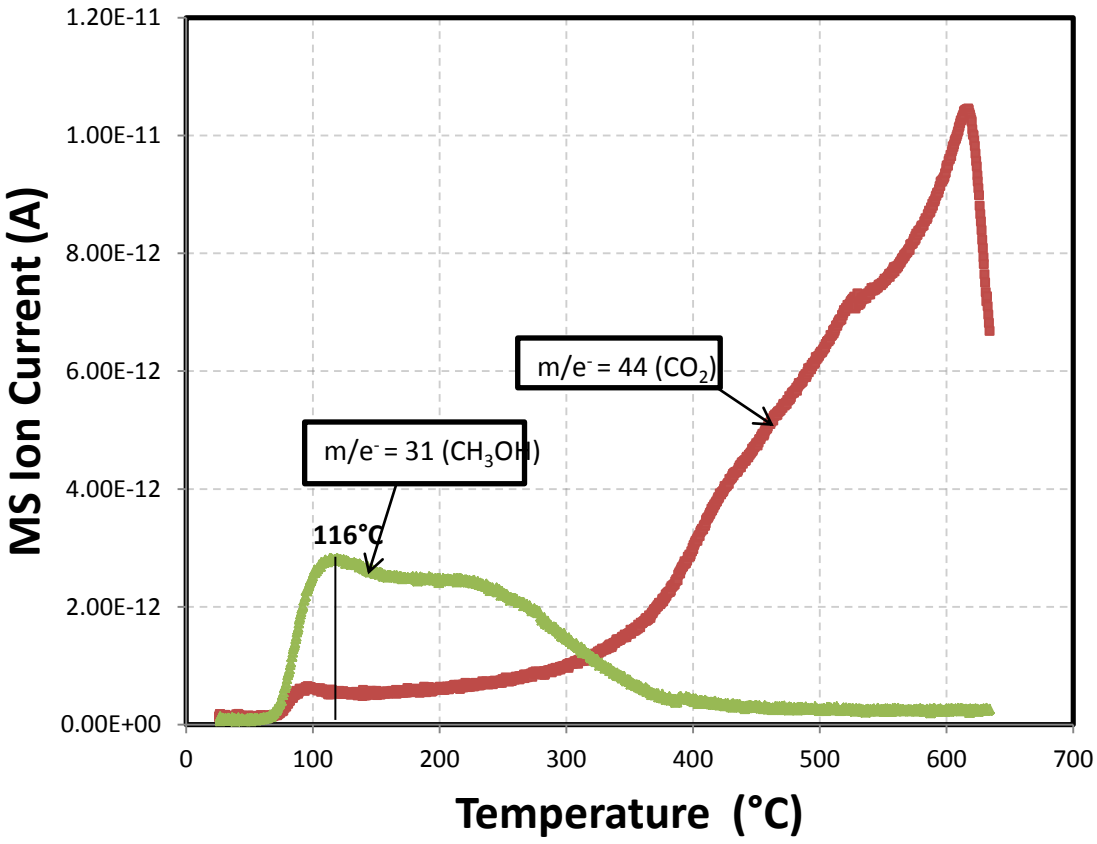

Figure 48: TPSR of methanol signal for CO_2 and Methanol from March 22, 2010 experiment

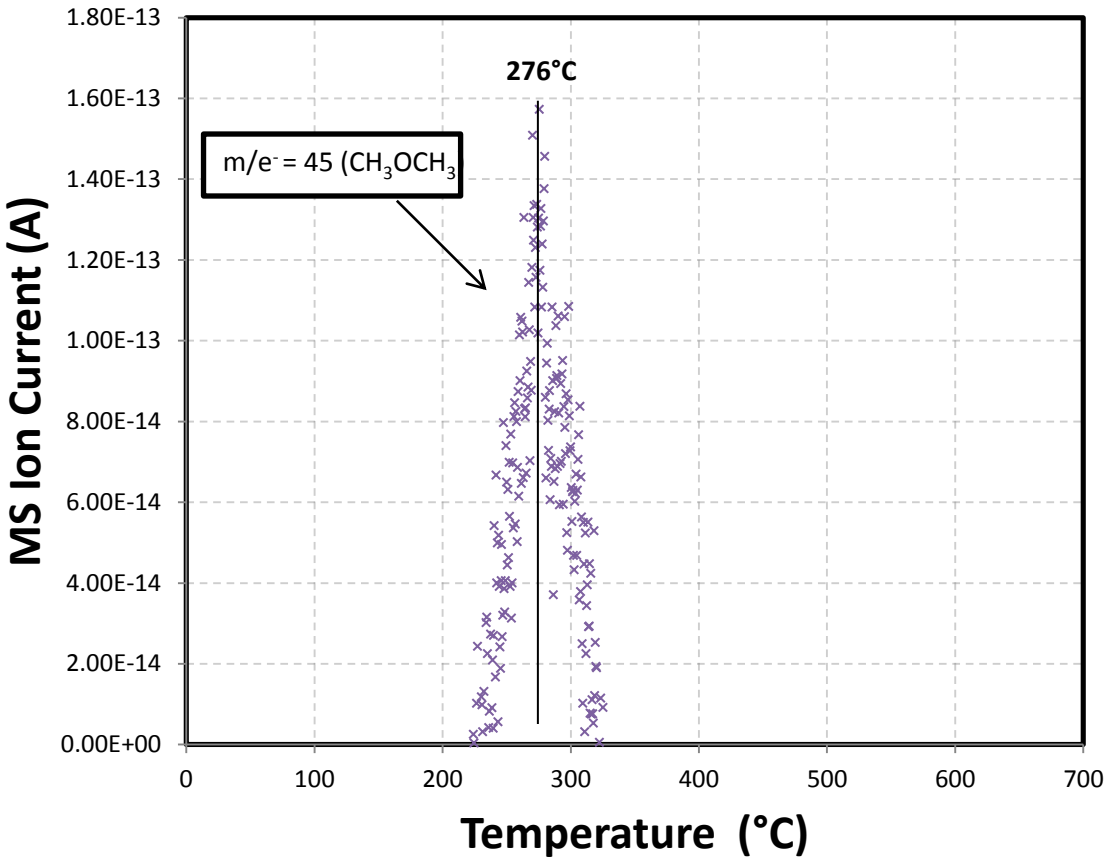

Figure 49: TPSR of methanol signal for di-methyl ether from March 22, 2010 experiment

Appendix A: List of Conference Presentations Performed under project DE-FC26-05NT4245

Beaver, M.G. (speaker), Caram, H. S., Sircar, S., **"**Utilization of High Temperature CO_2 Chemisorbents in Sorption Enhanced Reaction Concepts for Production of Fuel Cell Grade H_2 from Fossil Fuel Feedstocks," Presented at 26th International Pittsburgh Coal Conference on September 22, 2009

Beaver, M.G. (speaker), Caram, H. S., Sircar, S., "Experimental Demonstration of sorption enhanced reaction (SER) concepts for direct production of fuel cell grade H_2 by SE-water gas shift (WGS) and SE-steam methane reforming (SMR) reactions," Presented at IntertechPira Hydrogen Production and Storage Conference, Washington, D.C., October 1, 2009

Beaver, M.G. (speaker), Caram, H. S., Sircar, S., "Selection of CO_2 Chemisorbent for Fuel-Cell Grade H_2 Production by Sorption Enhanced Water-Gas-Shift & Steam- Methane-Reforming Reaction," Presented at American Institute of Chemical Engineering Annual Meeting, Nashville, TN, November 12, 2009

Beaver, M.G. (speaker), Sircar, S., "Adsorption Technology for Direct Recovery of Compressed, Pure CO_2 from a Flue Gas without Pre-compression or Pre-drying," presented at the Fundamentals of Adsorption 10 (FOA10), held in Awaji Island, Japan, May 28, 2010